A Primer on Surface Plasmon-Polaritons in Graphene

Yu. V. Bludov[1], Aires Ferreira[2], N. M. R. Peres[1], and M. I. Vasilevskiy[1]

[1] *Physics Department and CFUM, University of Minho, P-4710-057, Braga, Portugal.*

[2] *Graphene Research Centre and Department of Physics, National University of Singapore, 2 Science Drive 3, Singapore 117542*

We discuss the properties of surface plasmons-polaritons in graphene and describe four possible ways of coupling electromagnetic radiation in the terahertz (THz) spectral range to this type of surface waves: (i) the attenuated total reflection (ATR) method using a prism in the Otto configuration, (ii) graphene micro-ribbon arrays or monolayers with modulated conductivity, (iii) a metal stripe on top of the graphene layer, and (iv) graphene-based gratings. The text provides a number of original results along with their detailed derivation and discussion.

Keywords: Graphene; Surface Plasmon-Polaritons.

1. Introduction

It is since the days of Arnold Sommerfeld, back to 1899, that plasmonic effects in materials and gratings are investigated both theoretically and experimentally. Free electron plasma related phenomena in metallic gratings were investigated as early as 1902 by Wood [1]. An attempt to a theoretical interpretation of Wood's results was first made by Lord Rayleigh [2], followed, three decades latter, by Fano [3,4]. Systematic studies of plasmonic effects became possible with the work of Kretschmann [5] and Otto [6], who devised two different methods, using prisms [7] on top of or beneath a thin metallic film, of exciting surface plasmon–polaritons (SPPs). SPPs are evanescent electromagnetic waves coupled to the free electron plasma oscillations, propagating along the surface of a conductor. Meanwhile, reliable theoretical methods for studying scattering of electromagnetic radiation (ER) by metallic gratings have been developed by several authors [8,9,10].

Modern plasmonics gained a renewed interest with the discovery of the anomalously high transmittance through a periodic array of holes with a size smaller than the diffraction limit [11]. The effect was explained invoking surface plasmons (SPs) [12,13,14,15,16,17]. Another impressive SP-related effect is the surface enhanced Raman scattering (SERS) [18,19]. Beyond the fundamental physics, the plasmonics encompass a wide range of applications [20], such as spectroscopy and sensing [18,21,22,23,24], photovoltaics [25], optical tweezers [26,27], nano-photonics [13,28], radiation guiding [29], transformation and Fourier optics [30,31,32], etc. These applications rely on the short wavelength of SPPs (compared propagating photons of the same energy), strong

dependence of their dispersion relation on the environment dielectric constant, and high local field intensity associated with localised SPs.

Doped graphene sustains surface plasmons [33,34,35,36,37] whose frequency is proportional to the 1/4 power of the electronic density, a result specific to single-layer graphene, and to the 1/2 power of the wave number, a behavior shared with the 2D electron gas [38]. Moreover, the carrier density in graphene can be varied continuously from nearly zero to $\sim 10^{13}\mathrm{cm}^{-2}$ for either type of majority carriers (electrons or holes) by the application of an external voltage. This important ambipolar doping effect has opened the tantalizing prospect of real time control of SPPs by using a gate. In addition, the transfer of graphene films to a range of substrates is routine nowadays and has inspired the design of graphene-based structures with unique plasmonic signatures, such as quantum dots (or anti-dots) [39,40,41,42,43] and nanoribbons [44,45,46,47,48]. In this respect, the question of whether the classical description of SPs still holds for finite-size systems, such as quantum dots, is particularly relevant [43].

The robustness of graphene SPPs with respect to external perturbations, as well as the interaction of SPPs with individual quantum systems, are active topics of research: the effect of applied stress in the graphene plasmon dispersion [49,50], and the role of SPPs in graphene on the decay rate of nano-emitters [51,52,53,54,55] are now well established. Plasmons in bilayer graphene have also attracted attention [56] and the transverse electric (TE) mode spectrum has recently been obtained [57]. The plasmon dispersion relation of a graphene double-layer, two closely separated graphene sheets, has also been addressed [58,59]. A natural extension of the study of propagation of SPPs in monolayer graphene is the investigation of the same effect in graphene double-layers. In this case, the two degenerate dispersion relations of each of the layers hybridize, giving rise to optical and acoustic branches [60,61,62].

A series of recent experimental works [63,64,65,66] triggered a revival of interest in plasmonic effects in graphene [67,68]. In particular, it has been shown that graphene has a strong plasmonic response in the THz frequency range at room temperature [64]. THz photonics is emerging as an active field of research [69] and graphene may play a key role in THz metamaterials in the near future. Ju *et al.* have shown [64] that ER impinging on a grid of graphene microribbons can excite SPPs in graphene, leading to prominent absorption peaks, whose position can be tuned by doping. Fei *et al.* mapped the plasmon dispersion relation of graphene, and demonstrated its plasmonic tunability [66]. In agreement with the theory,[37] infrared SPPs in graphene have been shown to possess remarkably large propagation lengths when gauged against more conventional structures [70]. A similar experiment was performed by Chen *et al.* [71], where excitation and subsequent detection of SPPs were achieved. Yan *et al.* [72] have shown that graphene/insulator stacks can be used as tunable infrared plasmonic devices, able to work both as a filter and as a polarizer, having the potential for far-infrared (FIR) and THz photonic devices. As a proof of principle experiment, it has been shown that this type of devices can shield 97.5% of ER at frequencies below 1.2 THz [72]. Last, the possibility of transforming graphene into a

mantle cloak, working in the THz spectral range, has also been addressed [73].

In general, SPPs cannot be excited by directly shining light on a homogeneous system due to kinematic reasons: the momentum of a surface polariton is much larger than that of the incoming light having the same frequency. Therefore, some type of mechanism is necessary to promote the excitation of SPPs. The most common mechanisms for SPPs excitation are: (i) attenuated total reflection (ATR) [74], (ii) scattering from a topological defect at the conductor surface [13,75], and (iii) Bragg scattering using diffraction gratings [76] or a periodic corrugation of the surface of the conductor [8,77]. The method of Ju *et al.* is similar (but not identical) to the patterning of a metallic grating [65] on top of graphene. A theoretical account of the experiment by Ju *et al.* [64] was given in a recent work [44]. A novel method of SPP excitation consists in using the apex of an illuminated nanoscale tip [70]; this method provides a two-orders of magnitude enhancement of the in-plane momentum relatively to that of the impinging ER in free space bypassing the referred kinematic limitation. It has also been shown that modulation of the optical conductivity gives rise to efficient ER coupling to SPPs in graphene [78] without the need of a grating. The same principle works with split [79] or modulated [80] gates. Free space excitation of SPPs using non-linear optics effects has been proposed [81,82] and effectively put in action [83].

The reason why a periodic corrugation allows for the excitation of SPPs can be understood in analogy with the theory of electrons in a periodic potential. Here the periodic corrugation plays for SPPs the same role as the periodic atomic potential plays for electrons, that is, the SPP momentum is conserved up to a reciprocal lattice vector. The periodic corrugation provides the missing momentum needed to excite the polariton. Another way of understanding the effect is to note that the grating gives rise to a SPP band structure. Then the folding of the SPP dispersion curve, forming bands in the first Brillouin zone, makes it possible for an incident electromagnetic wave to excite a SPP mode associated with the upper bands for the same wavevector. The excitation of SPP modes in the first band still is not possible in the grating configuration unless the ATR technique is used.

This paper is organized as follows. In Sec. 2 we write down the macroscopic form of Maxwell's equations, introduce boundary conditions at an interface containing a graphene sheet, and provide the definition of TM (transverse magnetic) and TE waves. In Sec. 3 we review the basic properties of the optical conductivity of graphene. In Sec. 4 we compute the spectrum of a TM SPP wave providing both numerical and analytical results. In Sec. 5 we derive the dispersion relation of a TE SPP wave. In Sec. 6 we discuss in detail the excitation of SPPs on graphene using a prism in the ATR configuration originally proposed by Otto [6]. In Sec. 8 we discuss scattering of ER by an array of graphene microribbons and other flat graphene structures with periodically modulated conductivity. Section 7 is devoted to the SPP excitation by shining light on a metal stripe deposited on graphene. In Sec. 9 we give a formulation of Rayleigh approximation to scattering of ER by a

graphene-based grating due to Toigo *et al.* [8], adapted to this particular geometry. There the problems of both a sine a sawtooth gratings are solved. In Sec. 10 we discuss SPPs on a metal grating coated with graphene. In Sec. 11 we summarize the main results of the paper. In all sections we give enough details, so that the interest reader may reproduce all the results by him/herself.

2. Maxwell's equations and boundary conditions

2.1. *Planar geometry*

The central idea of the emerging area of nanoplasmonics is the use of SPPs, coupled charge-radiation excitations existing at a dielectric/conductor interface, for applications ranging from chemical sensors and surface-enhanced Raman spectroscopy (able to detect a single molecule) to solar cell's optimization. One of the most attractive features of SPPs is that they concentrate and guide ER at subwavelength scales. This is appealing since one can conceive circuitry using metals embedded in dielectrics, which is able to propagate both electric signals and SPPs [28]. In graphene, the SPP wavelength can be about 40 times shorter than the wavelength of the impinging radiation in free space [71].

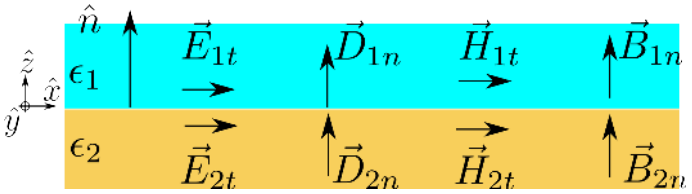

Fig. 1. Tangential and perpendicular fields at an interface. A graphene sheet is located between the two dielectrics.

We shall consider a graphene sheet, with conductivity σ, cladded by two dielectrics of relative dielectric permittivity ϵ_1 and ϵ_2. Graphene can be seen as the ultimate conductive thin film able to support SPPs [84]. As in any other conductor, the free charges in graphene couple to ER. We seek solutions of Maxwell's equations in the form of surface waves propagating along the graphene sheet. As we will see, graphene supports two different types of surface waves, the TM (or $p-$polarized) and TE (or $s-$polarized) SPPs.

2.2. *Maxwell's equations*

In the MKS system of units, the macroscopic Maxwell's equations read

$$\vec{\nabla} \cdot \vec{D} = \rho_f \,, \tag{1}$$

$$\vec{\nabla} \times \vec{E} = -\frac{\partial \vec{B}}{\partial t} \,, \tag{2}$$

$$\vec{\nabla} \cdot \vec{B} = 0 \,, \tag{3}$$

$$\vec{\nabla} \times \vec{H} = \vec{J}_f + \frac{\partial \vec{D}}{\partial t} \,, \tag{4}$$

where $\vec{D} = \epsilon\epsilon_0\vec{E}$, $\vec{B} = \mu_0\vec{H}$, ϵ is the relative dielectric permittivity, ϵ_0 and μ_0 are the vacuum dielectric and magnetic permeability, ρ_f is the charge density (charge per unit volume), and $\vec{J}_f$ is the current density (current per unit area).

In the case of a 2D metal, such as graphene, and assuming that it lies in the $xy-$plane, we have

$$\vec{J}_f = \vec{J}_s\delta(z) \,, \qquad \rho_f = \rho_s\delta(z) \,, \tag{5}$$

where $\vec{J}_s$ is the surface current density (current per unit length), ρ_s is the surface charge density (charge per unit area). For a 2D metal with a frequency–dependent (optical) conductivity σ, we have $\vec{J}_s = \sigma\vec{E}_t$, where $\vec{E}_t$ lies in the $xy-$plane as well.

The boundary conditions at the interface between the two media are (see also Fig. 1):

$$\vec{E}_{1t} = \vec{E}_{2t} \,, \tag{6}$$

$$\vec{H}_{1t} - \vec{H}_{2t} = \vec{J}_s \times \hat{n} \,, \tag{7}$$

$$D_{1n} - D_{2n} = \rho_s \,, \tag{8}$$

$$B_{1n} = B_{2n} \,. \tag{9}$$

Since graphene is a two-dimensional system, it enters in the calculation of the surface wave dispersion relation only through the boundary conditions. Then, the only quantity we need to known is its optical conductivity.

Assuming the time dependence of the fields in the form $e^{-i\omega t}$ and considering the absence of free volume currents and charges, Eqs. (2) and (4) are written as

$$\partial_y E_z - \partial_z E_y = i\omega B_x \,, \tag{10}$$

$$\partial_z E_x - \partial_x E_z = i\omega B_y \,, \tag{11}$$

$$\partial_x E_y - \partial_y E_x = i\omega B_z \,, \tag{12}$$

and

$$\partial_y B_z - \partial_z B_y = -ic^{-2}\epsilon\omega E_x \,, \tag{13}$$

$$\partial_z B_x - \partial_x B_z = -ic^{-2}\epsilon\omega E_y \,, \tag{14}$$

$$\partial_x B_y - \partial_y B_x = -ic^{-2}\epsilon\omega E_z \,, \tag{15}$$

respectively. As mentioned above, Maxwell's equations apply to the dielectrics with permittivity ϵ_1 and ϵ_2 surrounding graphene, and we take into account the relation $\mu_0\epsilon_0 = c^{-2}$.

2.3. *Definition of TE and TM modes and Poynting vector*

A conductive surface, depending on certain properties of metal's optical conductivity, can support transverse electric (TE or $s-$polarized) or/and transverse magnetic (TM or $p-$polarized) surface waves. These waves propagate along the metallic interface and decay exponentially away from it (along the $z-$direction). In the case of graphene, the free carrier oscillations are confined to the xy plane, while the electromagnetic field penetrates considerably into the cladding materials.

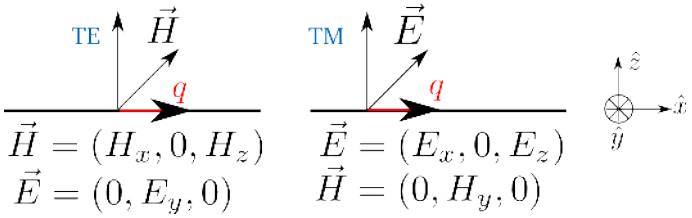

Fig. 2. Electric and magnetic fields of transverse electric (TE; left in the figure) and transverse magnetic (TM; right in the figure) surface waves. The graphene sheet lies in the $xy-$plane.

In Fig. 2 we represent both types of waves propagating along the $\hat{x}$ direction with momentum q. For TE-waves the electric field is oriented along the $\hat{y}$ direction. Then, we have

$$\vec{J}_s \times \hat{n} = \sigma_{yy} E_y \hat{y} \times \hat{n} = \sigma_{yy} E_y \hat{x}\,, \tag{16}$$

and for TM-waves the magnetic field is oriented along the $\hat{y}$ direction, so we have

$$\vec{J}_s \times \hat{n} = \sigma_{xx} E_x \hat{x} \times \hat{n} = -\sigma_{xx} E_x \hat{y}\,, \tag{17}$$

where we have assumed an anisotropic response. For an isotropic system, such as unstrained graphene, $\sigma_{xx} = \sigma_{yy} = \sigma$.

For future use, we recall here the definition of the Poynting vector, which is the instantaneous ER energy flux per unit area [85],

$$\vec{S} = \vec{E} \times \vec{H}\,, \tag{18}$$

where $\vec{E}$ and $\vec{H}$ are assumed to be real. Representing $\vec{E}$ and $\vec{H}$ by harmonic functions we have:

$$\begin{aligned} \vec{S} &= \Re(\vec{E}_0 e^{ikz - i\omega t}) \times \Re(\vec{H}_0 e^{ikz - i\omega t}) \\ &= \frac{1}{2}\Re(\vec{E}_0 \times \vec{H}_0^*) + \frac{1}{2}\Re(\vec{E}_0 \times \vec{H}_0 e^{2i(kz - \omega t)})\,. \end{aligned} \tag{19}$$

The time average of $\vec{S}$, i.e. the directional energy flux density, reads:

$$\langle \vec{S} \rangle = \frac{1}{2} \Re(\vec{E}_0 \times \vec{H}_0^*) \,. \tag{20}$$

The calculation of $\langle \vec{S} \rangle$ allows for the determination of the ER reflectance and transmittance at an interface.

3. Optical conductivity of graphene

3.1. *General expression*

In this section we provide a brief overview of the optical properties of graphene. Its optical conductivity is a sum of two contributions: (i) a term describing interband transitions and (ii) a Drude contribution, describing intraband processes. At zero temperature the optical conductivity has a simple analytical expression [86,87,67,68,88,89]. The inter-band contribution has the form $\sigma_I = \sigma_I' + i\sigma_I''$, with

$$\sigma_I' = \sigma_0 \left(1 + \frac{1}{\pi} \arctan \frac{\hbar\omega - 2E_F}{\hbar\gamma} - \frac{1}{\pi} \arctan \frac{\hbar\omega + 2E_F}{\hbar\gamma} \right) , \tag{21}$$

and

$$\sigma_I'' = -\sigma_0 \frac{1}{2\pi} \ln \frac{(2E_F + \hbar\omega)^2 + \hbar^2\gamma^2}{(2E_F - \hbar\omega)^2 + \hbar^2\gamma^2} \,, \tag{22}$$

where $\sigma_0 = \pi e^2/(2h)$, $e < 0$ is the electron charge, γ is the relaxation rate, and $E_F > 0$ denotes the (local) Fermi level position with respect to the Dirac point. The Drude conductivity term is

$$\sigma_D = \sigma_0 \frac{4E_F}{\pi} \frac{1}{\hbar\gamma - i\hbar\omega} \,. \tag{23}$$

The total conductivity is therefore given by

$$\sigma_g = \sigma' + i\sigma'' = \sigma_I' + i\sigma_I'' + \sigma_D \,. \tag{24}$$

In Fig. 3 the two contributions, Drude and interband, are plotted separately for a given value of E_F and $\Gamma = \hbar\gamma$. For heavily doped graphene and for photon energies $\hbar\omega/E_F \ll 1$, the optical response is dominated by the Drude term. Therefore, in what follows we assume

$$\sigma_g \approx \sigma_D \,, \tag{25}$$

since we are interested in this regime of frequencies. For the frequency range of interest in this work (the THz spectral range) the above approximation gives accurate results. The only exception to this approximation will be made when discussing TE-waves in graphene (Sec. 5).

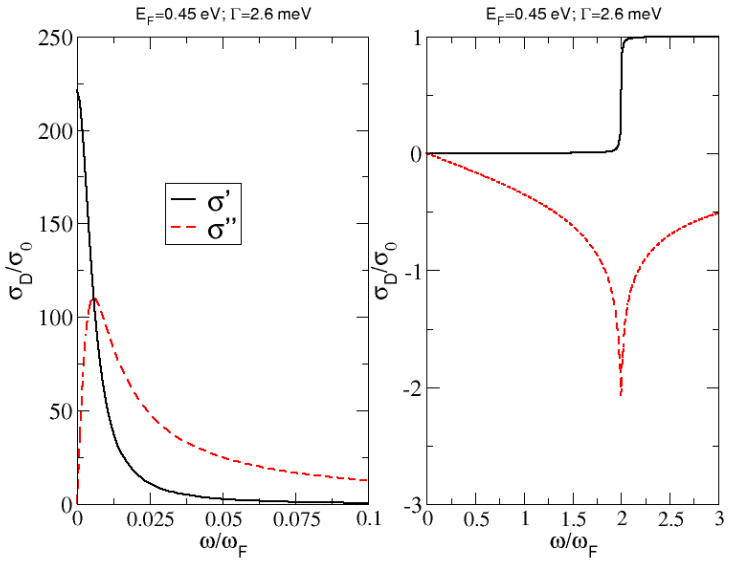

Fig. 3. Optical conductivity of uniform graphene: Drude (left) and inter-band (right) contributions. We assume $E_F = 0.45$ eV and $\Gamma = 2.6$ meV. The solid (dashed) line stands for the real (imaginary) part of the conductivity. In both panels $\omega_F = E_F/\hbar$.

3.2. *Drude conductivity in a magnetic field*

When a static external magnetic field is considered, the response of two-dimensional electronic systems to an external time-dependent field is described by the magneto-optical conductivity tensor $\sigma_{\alpha\beta}$, where $\alpha, \beta = x, y$ denote the in-plane coordinates. The tensorial nature of the magneto-optical response is a direct manifestation of the Lorentz force which, in the presence of a magnetic field, gives origin to both longitudinal and transverse electronic currents.

We assume that the applied static magnetic field is homogeneous and transverse to the graphene sheet, $\vec{B} = B\hat{z}$. In the semiclassical regime, $\hbar\omega/E_F \ll 1$, the magneto-optical transport in graphene can be described in terms of Boltzmann's transport equation. [90] Within this formalism, the electric current is obtained according to

$$\vec{J} = \frac{e}{\pi^2} \int d^2\vec{k}\; \delta f_{\vec{k}}\, \vec{v}_{\vec{k}}\,, \tag{26}$$

where $\delta f_{\vec{k}}$ is the deviation of the carriers' (electrons or holes) distribution function from the equilibrium Fermi–Dirac distribution, $f_0(\epsilon)$, and

$$\vec{v}_{\vec{k}} = v_F(\cos\theta_{\vec{k}}, \sin\theta_{\vec{k}})\,, \tag{27}$$

with $v_F \approx 10^6$ m/s denoting the Fermi velocity in graphene and $\theta_{\vec{k}} = \arctan(k_y/k_x)$. We remark that both spin and valley degeneracies have been included in Eq. (26).

In the presence of an electromagnetic field, the distribution function perturbation, $\delta f_{\vec{k}}$, is the solution of the kinetic equation [91],

$$-e\vec{E}_{\parallel}\cdot\vec{v}_{\vec{k}}\frac{\partial f_0}{\partial\epsilon}=\frac{\delta f_{\vec{k}}}{\tau_{\vec{k}}}+\frac{e}{\hbar}\left(\vec{v}_{\vec{k}}\times\vec{B}\right)\cdot\frac{\partial}{\partial\vec{k}}\left[\delta f_{\vec{k}}\right]\,, \tag{28}$$

where the standard relaxation approximation,

$$\frac{\partial}{\partial t}\left[\delta f_{\vec{k}}\right]\Big|_{\rm scatt}=-\frac{\delta f_{\vec{k}}}{\tau_{\vec{k}}}\,, \tag{29}$$

has been assumed. Here $\tau_{\vec{k}}$ denotes the carrier's relaxation time, and $\vec{E}_{\parallel}=(E_x,E_y)$ is the projection of the electric field onto the graphene plane. The kinetic equation can be solved exactly by writing $\delta f_{\vec{k}}$ as

$$\delta f_{\vec{k}}=e^{-i\omega t}\vec{k}\cdot\vec{A}_{\vec{k}}\,, \tag{30}$$

and noting that $(\vec{v}_{\vec{k}}\times\vec{B})\cdot\partial_{\vec{k}}\delta f_{\vec{k}}=\vec{v}_{\vec{k}}\cdot(\vec{B}\times\partial_{\vec{k}}\delta f_{\vec{k}})$, in order to obtain after some algebra

$$\vec{A}_{\vec{k}}=\frac{1}{(1-i\omega\tau_{\vec{k}})^2+\omega_c^2\tau_{\vec{k}}^2}\begin{pmatrix}1-i\omega\tau_{\vec{k}} & -\tau_{\vec{k}}\omega_c\\ \tau_{\vec{k}}\omega_c & 1-i\omega\tau_{\vec{k}}\end{pmatrix}\vec{\mathcal{E}}_{\vec{k}}\,, \tag{31}$$

where $\vec{\mathcal{E}}$ is defined as

$$\vec{\mathcal{E}}_{\vec{k}}=-e\frac{\partial f_0}{\partial\epsilon}(E_x v_{\vec{k},x},E_y v_{\vec{k},y})\,, \tag{32}$$

and

$$\omega_c=ev_F^2B/|E_F| \tag{33}$$

is the cyclotron frequency in graphene. Introducing the explicit form of $\delta f_{\vec{k}}$ in Eq. (26), and assuming $T=0$,

$$-\frac{\partial f_0}{\partial\epsilon}=\delta(\epsilon-E_F)\,, \tag{34}$$

one arrives at the semiclassical form of the conductivity tensor:

$$\sigma_{xx}(B,\omega)=\frac{e^2}{h}\frac{2|E_F|}{\hbar}\frac{\gamma-i\omega}{(\gamma-i\omega)^2+\left[\omega_c(B)\right]^2}\,, \tag{35}$$

$$\sigma_{xy}(B,\omega)=-\frac{e^2}{h}\frac{2E_F}{\hbar}\frac{\omega_c(B)}{(\gamma-i\omega)^2+\left[\omega_c(B)\right]^2}\,, \tag{36}$$

$\sigma_{yy}(B,\omega)=\sigma_{xx}(B,\omega)$, and $\sigma_{yx}(B,\omega)=-\sigma_{xy}(B,\omega)$. Note that for simplicity we have expressed the result in terms of the relaxation's rate $\gamma\equiv\tau_{k_F}^{-1}$.

In the presence of a magnetic field, and for pristine graphene ($\hbar\gamma\ll$ energy scales), the Drude peak (i.e., the maximum of $\mathrm{Re}\,\sigma_{xx}$) is located at the cyclotronic frequency, reflecting the intuitive fact that the optical response (absorption) is maximum for impinging light in resonance with the frequency for cyclotronic motion, that is, $\omega=\omega_c$. We note that the Drude conductivity for zero-field [Eq. (23)] is recovered by setting $B=0$ in Eq. (35).

4. Spectrum of TM SPPs in graphene

4.1. *Dispersion relation*

Let us find the form of a p-polarized surface wave in graphene. We assume a solution of Maxwell's equations in the form

$$\vec{E} = (E_{m,x}, 0, E_{m,z}) e^{iqx} e^{-\kappa_m |z|} \,, \tag{37}$$

$$\vec{B} = (0, B_{m,y}, 0) e^{iqx} e^{-\kappa_m |z|} \,, \tag{38}$$

where $m = 1, 2$ refers to the media 1 and 2 (see Fig. 1), waves are exponentially decaying in both directions away from the graphene sheet, and we seek the dispersion relation, $\omega = \omega(q)$, of this type of waves, with q denoting the wave number along the graphene sheet (see Fig. 2). The wave numbers κ_m are yet to be determined. In this case, Maxwell's equations (11), (13), (15) yield:

$$(-1)^m \kappa_m E_{m,x} - iq E_{m,z} = i\omega B_{m,y} \,, \tag{39}$$

$$(-1)^{m+1} \kappa_m B_{m,y} = -i\omega c^{-2} \epsilon_m E_{m,x} \,, \tag{40}$$

$$q B_{m,y} = -\omega c^{-2} \epsilon_m E_{m,z} \,, \tag{41}$$

which can be solved in terms of the amplitude of the magnetic field and allows for the determination of κ_m, that is,

$$E_{m,x} = i \frac{\kappa_m c^2}{\omega \epsilon_m} B_{m,y} (-1)^{m+1} \,, \tag{42}$$

$$E_{m,z} = -\frac{q c^2}{\omega \epsilon_m} B_{m,y} \,, \tag{43}$$

$$\kappa_m^2 = q^2 - \omega^2 \epsilon_m / c^2 \,, \tag{44}$$

with $B_{m,y}$ a constant. The SPP spectrum follows from the boundary conditions (6) and (7):

$$E_{1,x} = E_{2,x} \Leftrightarrow B_{1,y} = -\frac{\kappa_2 \epsilon_1}{\kappa_1 \epsilon_2} B_{2,y} \,, \tag{45}$$

$$B_{1,y} = B_{2_y} - \sigma_{xx} E_{1,x} \,, \tag{46}$$

from which we obtain the dispersion relation (in an implicit form, since both κ_m and σ_{xx} depend on frequency)

$$1 + \frac{\kappa_1 \epsilon_2}{\epsilon_1 \kappa_2} + i\sigma_{xx} \frac{\kappa_1}{\varepsilon_0 \omega \epsilon_1} = 0 \,;$$

$$\frac{\epsilon_1}{\kappa_1} + \frac{\epsilon_2}{\kappa_2} + i \frac{\sigma_{xx}}{\varepsilon_0 \omega} = 0 \,. \tag{47}$$

We note that Eq. (47) has real solutions only when the imaginary part of the conductivity is positive. This takes place when the conductivity is dominated by the Drude contribution. If the real part of the conductivity is finite (non-zero), the solutions are necessarily complex. Eq. (47) gives the spectrum of the $p-$polarized

SPPs in graphene. When the two media are the same ($\epsilon_1 = \epsilon_2 = \epsilon$), we obtain a simpler relation for the spectrum,

$$1 + i\frac{\sigma_{xx}}{2\omega\epsilon_0\epsilon}\sqrt{q^2 - \omega^2\epsilon/c^2} = 0\,. \tag{48}$$

Notice that starting from the boundary condition (8) would lead to the same spectrum. It can be shown as follows. From the continuity equation

$$\partial_t \rho_s(x,t) + \vec{\nabla}\cdot\vec{J}_s(x,t) = 0\,, \tag{49}$$

follows $-i\omega\rho_s + iq\sigma_{xx}E_{1,x} = 0$. Thus, the boundary condition reduces to $E_{1,z}\epsilon_1 - E_{2,z}\epsilon_2 = k_x\sigma_{xx}E_{1,x}/(\omega\epsilon_0)$. Using the relation (43), we obtain

$$-B_{1,y} + B_{2,y} = \sigma_{xx}E_{1x}\,, \tag{50}$$

which is the same as Eq. (46).

4.2. *Simplified analytical form*

Let us obtain some simple analytical results for the spectrum of the SPPs in graphene. We assume that the conductivity of graphene is given by the Drude contribution only. Ignoring absorption ($\gamma = 0$), we have

$$\sigma_D \approx i\frac{\nu}{\omega}, \qquad \nu = \sigma_0\frac{4E_F}{\pi\hbar}\,. \tag{51}$$

Furthermore, assuming $\epsilon_2 = \epsilon_1 = \epsilon$, the equation for the SPPs spectrum reads

$$\frac{1}{\kappa} = \frac{\nu}{2\epsilon\epsilon_0\omega^2}\,. \tag{52}$$

Inverting and squaring, we obtain

$$\omega^4 = \left(\frac{\nu}{2\epsilon\epsilon_0}\right)^2(q^2 - \omega^2\epsilon/c^2)\,. \tag{53}$$

When $\omega \to 0$, we obtain from Eq. (53) $\omega = vq$, where $v = c/\sqrt{\epsilon}$ is the speed of light in the dielectric. In the electrostatic limit (also dubbed non-retarded or plasmon approximation) we consider $\omega^2/v^2 \ll q^2$, in which case we obtain

$$\hbar^2\omega^2 = q\frac{\hbar^2\nu}{2\epsilon\epsilon_0} = \frac{2\alpha E_F}{\epsilon}\hbar cq\,, \tag{54}$$

where

$$\alpha = \frac{e^2}{4\pi\epsilon_0\hbar c} \approx \frac{1}{137} \tag{55}$$

is the fine-structure constant. We note that Eq. (54) coincides with the spectrum of plasmons in graphene. Since $E_F = v_F\hbar k_F$, the spectrum depends on the electronic density as $n_e^{1/4}$, which is specific to graphene and was experimentally confirmed [64].

We now derive the spectrum of the SPPs taking into account absorption. In this case we have to use the full form of σ_D. The dispersion relation now reads,

$$\kappa = \frac{2\epsilon\epsilon_0}{\nu}(\omega^2 + i\gamma\omega)\,. \tag{56}$$

In the electrostatic limit we write $\kappa \approx q = q' + iq''$ (assuming $q'' \ll q'$), which is now a complex quantity due to a non-zero γ. In this case, the SPP spectrum is obtained from

$$q' + iq'' = \frac{2\epsilon\epsilon_0}{\nu}(\omega^2 + i\gamma\omega), \tag{57}$$

where we have assumed $\gamma \ll \omega$. In terms of q', the spectrum is

$$\omega^2 = q'\frac{\nu}{2\epsilon\epsilon_0}\,, \tag{58}$$

which has the same functional form as in Eq. (54). The decay of the wave as it propagates in space is characterized by q'',

$$q'' = \frac{2\epsilon\epsilon_0}{\nu}\gamma\omega\,, \tag{59}$$

from which follows

$$\frac{q''}{q'} = \frac{\gamma}{\omega}\,, \tag{60}$$

that is, the decay is less pronounced at higher frequencies and smaller γ. The confinement of the electromagnetic field in the z direction (i.e. its penetration depth in the dielectrics surrounding the graphene sheet) is given by κ^{-1}. In the electrostatic limit, from Eq. (54) we have:

$$\kappa \approx q = \omega^2\frac{2\epsilon\epsilon_0}{\nu}\,. \tag{61}$$

In the dielectric the wave number of light is $k = \omega/v$. Comparing κ with k we obtain:

$$\frac{\kappa}{k} \approx \frac{2\epsilon\epsilon_0 v}{\nu}\omega = \frac{\sqrt{\epsilon}}{2\alpha}\frac{\hbar\omega}{E_F} \approx \frac{137}{2}\sqrt{\epsilon}\frac{\hbar\omega}{E_F}\,. \tag{62}$$

Thus, the ER penetration depth decreases with ϵ and with the photon frequency and increases with the Fermi energy. Considering, as an example, $\omega/(2\pi) = 10$ THz, $E_F = 0.2$ eV, and $\epsilon = 4$, we obtain $\kappa^{-1} \approx 0.035k^{-1}$, a fairly high degree of confinement in comparison with the wavelength.

4.3. *Numerical results*

In the general case of different dielectrics, neglecting absorption, Eq. (47) can be written as

$$\frac{\epsilon_1}{\sqrt{(\hbar cq)^2 - \epsilon_1(\hbar\omega)^2}} + \frac{\epsilon_2}{\sqrt{(\hbar cq)^2 - \epsilon_2(\hbar\omega)^2}} = \frac{4\alpha E_F}{(\hbar\omega)^2}\,, \tag{63}$$

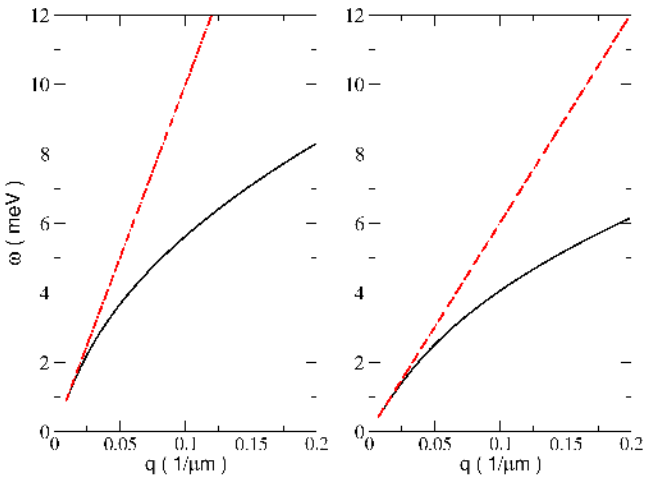

Fig. 4. SPP dispersion curves calculated taking into account only the imaginary part of the conductivity (thus q is real). We have chosen $\hbar\gamma = \Gamma = 0$ and $E_F = 0.45$ eV. Left: $\epsilon_1 = 3$ and $\epsilon_2 = 4$; right: $\epsilon_1 = 1$ and $\epsilon_2 = 11$ (silicon). The straight (dashed) line stands for the light dispersion $\hbar\omega = \hbar cq/\sqrt{\epsilon_2}$ in the medium 2 (that with higher dielectric constant).

which is convenient for numerical purposes. [In the numerical calculations we take $\hbar c = 0.2$ eV$\cdot\mu$m; it is also useful to recall that $\omega/(2\pi)$ =1 THz corresponds to an energy of 4.1 meV and to a wavelength of 300 μm.]

In the non-retarded approximation it is possible to derive from Eq. (63) analytical results which coincide with those of the previous section upon the replacement $\epsilon \to (\epsilon_1 + \epsilon_2)/2 \equiv \bar{\epsilon}$, that is,

$$\hbar\Omega_p \approx \sqrt{2\alpha E_F \hbar cq/\bar{\epsilon}}\,. \tag{64}$$

Note that we have used the symbol $\Omega_p \equiv \Omega_p(q)$ to denote the explicit solution of the dispersion relations; we shall keep this notation throughout the paper. In general, Eq. (63) has no analytical solution. In Fig. 4 we give the numerical solution to Eq. (63) in two different cases.

In Figs. 5 and 6 we present the low wavenumber part of the SPP spectrum, comparing the numerical solutions of Eq. (47) obtained with different levels of approximation to the optical conductivity and considering the role of the damping (or homogeneous broadening) parameter, $\Gamma = \hbar\gamma$. In Fig. 5 the effect of the damping is demonstrated, taking into account the full conductivity σ_D. In this case the wavenumber q is complex, $q = q' + iq''$, where q'' describes the decay of the SPP as it propagates in space along the graphene sheet. From this figure we see that the effect of the increase of the damping is two-fold: it shifts the SPP dispersion relation toward higher energies, for the same q', and enhances the value of q'' (as expected). If one wants to have long propagation lengths for the SPPs, then Γ must be as small as possible. In the same figure we also represent the light-lines $\hbar cq/\sqrt{\epsilon_1}$

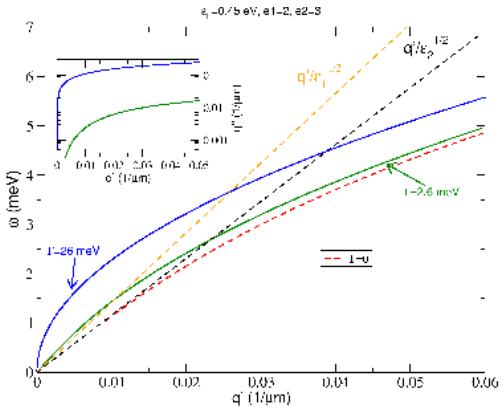

Fig. 5. Plasmon-polariton dispersion curves for $\epsilon_1 = 3$, $\epsilon_2 = 2$, considering the effect of broadening (for different values of Γ). Full expression for the conductivity with $E_F = 0.45\,\mathrm{eV}$ was included in the calculation. The red dashed line is for zero broadening. The inset shows the dependence of the imaginary part of q (q'') on the real part of q (q') (notice the logarithmic scale of the vertical axis).

and $\hbar cq/\sqrt{\epsilon_2}$, which correspond to the dispersion relations for photons propagating in the media 1 and 2, respectively. It may seem that one should be able to excite SPPs in graphene by directly shining ER on it if Γ is sufficiently large because the dispersion curves in Fig. 5 intersect the light lines, as most clearly seen for the curve corresponding to $\Gamma = 26$ meV. This is not true. For such a high value of Γ, plasmon-polaritons are overdamped (note that $q' < q''$), the "dispersion curve" ω *versus* $q' = \Re(q)$ is not quite meaningful, and the intersections do not have their usual physical meaning.

In Fig. 6 we present the effect of neglecting the real part of the optical conductivity,

$$\sigma_D \approx i\sigma_0 \frac{4E_F}{\pi\hbar} \frac{\omega}{\gamma^2 + \omega^2}\,. \tag{65}$$

The central feature is the vanishing of the dispersion curve for a finite value of q', which can be expressed as

$$q' = \frac{\epsilon_1 + \epsilon_2}{4\alpha E_F} \frac{\hbar\gamma^2}{c}. \tag{66}$$

This is a spurious result. When we use the full Drude conductivity expression, the dispersion relation vanishes at zero q'. Changing the dielectric constants of the surrounding media changes the value of q' for the same frequency, as can be seen comparing the left and right panels of Fig. 6.

4.4. *Structure with two graphene layers*

In the previous sections we have studied the SPP spectrum of single layer graphene. We have shown that the typical value of SPP's energy for wavevector $q \sim 0.1\ \mu\mathrm{m}^{-1}$

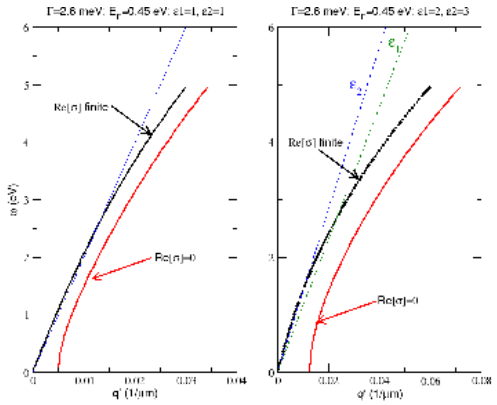

Fig. 6. SPP dispersion curves calculated considering the real part of the conductivity either finite or zero (but keeping γ finite in the imaginary part) for cases of equal (left: $\epsilon_1 = 1$, $\epsilon_2 = 1$) and different (right: $\epsilon_1 = 3$, $\epsilon_2 = 2$) dielectrics surrounding graphene with chemical potential $E_F = 0.45\,\text{eV}$ and damping $\hbar\gamma = 2.6\,\text{meV}$. The straight lines marked ϵ_1 and ϵ_2 refer to the light dispersion $\hbar\omega = \hbar cq/\sqrt{\epsilon_1}$ and $\hbar\omega = \hbar cq/\sqrt{\epsilon_2}$ in the dielectrics 1 and 2, respectively.

is $\hbar\omega \approx 4$ meV, corresponding to a frequency of about 1 THz. We would like to investigate the possibility of shifting the resonance frequency towards higher values. One way of achieving this is using a double-layer structure as shown in Fig. 7. The two degenerate SPP branches, associated with each of the layers, hybridize giving rise to a two branch spectrum, with one branch having higher energy than the bare spectrum for each layer.

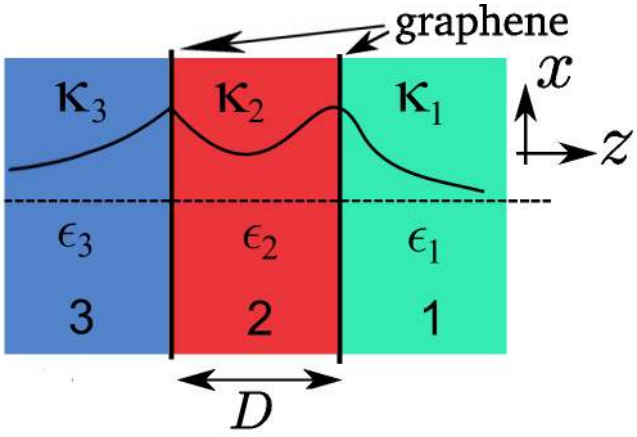

Fig. 7. Structure with two graphene layers separated by a dielectric with ϵ_2. Field profile for the E_x component of optical SPP mode is shown qualitatively.

We first compute the spectrum of the double layer system. We assume a configuration as represented in Fig. 7 with semi-infinite media 1 and 3 and a dielectric layer

2 of thickness D. Applying the boundary conditions at two interfaces and requiring exponential decay in the infinity yields:

$$\begin{bmatrix} -1 & 1 & 1 & 0 \\ \frac{\epsilon_3}{\kappa_3}+i\frac{\sigma}{\omega\epsilon_0} & -\frac{\epsilon_2}{\kappa_2} & \frac{\epsilon_2}{\kappa_2} & 0 \\ 0 & \frac{\epsilon_2 e^{\kappa_2 D}}{\kappa_2} & -\frac{\epsilon_2 e^{-\kappa_2 D}}{\kappa_2} & \left(\frac{\epsilon_1}{\kappa_1}+i\frac{\sigma}{\omega\epsilon_0}\right)e^{-\kappa_1 D} \\ 0 & e^{\kappa_2 D} & e^{-\kappa_2 D} & -e^{-\kappa_1 D} \end{bmatrix} \begin{bmatrix} E_{3,x} \\ E_{2+,x} \\ E_{2-,x} \\ E_{1,x} \end{bmatrix} = 0\,. \tag{67}$$

The spectrum is given by the vanishing of the determinant of the above matrix, that is,

$$\begin{aligned} e^{\kappa_2 D}\left(\frac{\epsilon_1}{\kappa_1}+i\frac{\sigma}{\omega\epsilon_0}+\frac{\epsilon_2}{\kappa_2}\right)\left(\frac{\epsilon_3}{\kappa_3}+i\frac{\sigma}{\omega\epsilon_0}+\frac{\epsilon_2}{\kappa_2}\right) = \\ e^{-\kappa_2 D}\left(\frac{\epsilon_1}{\kappa_1}+i\frac{\sigma}{\omega\epsilon_0}-\frac{\epsilon_2}{\kappa_2}\right)\left(\frac{\epsilon_3}{\kappa_3}+i\frac{\sigma}{\omega\epsilon_0}-\frac{\epsilon_2}{\kappa_2}\right)\,. \end{aligned} \tag{68}$$

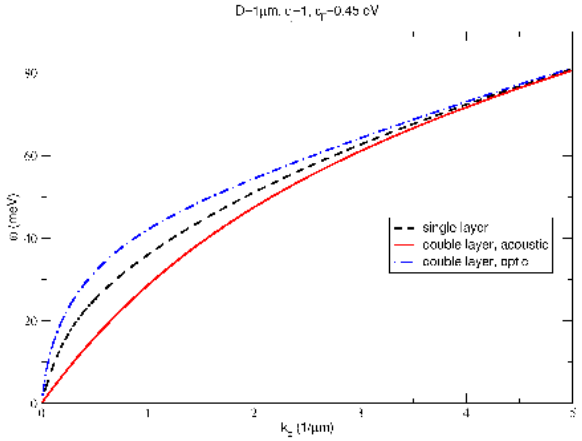

Fig. 8. Spectrum of the structure of Fig. 7, with its lower (acoustic) and upper (optical) branches. The dashed curve is the spectrum of a single layer. The parameters are $\epsilon_m = 1$ (with $m = 1, 2, 3$), $D = 1$ μm, and $E_F = 0.45$ eV.

As expected, in the limit $q_2 d \to \infty$, the two interfaces decouple and Eq. (68) reads as

$$\left(\frac{\epsilon_1}{\kappa_1}+i\frac{\sigma}{\omega\epsilon_0}+\frac{\epsilon_2}{\kappa_2}\right)\left(\frac{\epsilon_3}{\kappa_3}+i\frac{\sigma}{\omega\epsilon_0}+\frac{\epsilon_2}{\kappa_2}\right) = 0\,. \tag{69}$$

Each term in brackets represents the plasmon-polariton spectrum of one graphene layer [c.f. Eq. (47)], degenerate if $\epsilon_1 = \epsilon_3$.

In the "symmetric" case of $\epsilon_1 = \epsilon_3$, the dispersion relation (68) can be factorized,

$$\left[\left(\frac{\epsilon_1}{\kappa_1} + i\frac{\sigma}{\omega\epsilon_0}\right)\cosh(\kappa_2 D/2) + \frac{\epsilon_2}{\kappa_2}\sinh(\kappa_2 D/2)\right] \times \left[\left(\frac{\epsilon_1}{\kappa_1} + i\frac{\sigma}{\omega\epsilon_0}\right)\sinh(\kappa_2 D/2) + \frac{\epsilon_2}{\kappa_2}\cosh(\kappa_2 D/2)\right] = 0. \quad (70)$$

The first product term in Eq. (70) corresponds to the symmetric mode with the electric field z dependence even with respect to $z = D/2$ [$E_x(x,0) = E_x(x,D)$], while the second term describes the antisymmetric mode, odd with respect to the central plane [$E_x(x,0) = -E_x(x,D)$].

Another analytic limit is that of $\epsilon_1 = \epsilon_2 = \epsilon_3 = \epsilon$ and $q \gg \omega\epsilon^{1/2}/c$ (non-retarded or plasmon approximation). In this case, Eq. (70) reduces to

$$2\epsilon e^{qD} + i\frac{q\sigma}{\omega\epsilon_0}(e^{qD} \pm 1) = 0\,, \quad (71)$$

where upper and lower signs correspond to the first (symmetric) and second (antisymmetric) terms in (70), respectively. If we assume that the conductivity of graphene is given by Eq. (51), it is possible to obtain a close form for the spectrum of the surface waves,

$$\hbar^2\Omega_p^2 \approx \frac{2\alpha E_F}{\epsilon}\hbar qc\left(1 \pm e^{-qD}\right)\,. \quad (72)$$

Note that for $qD \gtrsim 0$ the spectrum given by Eq. (72) becomes inaccurate since the condition $qD \gg \omega q\epsilon^{1/2}/c$ is violated. In this regime the spectrum can only be obtained numerically. In Fig. 8 we give the numerical solution of Eq. (68) and obtain the two branches of the spectrum; clearly they both vanish at zero q. The optical (symmetric) branch lies above the dispersion curve of a single graphene layer and the acoustic (antisymmetric) branch is below it. This dependence can be obtained analytically as well by inspection of Eqs. (72) and (54).

The propagation of TM-waves in multilayer graphene-based structures, under strong light illumination, was considered by Dubinov *et al.* [92].

5. Spectrum of TE SPPs in graphene

A broadband polarizer based of on the propagation of TE-surface waves on graphene has been demonstrated [93]. It is, therefore, interesting to compute the properties of a TE surface-wave. Let us find the spectrum of an $s-$polarized (TE) surface wave in graphene. These type of waves do not exist in the traditional 2D electron gas because the imaginary part of the conductivity is always positive. We assume a solution of Maxwell's equations in the form

$$\vec{B} = (B_{m,x}, 0, B_{m,z})e^{iqx}e^{-\kappa_m|z|}\,, \quad (73)$$

$$\vec{E} = (0, E_{m,y}, 0)e^{iqx}e^{-\kappa_m|z|}\,, \quad (74)$$

where $m = 1, 2$ refers to the media 1 and 2 (see Fig. 1). In the case under consideration the boundary conditions (6) and (7) are represented as

$$E_{1,y} = E_{2,y}\,, \tag{75}$$

$$B_{1,x} - B_{2,x} = \mu_0 \sigma_{yy} E_{1,y}\,. \tag{76}$$

For this particular case, Maxwell's equations (10), (12) and (14) read

$$\begin{aligned} (-1)^{m+1}\kappa_m E_{m,y} &= -i\omega B_{m,x}\,, \\ iqE_{m,y} &= i\omega B_{m,z}\,, \\ (-1)^{m+1}\kappa_m B_{m,x} - iqB_{m,z} &= -ic^{-2}\epsilon_m \omega E_{m,y}\,, \end{aligned} \tag{77}$$

and we obrain the relations:

$$B_{m,x} = (-1)^{m+1} i \frac{\kappa_m}{\omega} E_{m,y}\,, \tag{78}$$

$$B_{m,z} = \frac{q}{\omega} E_{m,y}\,, \tag{79}$$

$$\kappa_m^2 = q^2 - \frac{\omega^2}{c^2}\epsilon_m\,; \qquad m = 1, 2\,. \tag{80}$$

From the first boundary condition it follows $E_{1,y} = E_{2,y}$ and the second boundary condition (76) yields the spectrum of the TE-waves [94],

$$\kappa_1 + \kappa_2 - i\omega\mu_0\sigma_{yy} = 0\,. \tag{81}$$

We note that Eq. (81) has real solutions if and only if the imaginary part of the conductivity is negative (and the real part of the conductivity is zero). For $\sigma' > 0$ the wave is damped by the imaginary part of either q or ω, depending on the excitation conditions. Since the imaginary part of the Drude conductivity is positive, this contribution alone cannot give rise to TE-waves. On the other hand, the interband contribution to σ'' is negative. Therefore, when the two contributions, for a given frequency, add to a negative number, TE SPPs can propagate in graphene.

Eq. (81) cannot be solved analytically. However, the third term is small because it is proportional to the fine structure constant. Then, in the simple case where $\epsilon_1 = \epsilon_2 = \epsilon$, the spectrum of the TE wave is essentially equal to $\hbar\omega \lesssim \hbar cq/\sqrt{\epsilon}$, that is, the dispersion relation of a free wave in a dielectric. Only close to the threshold for interband transitions, $\hbar\omega = 2E_F$, does the spectrum deviates considerably from this result.

6. Excitation of SPPs by evanescent waves

6.1. *ATR configuration*

As discussed above, excitation of SPPs on a flat metal surface is not possible by direct illumination (excepting the case of a periodically modulated conductivity; see Sec. 8.2). It is because the wave vector of the SPP, at a given frequency, is much larger than that of the impinging radiation. One way out is excitation by evanescent waves. We assume an attenuated total reflection (ATR) configuration of the form

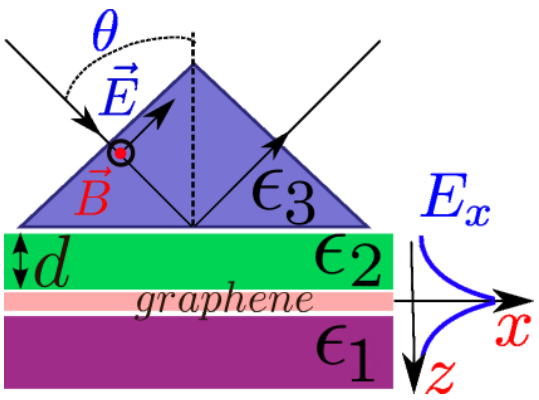

Fig. 9. Schematic representation of the experimental ATR setup needed to excite surface plasmon-polaritons in graphene (Otto configuration). The graphene layer is located between two dielectric media of relative permittivity ϵ_1 (considered semi-infinite) and ϵ_2 (of thickness d). On top of the latter there is a prism of relative permittivity $\epsilon_3 > (\epsilon_1, \epsilon_2)$ (which is a necessary condition for total internal reflection). The incident angle of the incoming $p-$polarized wave is θ, and the electric and magnetic fields are $\vec{E} = (E_x, 0, E_z)$ and $\vec{B} = (0, B_y, 0)$, respectively.

depicted in Fig. 9. Electromagnetic radiation coming from the prism impinges into the interface 3-2 at an angle θ larger than the critical angle for total internal reflection, $\theta > \arcsin\left[\sqrt{\max(\epsilon_1, \epsilon_2)/\epsilon_3}\right]$. So, only evanescent waves can exist in the layer with ϵ_2 (of thickness d) and in the half-space ϵ_1. In this configuration it becomes possible to couple the incident wave to the SPPs in graphene because the dielectric constant of the prism is larger than those of the dielectrics cladding graphene.

6.2. *Fields in the ATR regime*

We start by deriving the fields in the media 1, 2 and 3 (refer to Fig. 10). The incoming wave vector is $\vec{k}_i = (k\sin\theta, 0, k\cos\theta)$ and the reflected one at the interface is $\vec{k}_r = (k\sin\theta, 0, -k\cos\theta)$. Due to translational invariance, the component $q = k\sin\theta$ is conserved at all interfaces.

We study the case of TM-waves, that is, the fields have the form $\vec{B}_m = (0, B_{m,y}, 0)$ and $\vec{E}_m = (E_{m,x}, 0, E_{m,z})$ $(m = 1-3)$. If we further assume that $\vec{B}_3 = \vec{B}^{(i,r)} e^{i\vec{k}_{i,r}\cdot\vec{r}}$ and $\vec{E}_3 = \vec{E}^{(i,r)} e^{i\vec{k}_{i,r}\cdot\vec{r}}$, it follows from the Maxwell's equations that

$$k = \omega\varepsilon_3^{1/2}/c\,, \tag{82}$$

$$B_y^{(i,r)} = \pm\frac{\epsilon_3\omega}{c^2 k_z} E_x^{(i,r)}\,, \tag{83}$$

$$E_z^{(i,r)} = \mp\frac{q}{k_z} E_x^{(i,r)}\,. \tag{84}$$

Here $k_z = k\cos\theta$. In Eqs. (83)-(84) the upper and lower signs correspond to the incident and reflected waves, respectively. On the other hand, if we assume that $\vec{B}_m = \vec{B}_m^{(\pm)} e^{iqx} e^{\pm\kappa_m z}$ and $\vec{E}_m = \vec{E}_m^{(\pm)} e^{iqx} e^{\pm\kappa_m z}$, a situation corresponding to

evanescent or exponentially growing waves [simple generalization of Eqs. (37)-(38)], we find

$$B_{m,y}^{(\pm)} = \pm i \frac{\omega \epsilon_m}{c^2 \kappa_m} E_{m,x}^{(\pm)} , \tag{85}$$

$$E_{m,z}^{(\pm)} = \mp i \frac{q}{\kappa_m} E_{m,x}^{(\pm)} , \tag{86}$$

and the dispersion relation is equivalent to (44). Since q is conserved, we have:

$$\kappa_2^2 = \frac{\omega^2}{c^2} \epsilon_3 \sin^2\theta - \frac{\omega^2}{c^2} \epsilon_2 > 0 \Leftrightarrow \sin\theta > \left(\frac{\epsilon_2}{\epsilon_3} \right)^{1/2} . \tag{87}$$

The last condition means that evanescent waves can occur in the medium 2 if and only if $\epsilon_3 > \epsilon_2$. For the geometry of Fig. 10, the boundary conditions at the interfaces

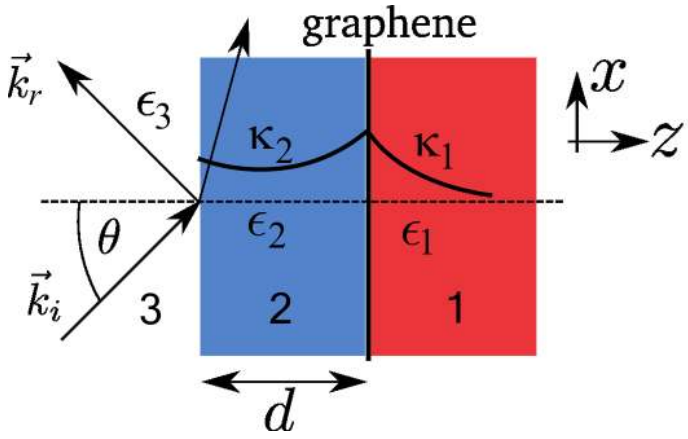

Fig. 10. Three dielectrics with $\epsilon_3 > \epsilon_1, \epsilon_2$. Between the dielectrics 1 and 2 there is a graphene sheet.

$z = d$ and $z = 0$ read as

$$E_{m,x} = E_{m+1,x} , \tag{88}$$

$$B_{m,y} = B_{m+1,y} - \mu_0 \sigma \delta_{m,1} E_{m,x} , \tag{89}$$

respectively, where $\delta_{m,m'}$ is the Kronecker symbol.

6.3. *Total reflection*

Let us assume that $d \to \infty$ and the graphene sheet and the medium 1 have no effect on the reflection at the interface 2-3. We shall show that, for $\theta_c = \arcsin(\epsilon_2/\epsilon_3)^{1/2}$, the reflection is total, even though there is an evanescent wave in the medium 2. For this particular case the boundary conditions are written as $E_x^{(i)} + E_x^{(r)} = E_{2,x}^{(-)}$ and $B_y^{(i)} + B_y^{(r)} = B_{2,y}^{(-)}$, where the subscripts i and r stand for incident and reflected

waves as before. Explicitly, the second boundary condition reads

$$\frac{\epsilon_3}{k_z}E_x^{(i)} - \frac{\epsilon_3}{k_z}E_x^{(r)} = -i\frac{\epsilon_2}{\kappa_2}E_{2,x}^{(-)}\,, \tag{90}$$

with the following solution,

$$r \equiv \frac{E_x^{(r)}}{E_x^{(i)}} = \frac{\epsilon_3\kappa_2 + i\epsilon_2 k_z}{\epsilon_3\kappa_2 - i\epsilon_2 k_z} = e^{2i\alpha}\,, \tag{91}$$

where we have defined $\alpha = \arctan(\epsilon_2 k_z/\epsilon_3\kappa_2)$. Note that for grazing incidence $\alpha = 0$, while for $\theta = \theta_c$ we have $\kappa_2 = 0$ and $\alpha = \pi/2$. We thus conclude that total reflection ($|r|^2 = 1$) occurs for $\theta \geq \theta_c$. The amplitude of the evanescent field reads

$$\frac{E_{2,x}^{(-)}}{E_x^{(i)}} = \frac{2\epsilon_3\kappa_2}{\epsilon_3\kappa_2 - i\epsilon_2 k_z} = \frac{2\epsilon_3\kappa_2}{\epsilon_3\kappa_2 - i\epsilon_2 k\cos\theta}\,, \tag{92}$$

where $\kappa_2 = k\sqrt{\sin^2\theta - \epsilon_2/\epsilon_3} < k$. We show in the next section that the presence of a graphene layer, as in Fig. 10, can frustrate the total reflection in a dramatic way.

6.4. *Otto configuration: p−polarized wave*

6.4.1. *Reflection coefficient*

We shall now compute the reflection coefficient in the situation represented in Fig. 10, where we have three dielectrics, a graphene layer at the 2-3 interface, and $\theta > \theta_c$. We will see that in this case $|r|^2$ can be smaller than unity (down to zero) due to the excitation of SPPs waves in the graphene layer.

In the dielectric 3 we have both incoming and reflected waves, while in the dielectric 2 we can have both evanescent and exponentially growing solutions because this region has a finite thickness d. In the dielectric 1 only evanescent waves can occur.

The fields in the three regions are:

Region 3

$$B_{3,y} = B_y^{(i)}e^{i\vec{k}_i\cdot\vec{r}} + B_y^{(r)}e^{i\vec{k}_r\cdot\vec{r}}\,, \tag{93}$$

$$\vec{E}_3 = \left(E_x^{(i)}, 0, E_z^{(i)}\right)e^{i\vec{k}_i\cdot\vec{r}} + \left(E_x^{(r)}, 0, E_z^{(r)}\right)e^{i\vec{k}_r\cdot\vec{r}}\,. \tag{94}$$

Region 2

$$B_{2,y} = B_{2,y}^{(+)}e^{i\vec{k}_2^{(+)}\cdot\vec{r}} + B_{2,y}^{(-)}e^{i\vec{k}_2^{(-)}\cdot\vec{r}}\,, \tag{95}$$

$$\vec{E}_2 = \left(E_{2,x}^{(+)}, 0, E_{2,z}^{(+)}\right)e^{i\vec{k}_2^{(+)}\cdot\vec{r}} + \left(E_{2,x}^{(-)}, 0, E_{2,z}^{(-)}\right)e^{i\vec{k}_2^{(-)}\cdot\vec{r}}\,, \tag{96}$$

Region 1

$$B_{1,y} = B_{1,y}^{(-)}e^{i\vec{k}_1^{(-)}\cdot\vec{r}}\,, \tag{97}$$

$$\vec{E}_1 = \left(E_{1,x}^{(-)}, 0, E_{1,z}^{(-)}\right)e^{i\vec{k}_1^{(-)}\cdot\vec{r}}\,, \tag{98}$$

where $\vec{k}_m^{(\pm)} = (k\sin\theta, 0, \mp i\kappa_m)$, $m = 1, 2$. The boundary conditions at the interfaces $z = 0$ and $z = d$ are:

$$E_x^{(i)} + E_x^{(r)} = E_{2,x}^{(+)} + E_{2,x}^{(-)}\,, \tag{99}$$

$$B_y^{(i)} + B_y^{(r)} = B_{2,y}^{(+)} + B_{2,y}^{(-)}\,. \tag{100}$$

$$E_{1,x}^{(-)} e^{-\kappa_1 d} = E_{2,x}^{(+)} e^{\kappa_2 d} + E_{2,x}^{(-)} e^{-\kappa_2 d}\,, \tag{101}$$

$$B_{1,y}^{(-)} e^{-\kappa_1 d} = B_{2,y}^{(+)} e^{\kappa_2 d} + B_{2,y}^{(-)} e^{-\kappa_2 d} - \mu_0\sigma_{xx} E_{1,x}^{(-)} e^{-\kappa_1 d}\,. \tag{102}$$

Explicitly, using relations (83) and (85), we can rewrite Eqs. (100) and (102) in terms of the x-component of the electric field,

$z = 0$:

$$-\frac{\epsilon_3}{k_z} E_x^{(i)} + \frac{\epsilon_3}{k_z} E_x^{(r)} = -i\frac{\epsilon_2}{\kappa_2} E_{2,x}^{(+)} + i\frac{\epsilon_2}{\kappa_2} E_{2,x}^{(-)}\,; \tag{103}$$

$z = d$:

$$-\frac{\omega\epsilon_2}{\kappa_2} e^{\kappa_2 d} E_{2,x}^{(+)} + \frac{\omega\epsilon_2}{\kappa_2} e^{-\kappa_2 d} E_{2,x}^{(-)} = \left(\frac{\omega\epsilon_1}{\kappa_1} + i\frac{\sigma}{\epsilon_0}\right) e^{-\kappa_1 d} E_{1,x}^{(-)}\,. \tag{104}$$

After the elimination of $E_{1,x}^{(-)}$, the linear system of equations defined by the boundary conditions can be written as

$$\Xi_p \begin{bmatrix} E_x^{(r)}/E_x^{(i)} \\ E_{2,x}^{(+)}/E_x^{(i)} \\ E_{2,x}^{(-)}/E_x^{(i)} \end{bmatrix} = \Phi_p, \tag{105}$$

where

$$\Xi_p = \begin{bmatrix} -1 & 1 & 1 \\ \kappa_2\epsilon_3 & ik_z\epsilon_2 & -ik_z\epsilon_2 \\ 0 & e^{\kappa_2 d}(\kappa_2\Lambda_1^{(+)} + \chi_1) & e^{-\kappa_2 d}(\kappa_2\Lambda_1^{(+)} - \chi_1) \end{bmatrix}, \tag{106}$$

$$\Phi_p = \begin{bmatrix} 1 \\ \kappa_2\epsilon_3 \\ 0 \end{bmatrix}, \tag{107}$$

$$\chi_m = \kappa_m\omega\epsilon_{m+1}\,, \tag{108}$$

$$\Lambda_m^{(\pm)} = (\omega\epsilon_m \pm i\sigma\kappa_m/\epsilon_0)\,. \tag{109}$$

The solution of the linear system yields:

$$E_x^{(r)}/E_x^{(i)} = \frac{\kappa_2\epsilon_3\eta_1 + ik_z\epsilon_2\eta_2}{\kappa_2\epsilon_3\eta_1 - ik_z\epsilon_2\eta_2}\,, \tag{110}$$

$$\frac{E_{1,x}^{(-)} e^{-\kappa_1 d}}{E_x^{(i)}} = \frac{E_{2,x}^{(+)}}{E_x^{(i)}} e^{\kappa_2 d} + \frac{E_{2,x}^{(-)}}{E_x^{(i)}} e^{-\kappa_2 d} = \frac{2\omega\epsilon_2\kappa_1\kappa_2\epsilon_3}{\kappa_2\epsilon_3\eta_1 - ik_z\epsilon_2\eta_2}\,, \tag{111}$$

where $\eta_1 = \kappa_2\Lambda_1^{(+)}\sinh(\kappa_2 d) + \cosh(\kappa_2 d)\chi_1$ and $\eta_2 = \kappa_2\Lambda_1^{(+)}\cosh(\kappa_2 d) + \sinh(\kappa_2 d)\chi_1$. We note that, if the conductivity has an imaginary part only, then

the function $\Lambda_1^{(+)}$ is real and the reflection coefficient is simply a phase. Therefore, the reflectance is equal to unity. Thus, for detecting the excitation of a surface wave the conductivity of graphene must have a finite real part. In Fig. 11 we represent the reflectance and the absorbance as functions of the energy of the incoming ER. A sharp dip in the reflectance spectrum is seen at an energy of about $\hbar\omega \approx 4$ meV.

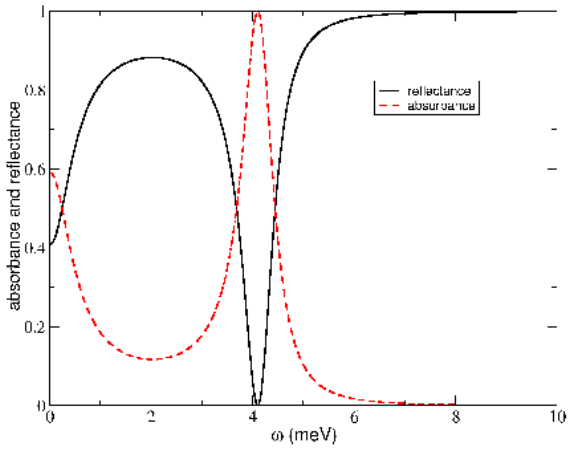

Fig. 11. Absorbance and reflectance spectra of graphene in the Otto configuration. The parameters are: $E_F = 0.45$ eV, $\Gamma = 0.1$ meV, ϵ_1=14, $\epsilon_2 = 1$, $\epsilon_3 = 5$, $d = 2.51$ μm, $\theta_c = 36.7^o$, and $\theta_i = 2.25\theta_c$. Solid black line: $|r|^2$; Red dashed line: 1-$|r|^2$. In the calculation we have used the Drude formula for the conductivity of graphene, Eq. (23).

We also note a reduction of the reflectance close to zero energy. We want to understand why the reflectance falls to zero at these two energy values. First, we make a three-dimensional representation (Fig. 12), where the absorbance is represented as function of both the angle of incidence and the incoming photon energy for a given width d. Maximal absorbance (minimal reflectance) occurs close to zero and 4 meV, and is accompanied by a drastic change (from positive to negative values) of the phase of the reflection coefficient as depicted in Fig. 12. The comparison of top and bottom panels in Fig. 12 shows that the resonance maximum of absorbance corresponds to maximal amplitude for excited SPPs and phase $\approx -\pi/2$. The latter imposes the fulfillment of the condition $\mathrm{Re}(E_{1,x}^{(-)} e^{-\kappa_1 d}) \approx 0$ at resonance, which, after taking into account Eq. (111), leads to the following constraint:

$$\mathrm{Re}(\eta_1) = \left(\frac{\epsilon_1}{\kappa_1} - \frac{\sigma''}{\omega \epsilon_0} \right) \sinh(\kappa_2 d) + \frac{\epsilon_2}{\kappa_2} \cosh(\kappa_2 d) = 0 \,. \tag{112}$$

Eq. (112) determines the frequency onset ω_{min}, and its main idea can be interpreted in the following manner. In the limit $d \to \infty$ this equation can be obtained by the substitution of the relation (known as ATR scanline),

$$k_{\mathrm{SPP}} = q = k \sin\theta = \frac{\omega}{c} \sqrt{\epsilon_3} \sin\theta \,, \tag{113}$$

into the SPP dispersion relation (63). Rearranging Eq. (113), the energy of the photon reads

$$\hbar\omega_\gamma = \frac{q\hbar c}{\sqrt{\epsilon_3}\sin\theta}\,. \tag{114}$$

It becomes possible to excite SPPs when the in-plane momentum of the photon (113) coincides with the momentum of the SPPs at the same frequency. Under this condition, the value of the reflectance at minimum can be represented as

$$R_{\min} = \frac{\omega\epsilon_3\kappa_1^2\kappa_2^2\frac{\sigma'}{\epsilon_0} - k_z\left[(\omega\epsilon_1 - \frac{\sigma''}{\epsilon_0}\kappa_1)^2\kappa_2^2 - (\omega\epsilon_2\kappa_1)^2\right]}{\omega\epsilon_3\kappa_1^2\kappa_2^2\frac{\sigma'}{\epsilon_0} + k_z\left[(\omega\epsilon_1 - \frac{\sigma''}{\epsilon_0}\kappa_1)^2\kappa_2^2 - (\omega\epsilon_2\kappa_1)^2\right]}. \tag{115}$$

Notice that the expression (115) must be evaluated at $\omega = \omega_{\min}$.

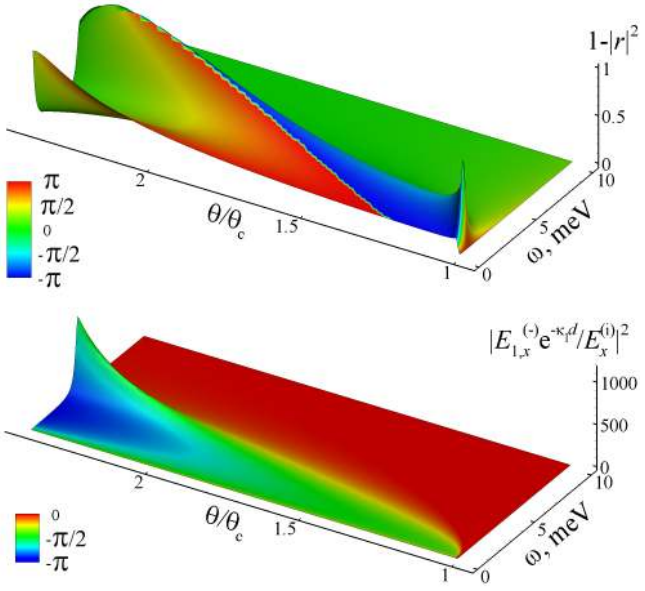

Fig. 12. Absorbance, 1-$|r|^2$, (top), and the electric field squared amplitude, $|E^{(-)}_{1,x}e^{-\kappa_1 d}/E^{(i)}_x|^2$ at $z = d$ (bottom) *versus* photon energy and angle of incidence. Phases of the reflection coefficient, r (top) and the electric field (bottom) are depicted by color. Other parameters as in Fig. 11.

In Fig. 13 the reflectance and the absorbance are plotted as functions of the incident angle θ and the spacer thickness d. We see that there are some optimal values of θ and d for which the reflectance is almost zero. They correspond to an efficient excitation of SPPs in the graphene sheet.

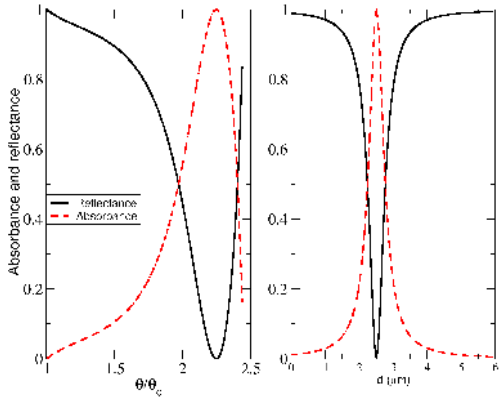

Fig. 13. Absorbance and reflectance spectra. Left: reflectance $|r|^2$ (solid line), and absorbance $1-|r|^2$ (dashed line), as function of the angle of incidence θ/θ_c. Right: reflectance $|r|^2$ (solid line), and absorbance $1-|r|^2$ (dashed line), as function of the spacer thickness, d. In both panels the photon energy is $\hbar\omega = 4.1$ meV and other parameters are as in Fig. 11.

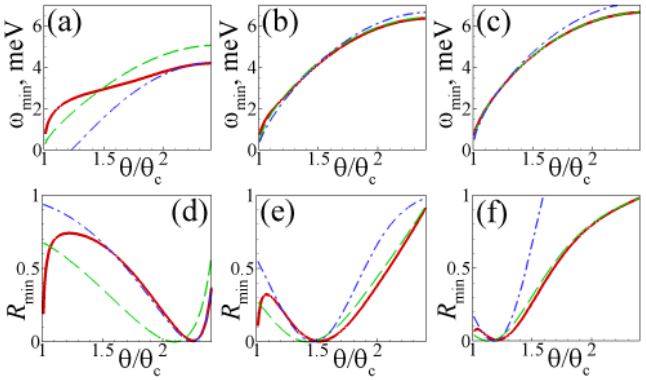

Fig. 14. Dependence of the resonant frequency $\omega_{\rm min}$ (a–c), and reflectance at resonance $R_{\rm min}$ (d–f) upon angle of incidence θ, obtained from numerical calculation [red solid line], approximations (119) [blue dashed-dotted line] and (122) [green dashed line]. The parameters are: $d = 2.51$ μm (a,d), $d = 7.53$ μm (b,e), and $d = 12.55$ μm (c,f). Other parameters as in Fig. 11.

6.4.2. *The limit* $\kappa_2 d \ll 1$

Putting $\kappa_2 d = 0$ in Eq. (110), we find:

$$\frac{E_x^{(r)}}{E_x^{(i)}} \approx \frac{\kappa_1\omega\epsilon_3 + ik_z\Lambda_1^{(+)}}{\kappa_1\omega\epsilon_3 - ik_z\Lambda_1^{(+)}} = \frac{\xi - k_z\sigma'\kappa_1/\epsilon_0}{\xi^* + k_z\sigma'\kappa_1/\epsilon_0}\,, \tag{116}$$

where ξ is defined as

$$\xi = \omega\epsilon_3 + ik_z\omega\left(\frac{\epsilon_1}{\kappa_1} - \frac{\sigma''}{\epsilon_0\omega}\right). \tag{117}$$

The above equation is the total internal reflection (91), modified by the presence of graphene. The smallest value of $E_x^{(r)}/E_x^{(i)}$ is obtained for $\mathrm{Im}\xi = 0$, that is, for

$$\frac{\epsilon_1}{\kappa_1} - \frac{\sigma''}{\epsilon_0\omega} = 0\,, \tag{118}$$

which coincides with the dispersion relation of SPP waves with the wavenumber κ_1 in a medium of dielectric permittivity $\epsilon_1/2$. We recall, however, that the fulfilment of the condition (118) by itself does not imply an efficient excitation of SPPs because this type of electromagnetic waves cannot be excited by direct illumination. We note that Eq. (118) fixes a relation between ω and θ, which are no longer independent variables. Solving, for example, Eq. (118) for $\sin\theta$, Eq. (116) can be regarded as a function of ω only.

For finite $\kappa_2 d \ll 1$ Eq. (112) becomes

$$\omega_{\min} = \frac{\sqrt{\epsilon_3\sin^2\theta - \epsilon_1}}{\epsilon_1 d}\left[\frac{4\alpha E_F d}{\hbar} - \frac{c\epsilon_2}{\epsilon_3\sin^2\theta - \epsilon_2}\right]. \tag{119}$$

The main consequence of Eq. (119) is the existence of a low-angle cutoff, that is, SPPs can be excited only for incidence angles higher than a certain $\Theta_{\min}$,

$$\sin^2\Theta_{\min} = \frac{\epsilon_2}{\epsilon_3}\left[1 + \frac{\hbar c}{4\alpha E_F d}\right]. \tag{120}$$

This expression was obtained from Eq. (119) by setting $\omega_{\min} = 0$. Decreasing the thickness of the gap between the prism and graphene, d, leads to an increase of $\Theta_{\min}$. When the right-hand side of Eq. (120) becomes larger than unity, SPPs no longer can be excited in the full range of incidence angles θ.

The validity of approximation (119) is demonstrated explicitly in Fig. 14(a). For small d, the approximation (119) is valid for $\theta \gtrsim \Theta_{\min} \approx 1.23\theta_c$. At the same time, for $\theta \gtrsim 2.15\theta_c$ one obtains a good agreement between the approximation (119) [blue dashed-dotted line] and exact results [red solid line] both for $\omega_{\min}$ [Fig. 14(a)] and for $R_{\min}$ [Fig. 14(d)]. Finally, increasing d limits the validity of the approximation (119) to small θ only [see Figs. 14(b), 14(c), 14(e), and 14(f)].

6.4.3. *The limit* $\kappa_2 d \gg 1$

In the opposite limit of $\kappa_2 d \to \infty$, we obtain for Eq. (110)

$$\frac{E_x^{(r)}}{E_x^{(i)}} \to \frac{i\kappa_2\epsilon_3 - k_z\epsilon_2}{i\kappa_2\epsilon_3 + k_z\epsilon_2}\,, \tag{121}$$

which is equivalent to Eq. (91), as expected, because graphene is far away from the 2-3 interface. Solution of Eq. (112) by means of perturbation theory yields:

$$\omega_{\min} = \frac{4\alpha E_F}{\hbar}\left[\frac{\epsilon_1}{\sqrt{\epsilon_3\sin^2\theta-\epsilon_1}}+\frac{\epsilon_2\beta}{\sqrt{\epsilon_3\sin^2\theta-\epsilon_2}}\right]^{-1}, \tag{122}$$

where

$$\beta = \tanh^{-1}\left(\omega_0\frac{d}{c}\sqrt{\epsilon_3\sin^2\theta-\epsilon_2}\right),$$

$$\omega_0 = \frac{4\alpha E_F}{\hbar}\left[\frac{\epsilon_1}{\sqrt{\epsilon_3\sin^2\theta-\epsilon_1}}+\frac{\epsilon_2}{\sqrt{\epsilon_3\sin^2\theta-\epsilon_2}}\right]^{-1}. \tag{123}$$

Comparison of panels (a-c) in Fig. 14 demonstrates that increasing d leads to a better correspondence between the approximation (122) [green dashed lines] and the exact result [red solid lines].

6.4.4. *Transfer matrix method*

We will show now how the same problem of interaction of light with a graphene-based planar structure can be solved using the transfer matrix method [95]. Obviously, the result is the same, however, the method is suitable for systems based on graphene multi-layers, such as that of Fig. 19. Referring to Fig. 10, the boundary conditions (99) and (103) at the 3-2 interface can be written in the matrix form as

$$\begin{bmatrix}E_x^{(i)}\\E_x^{(r)}\end{bmatrix} = \frac{1}{2i\epsilon_3\kappa_2}\begin{bmatrix}\epsilon_3 & k_z\\ \epsilon_3 & -k_z\end{bmatrix}\begin{bmatrix}i\kappa_2 & i\kappa_2\\ -\epsilon_2 & \epsilon_2\end{bmatrix}\begin{bmatrix}E_{2,x}^{(+)}\\E_{2,x}^{(-)}\end{bmatrix}$$
$$\equiv M^{3\Rightarrow 2}\begin{bmatrix}E_{2,x}^{(+)}\\E_{2,x}^{(-)}\end{bmatrix}. \tag{124}$$

The determinant of $M^{3\Rightarrow 2}$ is $\det M^{3\Rightarrow 2} = ik_z\epsilon_2/(\kappa_2\epsilon_3)$. Similarly, the boundary conditions at the 2-1 interface can be written as

$$\begin{bmatrix}E_{2,x}^{(+)}\\E_{2,x}^{(-)}\end{bmatrix} = \begin{bmatrix}e^{-\kappa_2 d} & 0\\ 0 & e^{\kappa_2 d}\end{bmatrix}\frac{1}{2\chi_1}\begin{bmatrix}\chi_1 & 1\\ \chi_1 & -1\end{bmatrix}$$
$$\times\begin{bmatrix}1 & 1\\ \kappa_2\Lambda_1^{(-)} & -\kappa_2\Lambda_1^{(+)}\end{bmatrix}\begin{bmatrix}E_{1,x}^{(+)}e^{\kappa_1 d}\\E_{1,x}^{(-)}e^{-\kappa_1 d}\end{bmatrix}$$
$$\equiv M^{2\Rightarrow 1}\begin{bmatrix}E_{1,x}^{(+)}\\E_{1,x}^{(-)}\end{bmatrix}, \tag{125}$$

where $\Lambda_1^{(\pm)}$ has been defined in (109). The determinant of $M^{2\Rightarrow 1}$ is, $\det M^{2\Rightarrow 1} = \kappa_2\epsilon_1/(\kappa_1\epsilon_2)$. The full transfer matrix is $M = M^{3\Rightarrow 2}M^{2\Rightarrow 1}$ and its determinant reads:

$$\det M = i\frac{k_z\epsilon_1}{\kappa_1\epsilon_3}. \tag{126}$$

The reflection coefficient is given by

$$r \equiv \frac{E_x^{(r)}}{E_x^{(i)}} = \frac{M_{22}}{M_{12}}\,, \tag{127}$$

or explicitly,

$$\frac{E_x^{(r)}}{E_x^{(i)}} = \frac{\kappa_2 \cosh(\kappa_2 d)(\chi_1\epsilon_3 + ik_z\epsilon_2\Lambda_1^{(+)}) + \sinh(\kappa_2 d)(\kappa_2^2\epsilon_3\Lambda_1^{(+)} + ik_z\epsilon_2\chi_1)}{\kappa_2 \cosh(\kappa_2 d)(\chi_1\epsilon_3 - ik_z\epsilon_2\Lambda_1^{(+)}) + \sinh(\kappa_2 d)(\kappa_2^2\epsilon_3\Lambda_1^{(+)} - ik_z\epsilon_2\chi_1)}\,, \tag{128}$$

where M_{ij} are the elements of the matrix M. Notice, that Eq.(127) can be obtained from Eqs.(125) and (124), by putting $E_{1,x}^{(+)} \equiv 0$ which is necessary to guarantee that the field is finite at z $\to \infty$. After some algebra, Eq. (128) can be shown equivalent to Eq. (110).

6.5. *Otto configuration: s−polarized wave*

We shall now discuss the reflection of an $s-$polarized wave in the geometry depicted in Fig. 10. The wave vectors have been defined in Sec. 6.4. The fields in the three regions are given by:

Region 3

$$\vec{B}_3 = (B_x^{(i)}, 0, B_z^{(i)})e^{i\vec{k}_i\cdot\vec{r}} + (B_x^{(r)}, 0, B_z^{(r)})e^{i\vec{k}_r\cdot\vec{r}}\,, \tag{129}$$

$$E_{3,y} = E_y^{(i)}e^{i\vec{k}_i\cdot\vec{r}} + E_y^{(r)}e^{i\vec{k}_r\cdot\vec{r}}\,; \tag{130}$$

Region 2

$$\vec{B}_2 = (B_{2,x}^{(+)}, 0, B_{2,z}^{(+)})e^{i\vec{k}_2^{(+)}\cdot\vec{r}} + (B_{2,x}^{(-)}, 0, B_{2,z}^{(-)})e^{i\vec{k}_2^{(-)}\cdot\vec{r}}\,, \tag{131}$$

$$E_{2,y} = E_{2,y}^{(+)}e^{i\vec{k}_2^{(+)}\cdot\vec{r}} + E_{2,y}^{(-)}e^{i\vec{k}_2^{(-)}\cdot\vec{r}}\,; \tag{132}$$

Region 1

$$\vec{B}_1 = (B_{1,x}^{(-)}, 0, B_{1,z}^{(-)})e^{i\vec{k}_1^{(-)}\cdot\vec{r}}\,, \tag{133}$$

$$E_{1,y} = E_{1,y}^{(-)}e^{i\vec{k}_1^{(-)}\cdot\vec{r}}\,. \tag{134}$$

The boundary conditions at $z = 0,\ d$ are:

$$E_y^{(i)} + E_y^{(r)} = E_{2,y}^{(+)} + E_{2,y}^{(-)}\,; \tag{135}$$

$$B_x^{(i)} + B_x^{(r)} = B_{2,x}^{(+)} + B_{2,x}^{(-)}\,. \tag{136}$$

$$E_{1,y}^{(-)}e^{-\kappa_1 d} = E_{2,y}^{(+)}e^{\kappa_2 d} + E_{2,y}^{(-)}e^{-\kappa_2 d}\,, \tag{137}$$

$$B_{1,x}^{(-)}e^{-\kappa_1 d} = B_{2,x}^{(+)}e^{\kappa_2 d} + B_{2,x}^{(-)}e^{-\kappa_2 d} + \mu_0\sigma E_{1,y}^{(-)}e^{-\kappa_1 d}\,. \tag{138}$$

We can express the magnetic field components in terms of the electric field ones. To that end we use Maxwell's equations (10), and (12), (14) and obtain

$$B_x^{(i,r)} = \mp\frac{k_z}{\omega}E_y^{(i,r)}\,, \tag{139}$$

$$B_z^{(i,r)} = \frac{q}{\omega}E_y^{(i,r)}\,, \tag{140}$$

$$B_{m,x}^{(\pm)} = \pm i\frac{\kappa_m}{\omega}E_{m,y}^{(\pm)}\,, \tag{141}$$

$$B_{m,z}^{(\pm)} = \frac{q}{\omega}E_{m,y}^{(\pm)}\,. \tag{142}$$

These allow to write Eqs. (136) and (138) as

$$ik_zE_y^{(i)} - ik_zE_y^{(r)} = \kappa_2E_{2,y}^{(+)} - \kappa_2E_{2,y}^{(-)} \tag{143}$$

and

$$-(\kappa_1 - i\omega\mu_0\sigma)E_{1,y}^{(-)}e^{-\kappa_1 d} = \kappa_2E_{2,y}^{(+)}e^{\kappa_2 d} - \kappa_2E_{2,y}^{(-)}e^{-\kappa_2 d}\,, \tag{144}$$

respectively. The problem now reduces to the solution of the following system of linear equations:

$$\Xi_s\begin{bmatrix} E_y^{(r)}/E_y^{(i)} \\ E_{2,y}^{(+)}/E_y^{(i)} \\ E_{2,y}^{(+)}/E_y^{(i)} \end{bmatrix} = \Phi_s\,. \tag{145}$$

Here

$$\Xi_s = \begin{bmatrix} -1 & 1 & 1 \\ ik_z & \kappa_2 & -\kappa_2 \\ 0 & (\Lambda_s^{(-)} + \kappa_2)e^{\kappa_2 d} & (\Lambda_s^{(-)} - \kappa_2)e^{-\kappa_2 d} \end{bmatrix}, \tag{146}$$

$$\Phi_s = \begin{bmatrix} 1 \\ ik_z \\ 0 \end{bmatrix}, \tag{147}$$

$$\Lambda_s^{(\pm)} = \kappa_1 \pm i\mu_0\omega\sigma\,. \tag{148}$$

From the solution of 145 it follows that the reflection coefficient is given by

$$r_s = \frac{E_y^{(r)}}{E_y^{(i)}} = -\frac{\kappa_2\eta_{1,s} + ik_z\eta_{2,s}}{\kappa_2\eta_{1,s} - ik_z\eta_{2,s}}\,. \tag{149}$$

where $\eta_{1,s} = \Lambda_s^{(-)}\cosh(\kappa_2 d) + \kappa_2\sinh(\kappa_2 d)$, $\eta_{2,s} = \Lambda_s^{(-)}\sinh(\kappa_2 d) + \kappa_2\cosh(\kappa_2 d)$. We note that for $d \to \infty$, r has a pole for $\Lambda_s^{(-)} + \kappa_2 = 0$, which yields the TE-wave dispersion relation [compare with Eq. (81)].

In Fig. 15 the reflectance of a $s-$polarized wave is plotted against the photon energy and the angle of incidence. Clearly, the reflectance is close to unity everywhere excepting $\omega \to 0$. Accordingly, the absorbance, $1-|r_s|^2$, is close to zero. This behaviour contrasts with the case of $p-$polarized waves, where sharp SPP-related resonances occur. There are such dips in the reflectance depicted in Fig. 15 (note the

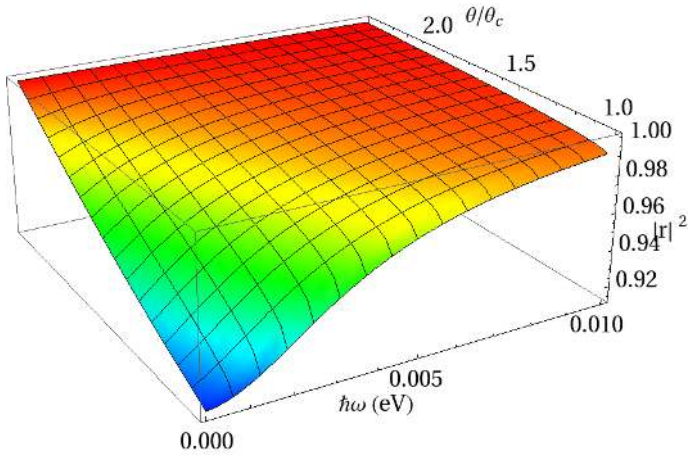

Fig. 15. Reflectance of a $s-$polarized wave in the geometry of Fig. 10. The parameters are the same of Fig. 11.

vertical scale) because the conductivity has been modelled by the Drude formula (which has $\sigma'' > 0$). Hence, TE plasmon-polaritons in graphene are not captured by the present calculation (c.f. Sec. 5).

6.6. *Otto configuration: arbitrarily polarized waves*

In the general case of an arbitrary linearly polarized wave (see Fig. 16), the incoming magnetic field is,

$$\vec{B}_i = B_i(-\cos\varphi\cos\theta, \sin\varphi, \cos\varphi\sin\theta)e^{i\vec{k}_i\cdot\vec{r}}\,. \tag{150}$$

Note that $\varphi = 0$ corresponds to a purely $s-$polarized wave, whereas $\varphi = \pi/2$ corresponds to a purely $p-$polarized wave.

The incoming electric field is obtained from Maxwell's equations as

$$\vec{E}_i = -\frac{\omega}{k^2}\vec{k}_i \times \vec{B} = \frac{\omega}{k}B_i(\sin\varphi\cos\theta, \cos\varphi, -\sin\varphi\sin\theta)e^{i\vec{k}_i\cdot\vec{r}} \tag{151}$$

and the reflected field can be written as

$$\vec{B}_r = (B_s\cos\theta, B_p, B_s\sin\theta)e^{i\vec{k}_r\cdot\vec{r}}\,. \tag{152}$$

Again, it follows from Maxwell's equations that the reflected electric field is given by

$$\vec{E}_r = -\frac{\omega}{k^2}\vec{k}_r \times \vec{B} = \frac{\omega}{k}(-B_p\cos\theta, B_s, -B_p\sin\theta)e^{i\vec{k}_r\cdot\vec{r}}\,. \tag{153}$$

It becomes clear that the arbitrarily polarized wave can be decomposed into $s-$ and $p-$polarized components, which are reflected independently. We have already

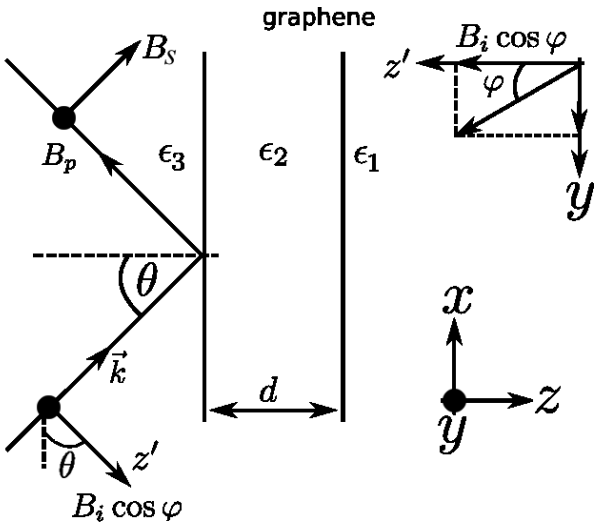

Fig. 16. Geometry for the scattering of an electromagnetic wave containing both $s-$ and $p-$polarization components.

computed the reflection coefficients for $s-$ and $p-$polarized waves. Thus, we have for the $s-$polarized component:

$$\frac{E_y^{(r)}}{E_y^{(i)}} = \frac{B_s}{B_i \cos\varphi}\,; \qquad \frac{B_s}{B_i} = \cos\varphi \frac{E_y^{(r)}}{E_y^{(i)}}\,. \tag{154}$$

For $\varphi = \pi/2$, there is no $s-$polarized reflected wave because the incoming ER is purely $p-$polarized. Notice that $E_y^{(r)}/E_y^{(i)}$ has been defined in Eq. (149).

For the $p-$polarized component we have:

$$\frac{E_x^{(r)}}{E_x^{(i)}} = -\frac{B_p}{B_i \sin\varphi}\,; \qquad \frac{B_p}{B_i} = -\sin\varphi \frac{E_x^{(r)}}{E_x^{(i)}}\,, \tag{155}$$

and $E_x^{(r)}/E_x^{(i)}$ has been defined in Eq. (110). This result implies that for $\varphi = 0$ there is no scattered $p-$polarized wave because the incoming ER is purely $s-$polarized.

In the regime where the optical conductivity of graphene is dominated by the Drude term, the excitation of a $s-$polarized surface waves in graphene is not possible because the imaginary part of the conductivity is positive (refer to Sec. 5). On the other hand, choosing the parameters of the problem appropriately (refer to Sec. 6.4), it is possible to obtain a strong absorption of the $p-$polarized component of the impinging ER. As a consequence, the setup of Fig. 9 can work as a polarizer.

If we write $B_s/B_i = A_s e^{i\delta_s}$ and $B_p/B_i = A_p e^{i\delta_p}$, the total reflected power is defined as

$$R_T = R_s + R_p = |A_s|^2 + |A_p|^2\,, \tag{156}$$

and the angle of ellipticity, ψ, is obtained from [96]

$$\tan(2\psi) = \frac{2A_pA_s}{A_s^2 - A_p^2}\cos(\delta_p - \delta_s)\,. \tag{157}$$

The angle ψ vanishes when either A_s or A_p is equal to zero, corresponding to a linearly polarized wave, or when $\delta_p - \delta_s = \pm\pi/2$, corresponding to an elliptically polarized wave.

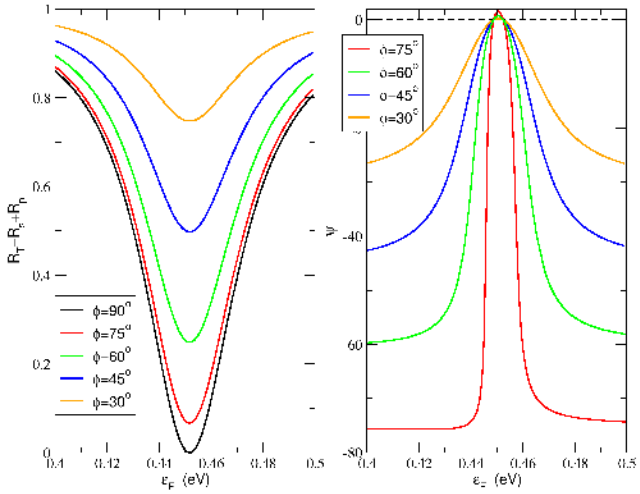

Fig. 17. Total reflectance R_T and the angle of ellipticity ψ as a function of the Fermi energy E_F, for different angles of polarization of the incident wave. The reflectance of the $p-$polarized component vanishes for $E_F = 0.45$ eV. Other parameters as in Fig. 11. The angle of incidence is $\theta = 1.95\theta_c$ and the energy of the incoming light is $\hbar\omega = 5.1$ meV.

In Fig. 17 we represent the total reflectance R_T, given by Eq. (156), and the angle of ellipticity ψ, as given by Eq. (157), as a function of the Fermi energy E_F, for fixed ω and θ and different angles of polarization, φ, of the incident wave. When $\varphi = \pi/2$, the incoming wave is purely $p-$polarized and the reflectance for $E_F = 0.45$ eV is zero (for the given ω and θ). As φ deviates from $\pi/2$, a finite reflectance for $E_F = 0.45$ eV appears due to the $s-$polarized component of the incoming wave, as can be seen in the left panel of Fig. 17. In the right panel of the same figure, the angle of ellipticity (ψ) is plotted. We can see that there are two points for which ψ is zero, they correspond to $A_p = 0$ at $E_F = 0.45$ eV and to $\delta_p - \delta_s = \pm\pi/2$ at a sightly different energy.

6.7. *Otto configuration in a static magnetic field*

We shall now consider the Otto configuration of Fig. 10 in the presence of a static magnetic field $\vec{B}_0 = (0, 0, B_0)$. We take an arbitrarily polarized incident wave,

$$\vec{E}_i(\vec{r}, t) = \left[(E_x^{(i)}, 0, E_z^{(i)}) + (0, E_y^{(i)}, 0) \right] e^{i\vec{k}_i \cdot \vec{r}}, \tag{158}$$

where we have explicitly separated the $p-$ and $s-$polarized components. The starting point to solve the light reflection problem is to write the ER field in regions $m = 1, 2, 3$ in the most general way. We obtain,

i) Region 3:

$$\vec{E}_3 = (E_x^{(i)}, E_y^{(i)}, E_z^{(i)}) e^{i\vec{k}_i \cdot \vec{r}} + (E_x^{(r)}, E_y^{(r)}, E_z^{(r)}) e^{i\vec{k}_r \cdot \vec{r}}, \tag{159}$$

ii) Region 2:

$$\vec{E}_2 = (E_{2,x}^{(+)}, E_{2,y}^{(+)}, E_{2,z}^{(+)}) e^{i\vec{k}_2^{(+)} \cdot \vec{r}} + (E_{2,x}^{(-)}, E_{2,y}^{(-)}, E_{2,z}^{(-)}) e^{i\vec{k}_2^{(-)} \cdot \vec{r}}, \tag{160}$$

iii) Region 1:

$$\vec{E}_1 = (E_{1,x}^{(-)}, E_{1,y}^{(-)}, E_{1,z}^{(-)}) e^{i\vec{k}_1^{(-)} \cdot \vec{r}}, \tag{161}$$

where the wavevectors $\vec{k}_{i,r}$, $\vec{k}_m^{(\pm)}$ have been defined in Sec. 6.4. Similar equations apply to the time-varying part of the magnetic field $\vec{B}$.

The next step is to write the boundary conditions at each interface. At $z = 0$, the magnetic field is continuous, as well as the tangential components of the electric field. The boundary conditions have the same form as Eqs. (99)-(100), and (135)-(136), and shall not be reproduced again. The boundary conditions at the second interface ($z = d$) must take into account the discontinuity of the magnetic field across the graphene layer due to the existence of a surface current $\vec{J}_s$ [see Eq.(7)],

$$\left(\vec{B}_{1t} - \vec{B}_{2t} \right) \Big|_{z=d} = \mu_0 \vec{J}_s \times \hat{n} = \mu_0 \hat{\sigma}(\omega, B_0) \vec{E}_t(z = d) \times \hat{n}\,, \tag{162}$$

with $\vec{B}_{1t}$, $\vec{B}_{2t}$, and $\vec{E}_t$ denoting the tangential (in-plane) components of the electromagnetic field with respect to the graphene sheet. The magneto-optical conductivity tensor of graphene $\hat{\sigma}(\omega, B_0)$ was discussed earlier, in Sec. 3. The boundary conditions relating the electric field amplitudes coincide with those given earlier, namely, Eqs. (101) and (137), whereas for the magnetic field amplitudes we obtain the following set of conditions:

$$\begin{aligned} B_{1,y}^{(-)} - e^{\kappa_1 d} \left(B_{2,y}^{(+)} e^{\kappa_2 d} + B_{2,y}^{(-)} e^{-\kappa_2 d} \right) = \\ -\mu_0 \left(\sigma_{xx} E_{1,x}^{(-)} + \sigma_{xy} E_{1,y}^{(-)} \right), \end{aligned} \tag{163}$$

$$\begin{aligned} B_{1,x}^{(-)} - e^{\kappa_1 d} \left(B_{2,x}^{(+)} e^{\kappa_2 d} + B_{2,x}^{(-)} e^{-\kappa_2 d} \right) = \\ \mu_0 \left(\sigma_{yx} E_{1,x}^{(-)} + \sigma_{yy} E_{1,y}^{(-)} \right). \end{aligned} \tag{164}$$

As before, we express the boundary conditions using the electric field components only. Using Eqs. (85) and (141), we easily obtain:

$$\frac{\omega\epsilon_1}{\kappa_1}E_{1,x}^{(-)} + \frac{\omega\epsilon_2 e^{\kappa_1 d}}{\kappa_2}\left(E_{2,x}^{(+)}e^{\kappa_2 d} - E_{2,x}^{(-)}e^{-\kappa_2 d}\right) = -\frac{i}{\epsilon_0}\left(\sigma_{xx}E_{1,x}^{(-)} + \sigma_{xy}E_{1,y}^{(-)}\right); \tag{165}$$

$$\kappa_1 E_{1,y}^{(-)} + \kappa_2\left(E_{2,y}^{(+)}e^{\kappa_2 d} - E_{2,y}^{(-)}e^{-\kappa_2 d}\right) = i\omega\mu_0\left(\sigma_{yx}E_{1,x}^{(-)} + \sigma_{yy}E_{1,y}^{(-)}\right). \tag{166}$$

Combining Eqs. (99), (101), (103), (135), (137), (143) and (165)-(166), and defining the following vectors,

$$e_p \equiv (E_x^{(r)}/E_x^{(i)}, E_{2,x}^{(+)}/E_x^{(i)}, E_{2,x}^{(-)}/E_x^{(i)}), \tag{167}$$

$$e_s \equiv (E_y^{(r)}/E_x^{(i)}, E_{2,y}^{(+)}/E_x^{(i)}, E_{2,y}^{(-)}/E_x^{(i)}), \tag{168}$$

a closed system of equations for the ER amplitudes is obtained according to

$$\begin{pmatrix} \Xi_p & \Xi_{ps} \\ \Xi_{sp} & \Xi_s \end{pmatrix}\begin{pmatrix} e_p \\ e_s \end{pmatrix} = \begin{pmatrix} \Phi_p \\ f_s\Phi_s \end{pmatrix}, \tag{169}$$

where $f_s \geq 0$ denotes the relative fraction of the incoming electric field stored in the $s-$polarized component, $f_s = E_y^{(i)}/E_x^{(i)}$, and Ξ_p, Φ_p, Ξ_s, Φ_s have been defined in Eqs. (106), (107), (146), and (147), respectively, while other Ξ-matrices are are given by

$$\Xi_{ps} = \begin{pmatrix} 0 & 0 & 0 \\ 0 & 0 & 0 \\ 0 & i\frac{\sigma_{xy}}{\epsilon_0}\kappa_1\kappa_2 & i\frac{\sigma_{xy}}{\epsilon_0}\kappa_1\kappa_2 \end{pmatrix}, \tag{170}$$

$$\Xi_{sp} = \begin{pmatrix} 0 & 0 & 0 \\ 0 & 0 & 0 \\ 0 & -i\omega\mu_0\sigma_{yx} & -i\omega\mu_0\sigma_{yx} \end{pmatrix}. \tag{171}$$

It should be stressed that in Sec. 6.6 the $s-$ and $p-$polarization components were independent, while in the case under consideration (with external magnetic field) they are coupled through the matrices Ξ_{sp} and Ξ_{ps}. The optical properties of the the system in Otto configuration, in the presence of an external magnetic field, are fully determined once the system of equations (169) is solved. For instance, the reflectance is obtained according to

$$R = \frac{|E_x^{(r)}/E_x^{(i)}|^2 + \cos^2\theta|E_y^{(r)}/E_x^{(i)}|^2}{1 + f_s^2\cos^2\theta}, \tag{172}$$

and reduces to the familiar form $R = |E_x^{(r)}/E_x^{(i)}|^2$ in the particular case of a pure $p-$polarized incident wave ($f_s = 0$). Note that, by expressing the incident and

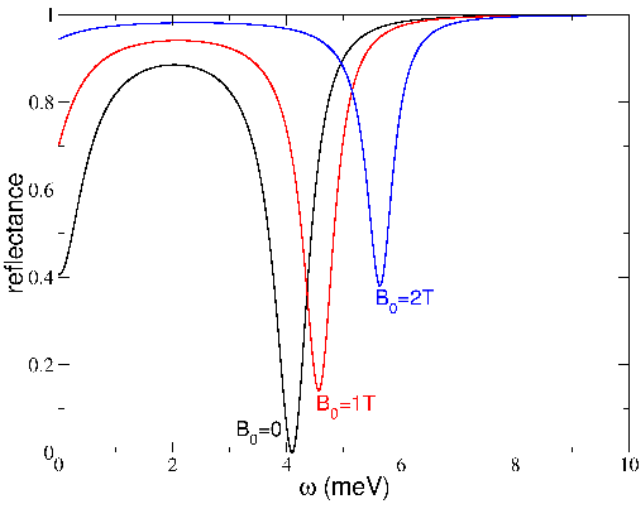

Fig. 18. The reflectance as function of the frequency for $p-$polarized incident light in the presence of a static external magnetic field. Other parameters as in Fig. 11.

reflected electric fields in the form similar to Eqs.(151), and (153),

$$\vec{E}_3 = E_i(\sin\varphi\cos\theta, \cos\varphi, -\sin\varphi\sin\theta)e^{i\vec{k}_i\cdot\vec{r}} + (-E_p\cos\theta, E_s, -E_p\sin\theta)e^{i\vec{k}_r\cdot\vec{r}}\,, \tag{173}$$

the reflectance assumes the simple form $R = (|E_p|^2 + |E_s|^2)/|E_i|^2$, and we have $f_s = \tan^{-1}\varphi\cos^{-1}\theta$.

In Fig. 18 we plot the reflectance as a function of ω for $p-$polarization, obtained by solving numerically (169). We focus on the parameters considered in the absence of magnetic field (refer to Fig. 13). The suppression of the reflectance within specific frequency intervals, interpreted as the excitation of SPPs for the combined layered structure in zero-field (see Sec. 6.3), is still seen to occur. However, for $B_0 > 0$ the dips are less pronounced and shifted relative to the zero-field case. The dips in the reflectance spectrum for non-zero magnetic field are related to a special type of surface plasmonic waves known as magneto-plasmon polaritons, resulting from the hybridization between plasmonic waves and cyclotronic modes. In the semi-classical regime, the energy of a magneto-plasmon polariton mode, in the non-retarded approximation $\omega \ll cq$ [97,98], is given by

$$\Omega(B) \simeq \sqrt{[\Omega(0)]^2 + [\omega_c(B)]^2}\,, \tag{174}$$

where $\Omega(0)$ is the SPP dispersion in the absence of a magnetic field for graphene cladded by two dielectrics of permittivity ϵ_2 and ϵ_1 [see Eq. (64)], and the cyclotron frequency ω_c is given by Eq. (33). A similar formula holds for the 2D electron gas [99,100]. Away from the semi-classical regime (i.e., for low Fermi energy or high magnetic fields), the quantization of the electronic spectrum must be taken into

account. In the quantized regime, the physics of graphene becomes quite exotic, with interband transitions between Landau levels in the valence and conduction bands of graphene controlling the characteristics of the magneto-plasmon polaritons (e.g., their confinement and propagation) and giving rise to quasi-transverse electric modes in specific frequency windows. The reader can refer to Ref. [97] for further details.

The formula (174) can be used to estimate the shift of the resonance positions due to the plasmon hybridization with cyclotronic modes. It predicts a shift $\Omega(B) - \Omega(0)$ of roughly 0.56 meV for $B = 1$ T, and 1.72 meV for $B = 2$ T, which agrees qualitatively with the exact numerical results presented in Fig. 18. We remark that the absolute position of the reflectance dips cannot be obtained from Eq. (174), since this result has been derived for a simpler geometry consisting of graphene sandwiched between two dielectrics (see also discussion in Sec. 6.3). An interesting feature of the hybrid plasmon-cyclotronic modes is the absence of a clear transverse-magnetic character (i.e., contrary to SPPs, magneto-plasmon polaritons have non-zero magnetic field longitudinal components, B_x and B_z [97]). Strictly speaking, these modes cannot be excited by means of pure $p-$polarized light, hence explaining why the reflectance does not drop all the way to zero at the magneto-plasmon polariton frequency (see Fig. 18). For illumination with a TM wave, complete supression of the reflectance can only occur when pure SPP (p-polarized) modes are excited (that is, at zero external magnetic field).

6.8. *Transfer matrix method for N−layer problem*

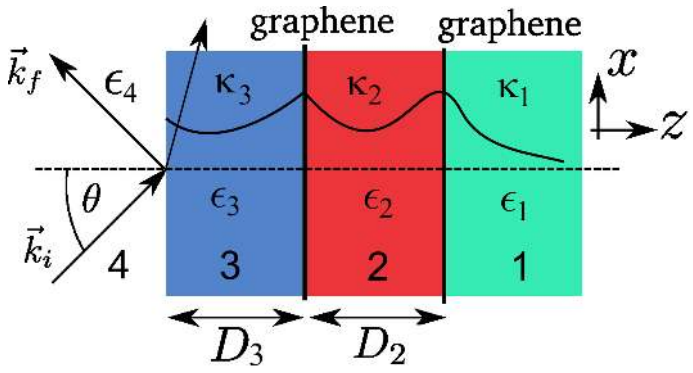

Fig. 19. Configuration for a double graphene-layer system. There are three interfaces: $4-3$, $3-2$, and $2-1$.

We have computed the TM SPP spectrum for graphene double layer in Sec. 4.4. It is instructive to apply the transfer matrix method to a more general problem considering an array of N graphene interfaces. It allows for the calculation of the reflection coefficient in the ATR configuration whose zeros correspond to the SPP

modes (as we will see below, for a propagating wave the *poles* of the reflection coefficient can be related to the SPP modes). Figure 19 depicts the particular case of $N = 2$. Thus, the structure under consideration contains $N + 2$ dielectric layers, first and $N+2$-th layers being semi-infinite with dielectric constants ϵ_1 and ϵ_{N+2}. At the same time, other layers are characterized by width D_m and dielectric constants ϵ_m, $m = 2, ..., N + 1$. N graphene layers are arranged at interfaces between m-th and $m - 1$-th layers ($m = 2, ..., N + 1$). The final solution can be put in the form:

$$\begin{bmatrix} E_x^{(i)} \\ E_x^{(r)} \end{bmatrix} = M \begin{bmatrix} E_{1,x}^{(+)} \\ E_{1,x}^{(-)} \end{bmatrix} , \tag{175}$$

where the total transfer matrix $M = \prod_{m=N+1}^{1} M^{m+1\Rightarrow m}$ and matrices $M^{m+1\Rightarrow m}$ can be obtained as generalization of the matrices in Eqs. (124)-(125), namely

$$M^{N+2\Rightarrow N+1} = \frac{-i}{2\epsilon_{N+2}\kappa_{N+1}} \begin{bmatrix} \epsilon_{N+2} & k_z \\ \epsilon_{N+2} & -k_z \end{bmatrix} \begin{bmatrix} i\kappa_{N+1} & i\kappa_{N+1} \\ -\epsilon_{N+1} & \epsilon_{N+1} \end{bmatrix} , \tag{176}$$

$$M^{m+1\Rightarrow m} = \begin{bmatrix} e^{-\kappa_{m+1}D_{m+1}} & 0 \\ 0 & e^{\kappa_{m+1}D_{m+1}} \end{bmatrix} \frac{1}{2\chi_m} \begin{bmatrix} \chi_m & 1 \\ \chi_m & -1 \end{bmatrix} \times \begin{bmatrix} 1 & 1 \\ \kappa_{m+1}\Lambda_m^{(-)} & -\kappa_{m+1}\Lambda_m^{(+)} \end{bmatrix} . \tag{177}$$

The determinant of the total transfer matrix is given by

$$\det(M) = i\frac{k_z\epsilon_1}{\kappa_1\epsilon_{N+2}} \tag{178}$$

and the reflectance of the structure can be evaluated from the matrix elements [Eq. (127)].

In Fig. 20 we present the reflectance and the absorbance of double-layer graphene ($N = 2$) as functions of both the energy and the incident angle. The most notable effect is the shift of the resonant energy from $\hbar\omega \approx 4$ meV to $\hbar\omega \approx 8.5$ meV (more than 100%!). This is due to the hybridization of the plasmon-polarion bands of the two graphene sheets when they come closer to each other. It is possible to control the position of the resonance by tuning the distance D_2.

7. SPP excitation by incident wave at a metallic contact

7.1. *Green's function for ER scattering problem*

Here we shall consider the problem of scattering of electromagnetic radiation by a very thin metallic stripe (of width L) on top of a graphene sheet (see Fig. 21). It has been solved numerically by Satou and Mikhailov[101], here we shall show how an approximate solution can be obtained analytically using Green's function method[102]. The scattering problem for a plane $p-$polarized wave leads to the two-dimensional Helmholtz equation[95],

$$\nabla_{x,z}^2 B_y + \epsilon(z)\frac{\omega^2}{c^2}B_y = 0 , \tag{179}$$

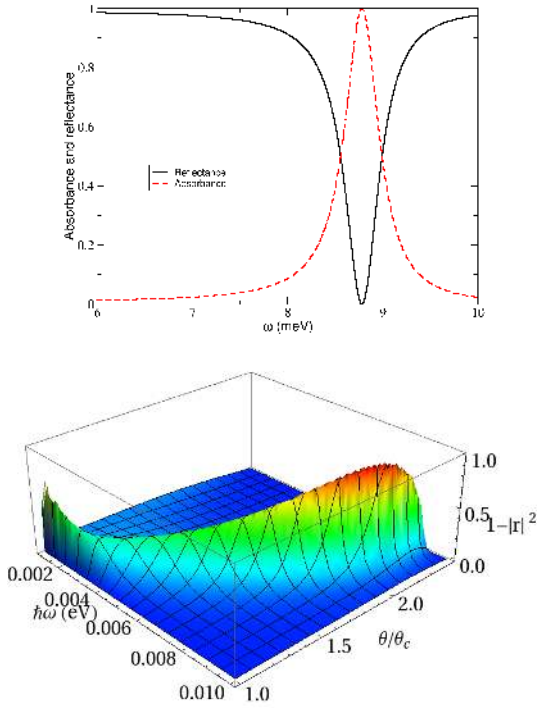

Fig. 20. Top: Absorbance (dashed line) and reflectance (solid line) *versus* photon energy of double-layer graphene for $\theta = 2.1\theta_c$. Bottom: reflectance as function of both the energy $\hbar\omega$ and the angle of incidence, θ/θ_c. The parameters are: $E_F = 0.45$ eV, $\Gamma = 0.1$ meV, ϵ_4=14, $\epsilon_3 = 1$, $\epsilon_2 = \epsilon_1 = 5$, $D_3 = 2.51$ μm, $D_2 = D_3$, and $\theta_c = 36.7^{\rm o}$.

where $\nabla^2_{x,z}$ is the Laplace operator in the xz plane, $\epsilon(z) = \epsilon_2$ for $z < 0$ and $\epsilon(z) = \epsilon_1$ for $z > 0$. Considering an incident wave coming from $z = -\infty$, the solution of Eq. (179) for $z < 0$ can be written as

$$B_y(x, z < 0) = 2B_i \cos(k_z z) e^{iqx} + B_{\rm scat} \, . \tag{180}$$

The first term in Eq. (180) represents total reflection (as if the whole plane $z = 0$ were covered with a perfect metal) and the second one (that we call scattered field) includes the contribution of all parts of the interface that are not covered by the metal (but covered with graphene). As before, here $k_z = k\cos\theta$, $q = k\sin\theta$ and $k = \omega\epsilon_2^{1/2}/c$. The scattered field can be presented in terms of Green's function $G_{\vec{k}}(\vec{r}; \vec{r}')$,

$$B_{\rm scat} = \int_{-\infty}^{\infty} \Big\{ G_{\vec{k}}(\vec{r}; x', z' = 0) \times$$
$$[\Theta(x' - L/2) + \Theta(-x' - L/2)] \left. \frac{\partial B_y}{\partial z'} \right|_{z'=0^-} \Big\} dx' \, , \tag{181}$$

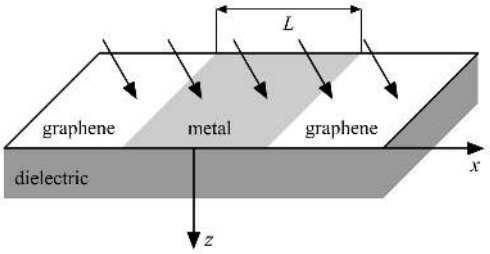

Fig. 21. Graphene sheet on a dielectric substrate with a metal contact (stripe of width L) on top of it.

which is given by [102]

$$G_{\vec{k}}(\vec{r};\vec{r}') = \frac{i}{4}\left[H_0^{(1)}(kR) + H_0^{(1)}(kR')\right] \tag{182}$$

with $R = \sqrt{(x-x')^2+(z-z')^2}$ and $R' = \sqrt{(x-x')^2+(z+z')^2}$. Here $H_0^{(1)}$ denotes the Hankel function of the first kind and zero order. The Green's function (182) is the solution of the equation

$$\nabla_{x,z}^2 G_{\vec{k}}(\vec{r};\vec{r}') + \epsilon_2 \frac{\omega^2}{c^2} G_{\vec{k}}(\vec{r};\vec{r}') = -\delta(\vec{r}-\vec{r}')\,, \tag{183}$$

and takes into account the effects of a field source located at $\vec{r}' = (x', z')$ and of an image source at $\vec{r}' = (x', -z')$. The Heaviside functions $\Theta(x)$ in Eq. (181) explicitly take into account the fact that the sources of the scattered field are located at $|x| \geq L/2$.

Similar to Eq. (180), the field in the substrate ($z > 0$) can be written as

$$B_y(x, z>0) = -\frac{i}{2}\int_{-\infty}^{\infty} \Big\{ H_0^{(1)}([\epsilon_1/\epsilon_2]^{1/2} k\sqrt{(x-x')^2+z^2}) \times \\ [\Theta(x'-L/2) + \Theta(-x'-L/2)]\, \frac{\partial B_y}{\partial z'}\Big|_{z'=0^+} \Big\}\, dx'\,. \tag{184}$$

7.2. *Integral equation*

Matching conditions at $z = 0$, for $|x| \geq L/2$ read:

$$\frac{1}{\epsilon_2}\,\frac{\partial B_y}{\partial z}\Big|_{z=0^-} = \frac{1}{\epsilon_1}\,\frac{\partial B_y}{\partial z}\Big|_{z=0^+} \tag{185}$$

and [see Eq. (50)]

$$B_y(x,0^-) - B_y(x,0^+) = \frac{\sigma(\omega)}{i\varepsilon_0\omega\epsilon_2}\frac{\partial B_y}{\partial z}\Big|_{z=0^-}\,. \tag{186}$$

Substituting Eqs. (180), (181), (184), and (185) into (186), we obtain:

$$2iB_i e^{iqx} - \frac{1}{2\epsilon_2}\int_{|x'|\geq L/2} g(x-x')\left.\frac{\partial B_y(x',z)}{\partial z}\right|_{z=0^-} dx' = \frac{\sigma(\omega)}{\varepsilon_0\omega\epsilon_2}\left.\frac{\partial B_y(x,z)}{\partial z}\right|_{z=0^-} . \quad (187)$$

This is an integral equation for the magnetic field derivative (equal to $i\mu_0\omega E_x$) on graphene, with

$$g(x-x') = \epsilon_2 H_0^{(1)}(k|x-x'|) + \epsilon_1 H_0^{(1)}([\epsilon_1/\epsilon_2]^{1/2}k|x-x'|)\,, \quad (188)$$

Let us introduce an analytic function $f(x)$, such that it is equal to this derivative (divided by $\epsilon_2 B_i$) on uncovered parts of the graphene sheet,

$$f(x) = \left.\frac{1}{\epsilon_2 B_i}\frac{\partial B_y}{\partial z}\right|_{z=0^-} ; \qquad |x'| \geq L/2\,, \quad (189)$$

however, not necessarily vanishing on the metal stripe. It obeys the equation,

$$2ie^{iqx} = \frac{\sigma(\omega)}{\varepsilon_0\omega}f(x) + \frac{1}{2}\int_{|x'|\geq L/2} g(x-x')f(x')dx'\,, \quad (190)$$

that holds for $-\infty < x < \infty$. Multiplying Eq. (190) by $\exp(iQx)$ and integrating we obtain:

$$i4\pi\delta(q+Q) = \frac{\sigma(\omega)}{\varepsilon_0\omega}\tilde{f}(Q) - i\mathcal{K}(Q)\int_{|x'|\geq L/2} e^{iQx'}f(x')dx'\,, \quad (191)$$

where

$$\tilde{f}(Q) = \int_{-\infty}^{\infty} e^{iQx}f(x)dx$$

is a Fourier transform of function $f(x)$, and

$$\mathcal{K}(Q) = \frac{i}{2}\int_{-\infty}^{\infty} e^{iQ(x-x')}g(x-x')d(x-x') = \frac{\epsilon_2}{\kappa_2(Q)} + \frac{\epsilon_1}{\kappa_1(Q)}\,,$$

$\kappa_1(Q)$, $\kappa_2(Q)$ were defined in Eq.(44) with replacing $q \Rightarrow Q$. The integral in the last term of Eq. (191) can be written as

$$\frac{1}{2\pi}\int_{|x'|\geq L/2} e^{iQx'}\int_{-\infty}^{\infty}\tilde{f}(Q')e^{-iQ'x'}dQ'dx' = \tilde{f}(Q) - \frac{1}{\pi}\int_{-\infty}^{\infty}\tilde{f}(Q')\frac{\sin\left[(Q-Q')L/2\right]}{Q-Q'}dQ'\,.$$

Therefore, Eq. (191) reads as

$$-4\pi\delta(q+Q) = i\frac{\sigma(\omega)}{\varepsilon_0\omega}\tilde{f}(Q) + \mathcal{K}(Q)\int_{-\infty}^{\infty}\mathcal{L}(Q-Q')\tilde{f}(Q')dQ'\,. \quad (192)$$

This is a Fredholm integral equation of the second kind [102] with the kernel

$$\mathcal{L}(Q-Q') = \delta(Q-Q') - \frac{\sin\left[(Q-Q')L/2\right]}{\pi(Q-Q')}\,. \quad (193)$$

First, let us consider the trivial case of $L = 0$ (no metallic stripe). Then $\mathcal{L}(Q - Q') = \delta(Q - Q')$ and we have:

$$\tilde{f}_0(Q) = -\frac{4\pi\delta(q+Q)}{\mathcal{K}(Q) + i\frac{\sigma(\omega)}{\varepsilon_0\omega}}$$

and

$$f_0(x) = -\frac{2\exp(iqx)}{\mathcal{K}(q) + i\frac{\sigma(\omega)}{\varepsilon_0\omega}}\,. \tag{194}$$

Substituting (194) into Eqs. (181) and (184), we obtain:

$$\begin{aligned} B_y(x, z<0) &= B_0 e^{iqx}\left(e^{ik_z z} + r_y e^{-ik_z z}\right)\,; \\ B_y(x, z>0) &= t_y B_i e^{i(qx-\kappa_1(q)z)}\,. \end{aligned} \tag{195}$$

with

$$\begin{aligned} r_y &= \frac{\mathcal{K}(q) + i\frac{\sigma(\omega)}{\epsilon_0\omega} - \frac{2\epsilon_2}{\kappa_2(q)}}{\mathcal{K}(q) + i\frac{\sigma(\omega)}{\epsilon_0\omega}}\,; \\ t_y &= \frac{\epsilon_1}{\kappa_1(q)}\frac{2}{\mathcal{K}(q) + i\frac{\sigma(\omega)}{\varepsilon_0\omega}}\,, \end{aligned} \tag{196}$$

Here we have taken into account, that $\kappa_2(q) = -ik_z$. We have used the following relation for the Fourier transform of the Hankel function:

$$\int_{-\infty}^{\infty} dx H_0^{(1)}(k\sqrt{x^2+z^2})\exp(-iQx) = \frac{2\exp(i\sqrt{k^2-Q^2}x)}{\sqrt{k^2-Q^2}}. \tag{197}$$

Of course, there is no real scattering in this case, just reflection, and the coefficients r_y and t_y could be found in a much simpler way but this simple example demonstrates how the method works. Let us notice that, if we formally suppose that $\kappa_{1,2}(q)$ are real (respectively, k_z is imaginary), the poles of the reflection and transmission coefficients (194) yield the dispersion relation of surface plasmon-polaritons in graphene. Indeed, it is easy to check that the equation

$$\mathcal{K}(q) + i\frac{\sigma(\omega)}{\varepsilon_0\omega} = 0 \tag{198}$$

is equivalent to Eq. (47).

7.3. *Solution for qL << 1*

We shall now solve Eq. (192) for the case when L is small, $QL << 1$, where Q is any relevant wavenumber along x. Then we put $\sin[(Q-Q')L/2] \approx (Q-Q')L/2$ and

$$\mathcal{L}(Q - Q') = \delta(Q - Q') - \frac{L}{2\pi}\,. \tag{199}$$

By noting that

$$\int_{-\infty}^{\infty} \tilde{f}(Q)dq = 2\pi f(0) = const\,,$$

Eq. (192) is solved to give

$$\tilde{f}(Q) = \tilde{f}_0(Q) + f(0)\frac{\mathcal{K}(Q)L}{\mathcal{K}(Q) + i\frac{\sigma(\omega)}{\varepsilon_0\omega}}$$

and

$$f(x) = f_0(x) + f(0)\frac{L}{2\pi}\int_{-\infty}^{\infty} \frac{\mathcal{K}(Q)}{\mathcal{K}(Q) + i\frac{\sigma(\omega)}{\varepsilon_0\omega}} e^{-iQx} dQ\,, \tag{200}$$

where $f_0(x)$ is given by Eq. (194). The integral in Eq. (200) converges, since $\mathcal{K}(Q) \sim Q^{-1}$ for large Q, and can be calculated using Jordan's lemma and the contour shown in Fig. 22 (for $x > 0$). We denote by Q_p^- the pole that lies in the lower half-plane and

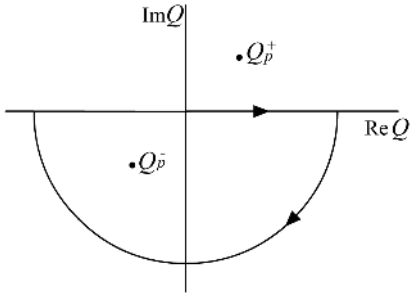

Fig. 22. Contour for integral in Eq. 200 for $x > 0$. For $x < 0$ it has to be closed in the upper half-plane.

note that it is one of the two roots of Eq. (198). In other words, Q_p^- and $Q_p^+ = -Q_p^-$ are two possible values of the SPP wavevector for a given frequency ω. Calculation of the integral yields

$$\frac{1}{2\pi}\int_{-\infty}^{\infty} \frac{\mathcal{K}(Q)}{\mathcal{K}(Q) + i\frac{\sigma(\omega)}{\varepsilon_0\omega}} e^{-iQx} dQ = i\frac{\mathcal{K}(Q_p^-)}{\frac{\partial\mathcal{K}(Q)}{\partial Q}\Big|_{Q=Q_p^-}} e^{-iQ_p^- x} = -\frac{\sigma(\omega)}{\varepsilon_0\omega}\frac{\kappa_1^3(Q_p)\kappa_2^3(Q_p)}{Q_p^-\left[\epsilon_2\kappa_1^3(Q_p) + \epsilon_1\kappa_2^3(Q_p)\right]} e^{-iQ_p^- x}\,,$$

and we obtain:

$$f(x) = f_0(x) + f(0)L\mathcal{Q}e^{iQ_p^+ x}\,; \tag{201}$$

$$\mathcal{Q} = \frac{\sigma(\omega)}{\varepsilon_0\omega}\frac{\kappa_1^3(Q_p)\kappa_2^3(Q_p)}{Q_p^+\left[\epsilon_2\kappa_1^3(Q_p) + \epsilon_1\kappa_2^3(Q_p)\right]}\,. \tag{202}$$

By requiring self-consistency of Eq. (202), we obtain

$$f(0) = -\frac{1}{1 - iL\mathcal{Q}} \frac{2}{\mathcal{K}(q) + \frac{\sigma(\omega)}{\varepsilon_0 \omega}}$$

and the final result is:

$$f(x) = -\frac{2}{\mathcal{K}(q) + i\frac{\sigma(\omega)}{\varepsilon_0 \omega}} \left[\exp(iqx) + \frac{L\mathcal{Q}}{1 - L\mathcal{Q}} e^{iQ_p^+ x} \right] . \tag{203}$$

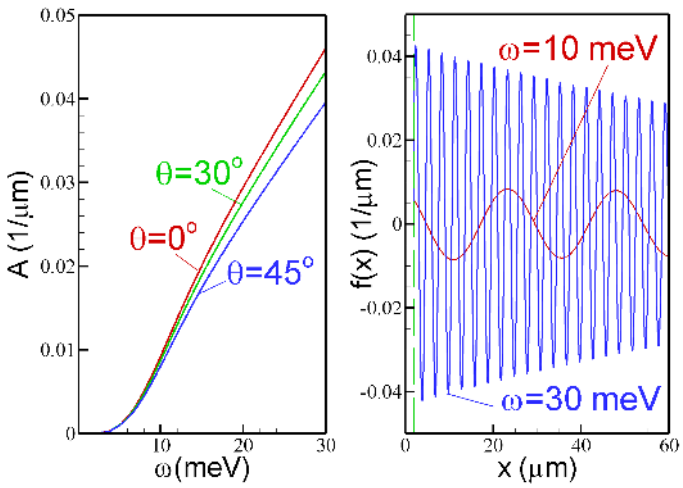

Fig. 23. SPP excitation by incident ER at metallic stripe. Left: Amplitude A of the second term of the function $f(x)$ [Eq. (203)] *versus* frequency ω for different angles of incidence as indicated. Right: Spatial profile of the generated SPP wave for two different frequencies indicated on the plot. The parameters are: $E_F = 0.45$ eV, $\hbar\Gamma = 0.1$ meV, $\epsilon_2 = 1$, $\epsilon_1 = 5$, and $L = 4$ μm.

Equation (203) is valid for $x > 0$, while for $x < 0$ we have $Q_p^+ \to Q_p^-$. The second term of this equation represents the SPP wave excited by shining ER radiation at the metallic contact. The two waves described by Eq. (203) can be referred to as forced and intrinsic oscillations, respectively, of the free 2D electron gas in graphene. The metallic stripe is a topological defect imposed on graphene and, as mentioned in the Introduction, can be used to launch SPP waves in this two-dimensional conductor. The amplitude of the SPP oscillations is proportional to the width of the contact ("defect power") and depends on the ER frequency as shown in Fig. Fig. 23. Let us remind that the solution (203) is valid in the limit $|Q_p|L << 1$. As shown numerically by Satou and Mikhailov [101], for larger $|Q_p|L$ the SPP amplitude becomes to oscillate as a function of frequency or contact width. The generated polaritons decay with the distance from the contact-stripe antenna because Q_p is complex (see Fig. 23). The scattered electromagnetic fields above and below the interface can be found by substituting (203) into Eqs. (181) and (184), leading to a

rather complex dependence on x and z (or, in other words, on the scattering angle and distance from the contact).

8. ER coupling to graphene with periodically modulated conductivity

8.1. *Polaritonic crystal*

So far, we have been considering graphene as a perfectly flat membrane with a homogeneous optical conductivity. Now we shall relax the latter assumption still keeping the former (i.e. graphene's flatness). There are different ways of implementing a position dependent conductivity in graphene: (i) patterning graphene micro-ribbons in an otherwise homogeneous graphene sheet, (ii) inducing an inhomogeneous strain profile in graphene, (iii) producing an inhomogeneous profile of adsorbed atoms or molecules on graphene sheet, and (iv) using patterned gates. The last three mechanisms produce a position dependent electronic density leading to a position dependent conductivity of graphene because of the dependence of the Fermi energy on the density.

We assume a periodically modulated conductivity, $\sigma(x + D) = \sigma(x)$, and introduce the one-dimensional (1D) reciprocal lattice wave vector, $G = 2\pi/D$. The system we have in mind is represented in Fig. 24. It can be seen as an 1D polaritonic crystal [78,80].

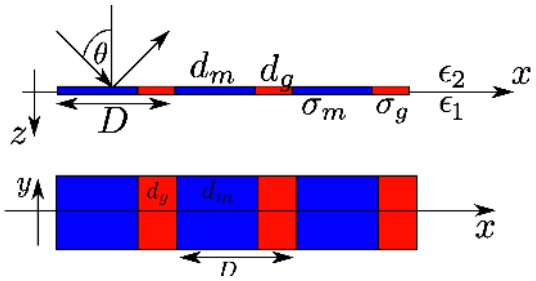

Fig. 24. System with a periodically modulated conductivity period D (side and top views).

Since the system is periodic, the fields can be written in the form of Fourier–Floquet series (in other words, they obey the Bloch theorem). In Fig. 24 we have represented an array of graphene micro-ribbons, of conductivity σ_g, separated by regions of conductivity σ_m, which can be made of either of a dielectric or a metal. However, we note that the formalism we develop below applies to any profile of modulated conductivity. Thus, Fig. 24 should be understood as a schematic representation of one of the aforementioned possibilities.

8.2. *Formalism and results*

First, we want to find the band structure of the TM-type surface plasmon–polaritons for a system of Fig. 24. If it is composed of periodic patches of graphene, the approach presented below fails because it requires an infinite number of reciprocal lattice vectors for achieving convergence. (The scattering problem we study later is, however, well defined.)

As before, we assume that the system supports surface waves propagating along the graphene sheet and decaying away from it. We consider p-polarized waves written in the form of Fourier–Floquet series,

$$B_{m,y}(x,z) = \sum_n \mathcal{B}_{m,y||n} e^{i(q+nG)x} e^{-\kappa_{m||n}|z|}\,; \tag{204}$$

$$E_{m,x}(x,z) = \sum_n \mathcal{E}_{m,x||n} e^{i(q+nG)x} e^{-\kappa_{m||n}|z|}\,; \tag{205}$$

$$E_{m,z}(x,z) = \sum_n \mathcal{E}_{m,z||n} e^{i(q+nG)x} e^{-\kappa_{m||n}|z|}\,, \tag{206}$$

where the index m labels the media above ($m = 1$) and below ($m = 2$) the $z = 0$ plane, and the sum runs over all integers. Since the system is linear, each Fourier component is independent of the others. Then, it follows from Maxwell's equations that

$$\kappa_{m||n} = \sqrt{(q+nG)^2 - \omega^2\epsilon_m/c^2}\,, \tag{207}$$

$$\mathcal{B}_{m,y||n} = (-1)^m \frac{i\omega\epsilon_m}{c^2\kappa_{m||n}} \mathcal{E}_{m,x||n}\,, \tag{208}$$

$$\mathcal{E}_{m,z||n} = (-1)^{m+1} i \frac{q+nG}{\kappa_{m||n}} \mathcal{E}_{m,x||n}\,. \tag{209}$$

Since the conductivity is periodic, it can be expanded in Fourier series as

$$\sigma(x) = \sum_l e^{ilGx} \widetilde{\sigma}_l\,, \tag{210}$$

where

$$\widetilde{\sigma}_l = \frac{1}{D}\int_0^D \sigma(x) e^{-ilGx} dx\,. \tag{211}$$

The boundary conditions $E_{1,x}(x,0) - E_{2,x}(x,0) = 0$, $B_{1,y}(x,0) - B_{2,y}(x,0) = -\mu_0\sigma(x)E_{1,x}(x,0)$ read:

$$\sum_n (\mathcal{E}_{1,x||n} - \mathcal{E}_{2,x||n}) e^{inGx} = 0\,; \tag{212}$$

$$\sum_n (\mathcal{B}_{1,y||n} - \mathcal{B}_{2,y||n}) e^{inGx} = -\mu_0 \sum_{l,p} \widetilde{\sigma}_l \mathcal{E}_{1,x||p} e^{i(l+p)Gx}\,, \tag{213}$$

or, alternatively ($l + p = n \Leftrightarrow l = n - p$),

$$\sum_n (\mathcal{B}_{1,y||n} - \mathcal{B}_{2,y||n}) e^{inGx} = -\mu_0 \sum_{n,p} \widetilde{\sigma}_{n-p} \mathcal{E}_{1,x||p} e^{inGx}\,. \tag{214}$$

As a result, Eqs. (212)-(213) imply that

$$\mathcal{E}_{1,x||n} - \mathcal{E}_{2,x||n} = 0 \tag{215}$$

$$\mathcal{B}_{1,y||n} - \mathcal{B}_{2,y||n} + \mu_0 \sum_p \widetilde{\sigma}_{n-p} \mathcal{E}_{1,x||p} = 0\,. \tag{216}$$

After some algebra, we obtain a non-linear eigenvalue problem,

$$\frac{\epsilon_1}{\kappa_{1||n}} \mathcal{E}_{1,x||n} + \frac{\epsilon_2}{\kappa_{2||n}} \mathcal{E}_{1,x||n} + \frac{i}{\omega\epsilon_0} \sum_p \widetilde{\sigma}_{n-p} \mathcal{E}_{1,x||p} = 0\,, \tag{217}$$

for the frequency ω. If we consider only the Fourier component $p = n$ in the sum in Eq.(217), we obtain

$$\frac{\epsilon_1}{\kappa_{1||n}} + \frac{\epsilon_2}{\kappa_{2||n}} + \frac{i}{\omega\epsilon_0} \widetilde{\sigma}_0 = 0\,, \tag{218}$$

which is just the equation for the SPP frequency of the wavevector $q+nG$ [compare with Eq. (47)]. The quantity $\widetilde{\sigma}_0$ is the average of the conductivity in the primitive cell,

$$\widetilde{\sigma}_0 = \frac{1}{D} \int_0^D \sigma(x) dx\,. \tag{219}$$

The presence of harmonics with other Fourier components of $\sigma(x)$, $\widetilde{\sigma}_l$ with $l \neq 0$ in Eq. (217) gives rise to the band-gap structure of the polaritonic spectrum, equivalent to the so called empty lattice approximation of electrons in a periodic potential [91]. It can be presented either in the extended scheme if we consider the SPP wavevector varying from $-\infty$ to ∞, or in the reduced scheme if we limit the wavevector to the first Brillouin zone, $-\frac{\pi}{D} \leq q < \frac{\pi}{D}$. In the latter case, folding the dispersion curve into the first Brillouin zone produces upper branches, i.e. the polaritonic crystal structure for the SPP frequencies.

We note that the non-linear eigenvalue problem can be transformed into a linear one if we make the non-retarded approximation. As discussed in Sec. 4, we do not expect to obtain an accurate solution for the band at wave vectors close to zero. In the non-retarded approximation we have $\kappa_{m||n} \approx |q + nG|$. Using Eq. (51) and writing the spatial-dependent conductivity as

$$\sigma(x) = i\frac{\nu}{\omega} s(x)\,, \tag{220}$$

the Fourier transform of $\sigma(x)$ can be written as

$$\widetilde{\sigma}_l = i\frac{\nu}{\omega} \mathcal{S}_l\,, \tag{221}$$

where $\mathcal{S}_l$ is the l-th Fourier component of $s(x)$. This allows to write Eq. (217) as

$$\frac{\epsilon_1 + \epsilon_2}{|q + nG|} \mathcal{E}_{1,x||n} - \frac{\nu}{\omega^2\epsilon_0} \sum_p \mathcal{S}_{n-p} \mathcal{E}_{1,x||p} = 0\,, \tag{222}$$

or as

$$\frac{\nu|q+nG|}{2\bar{\epsilon}\epsilon_0}\sum_p \mathcal{S}_{n-p}\mathcal{E}_{1,x||p} = \omega^2\mathcal{E}_{1,x||n}\,, \tag{223}$$

which has the standard form of a linear eigenvalue problem. However, the band structure derived from such procedure is not quantitatively accurate.

For obtaining the spectrum in the vicinity of $q = G/2 = \pi/D$, we need to take into account field harmonics $\mathcal{E}_{1,x||n}$ with $n = -1, 0$ only (which correspond to the lowest gap in the spectrum). In this case, Eq. (223) reduces to two equations only:

$$\frac{\nu G}{4\bar{\epsilon}\epsilon_0}\left(\mathcal{S}_0\mathcal{E}_{1,x||-1} + \mathcal{S}_{-1}\mathcal{E}_{1,x||0}\right) = \omega^2\mathcal{E}_{1,x||-1}\,, \tag{224}$$

$$\frac{\nu G}{4\bar{\epsilon}\epsilon_0}\left(\mathcal{S}_1\mathcal{E}_{1,x||-1} + \mathcal{S}_0\mathcal{E}_{1,x||0}\right) = \omega^2\mathcal{E}_{1,x||0}\,, \tag{225}$$

which form a 2×2 eigenvalue problem. The eigenvalues are

$$\omega^2 = \frac{\nu G}{4\bar{\epsilon}\epsilon_0}\left(\mathcal{S}_0 \pm \sqrt{\mathcal{S}_1\mathcal{S}_{-1}}\right) = \frac{\alpha E_F c G}{\bar{\epsilon}\hbar}\left(\mathcal{S}_0 \pm \sqrt{\mathcal{S}_1\mathcal{S}_{-1}}\right)\,. \tag{226}$$

Equation (226) describes the form of the spectrum in the vicinity of the gap at the Brillouin zone edge. As expected, the value of the gap depends on the Fourier components $\widetilde{\sigma}_{\pm 1}$ of the conductivity. The approximated description of the spectrum that we have presented has to be checked against a full numerical calculation. We have verified that for the case of an array of micro-ribbons this simplified description fails because a large number of reciprocal lattice vectors are necessary to describe the spectrum accurately. In fact, this particular case is poorly convergent. This is a consequence of the non-continuous nature of graphene in the micro-ribbon structure.

For further progress we need a model for $\sigma(x)$. We assume a conductivity profile of the form

$$\sigma(x) = \sigma_D s(x) = \sigma_D[1 - h\cos(2\pi x/D)]\,, \tag{227}$$

where σ_D is given by Eq. (23). The Fourier transform of $s(x)$ reads:

$$\mathcal{S}_0 = 1\,, \tag{228}$$

$$\mathcal{S}_l = -\frac{h}{2}(\delta_{l,1} + \delta_{l,-1})\,. \tag{229}$$

For this form of $s(x)$ the eigenvalue problem (223) has a fast convergence.

In the top plot of Fig. 25 we present the band structure of the polaritonic crystal produced by the conductivity modulation, computed using the non-retarded approximation. The dashed black lines represent the folding of the bare SPP dispersion curve of homogeneous graphene into the first Brillouin zone. The solid lines represent the spectrum when the conductivity is modulated. Clearly, there is a large gap between the first and the second bands and smaller gaps between the other upper bands. The blue dashed straight lines represent the light cone, $\hbar ck/\sqrt{\epsilon_1}$. The states of the upper bands located within the cone can be excited by shining light on the flat graphene sheet without the aid of a prism.

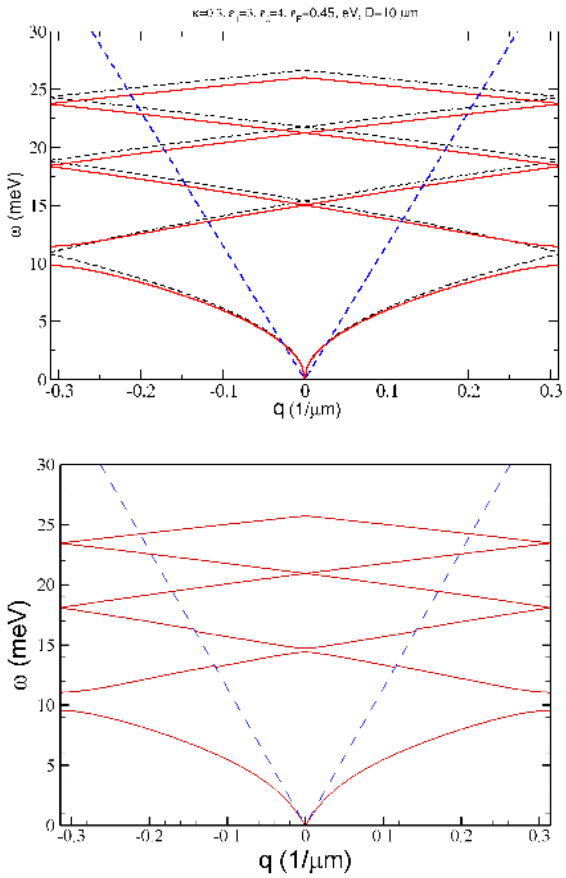

Fig. 25. Band structure of the polaritonic crystal obtained from the solution of the linear eigenvalue problem (223), i.e. in the non-retarded approximation (upper panel) and by directly solving Eq. (217) (lower panel). Only the first six bands are shown. The dashed curves in the upper panel correspond to the "empty lattice" approximation. Notice the anti-crossing of the bands $n = \pm 1$ in the vicinity of $q = 0$ (near 15 mev). The parameters are $E_F = 0.45$ eV, $D = 10$ μm, $\epsilon_1 = 3$, $\epsilon_2 = 4$, and $h = 0.3$.

As it can be observed in Fig. 25, the band structure for it is inaccurate at $k \approx 0$, the dispersion curve for the lowest band lies inside the light cone and the curves representing the upper branches do not show the expected anti-crossing. These are artefacts produced by the non-retarded approximation used. The band structure calculated taking into account the retardation effect [80] is free from these artefacts (see the lower plot of Fig. 25).

8.3. *Scattering by a polaritonic crystal*

8.3.1. *Formalism*

Having studied the emergence of the polaritonic band structure in a system with periodically modulated conductivity, we now want to discuss the scattering of light from a structure of the type represented in Fig. 24. We consider TM-polarized waves in the form

$$B_{m,y}(x,z) = \delta_{m,2} B_y^{(i)} e^{iqx} e^{ik_z z} + \sum_n \mathcal{B}_{m,y||n} e^{i(q+nG)x} e^{-\kappa_{m||n}|z|}\,, \tag{230}$$

$$E_{m,x}(x,z) = \delta_{m,2} E_x^{(i)} e^{iqx} e^{ik_z z} + \sum_n \mathcal{E}_{m,x||n} e^{i(q+nG)x} e^{-\kappa_{m||n}|z|}\,, \tag{231}$$

$$E_{m,z}(x,z) = \delta_{m,2} E_z^{(i)} e^{iqx} e^{ik_z z} + \sum_n \mathcal{E}_{m,z||n} e^{i(q+nG)x} e^{-\kappa_{m||n}|z|}\,. \tag{232}$$

where $q = k\sin\theta$, $k_z = k\cos\theta$, $k = \sqrt{\epsilon_2}(\omega/c)$. The relations between the amplitudes of the reflected and transmitted fields, $\mathcal{B}_{m,y||n}$, $\mathcal{E}_{m,x||n}$, and $\mathcal{E}_{m,z||n}$ are described by Eqs.(208) and (209), while those between the amplitudes of the incoming field are the same as Eqs. (83) and (84), with ϵ_3 being replaced by ϵ_2.

Notice that in Eqs. (230), (231) and (232) the ratio $(q+nG)/k$ can be interpreted as the sinus of the scattering angle of the Fourier mode n, that is,

$$e^{i(q+nG)x} = e^{ik\sin\theta_{2||n}x}\,, \tag{233}$$

leading to

$$\theta_{2||n} = \arcsin[(q+nG)/k]\,. \tag{234}$$

As a result, the usual condition for the Bragg scattering reads as

$$k\sin\theta_{2||n} = k\sin\theta + n2\pi/D < k\,;$$
$$D(\sin\theta_{2||n} - \sin\theta) = n\lambda\,, \tag{235}$$

where $\lambda = 2\pi/k$ is the wavelength of light in the top dielectric with ϵ_2. In fact, $(q+nG)^2 - [\kappa_{2||n}]^2 = k^2$ for both propagating and evanescent waves, but for diffraction orders (n) corresponding to propagating waves

$$\kappa_{2||n} = -ik\cos\theta_{2||n}. \tag{236}$$

In a similar manner it is possible to introduce the scattering angles for transmitted waves, $\theta_{1||n}$

$$q + nG = (\omega/c)\epsilon_1^{1/2}\sin\theta_{1||n}\,, \tag{237}$$

$$\kappa_{1||n} = -i(\omega/c)\epsilon_1^{1/2}\cos\theta_{1||n}. \tag{238}$$

The boundary conditions imply:

$$\mathcal{E}_{1,x||0} = \mathcal{E}_{2,x||0} + E_x^{(i)}\,, \tag{239}$$

$$\mathcal{E}_{1,x||n} = \mathcal{E}_{2,x||n} \quad \wedge \quad n \neq 0\,, \tag{240}$$

and

$$\mathcal{B}_{1,y||0} - \mathcal{B}_{2,y||0} - B_y^{(i)} = -\mu_0 \sum_p \widetilde{\sigma}_{-p} \mathcal{E}_{1,x||p}\,, \tag{241}$$

$$\mathcal{B}_{1,y||n} - \mathcal{B}_{2,y||n} = -\mu_0 \sum_p \widetilde{\sigma}_{n-p} \mathcal{E}_{1,x||p} \quad \wedge \quad n \neq 0\,. \tag{242}$$

Using the relations between the fields, Eqs. (83) and (208), the set of boundary conditions reduces to

$$\left(\frac{\epsilon_1}{\kappa_{1||0}} + \frac{\epsilon_2}{\kappa_{2||0}}\right) \mathcal{E}_{1,x||0} + \frac{i}{\omega\epsilon_0} \sum_p \widetilde{\sigma}_{-p} \mathcal{E}_{1,x||p} = \frac{2i\epsilon_2}{k_z} E_x^{(i)}\,, \tag{243}$$

$$\left(\frac{\epsilon_1}{\kappa_{1||n}} + \frac{\epsilon_2}{\kappa_{2||n}}\right) \mathcal{E}_{1,x||n} + \frac{i}{\omega\epsilon_0} \sum_p \widetilde{\sigma}_{n-p} \mathcal{E}_{1,x||p} = 0 \quad \wedge \quad n \neq 0\,. \tag{244}$$

We recall that

$$\kappa_{m||n} = \sqrt{(k\sin\theta + nG)^2 - \omega^2\epsilon_m/c^2} \tag{245}$$

for non-negative arguments of the square root, otherwise $\kappa_{m||n}$ is written as

$$\kappa_{m||n} = -i\sqrt{\omega^2\epsilon_m/c^2 - (k\sin\theta + nG)^2}\,. \tag{246}$$

The last equation imposes $\kappa_{1||0} = -ik_z$. The choice for the sign of the square root is dictated by physical reasons: we must have reflected waves for $z < 0$ and transmitted waves for $z > 0$ (so called Rayleigh conditions).

8.3.2. *Reflectance and transmittance efficiencies*

Let us compute the fraction of the ER energy carried by the different diffracted orders. The time average of the Poynting vector, $\langle\vec{S}\rangle = \Re(\vec{E} \times \vec{H}^*)/2$, is given by (recall Sec. 2.3)

$$\langle\vec{S}\rangle = \frac{1}{2\mu_0}\Re(-\hat{x}E_z B_y^* + \hat{y}E_x B_y^*)\,. \tag{247}$$

Thus, for diffraction order n we have

$$S_z^{(i)} = \frac{\omega\epsilon_2}{2\mu_0 c^2 k_z}\left|E_x^{(i)}\right|^2\,, \tag{248}$$

$$S_{2,z||n} = -\frac{\omega\epsilon_2}{2\mu_0 c^2|\kappa_{2||n}|}\left|E_{2,x||n}\right|^2\,, \tag{249}$$

$$S_{1,z||n} = \frac{\omega\epsilon_1}{2\mu_0 c^2|\kappa_{1||n}|}\left|E_{1,x||n}\right|^2 \tag{250}$$

for the incident, reflected, and transmitted power per unit area (along the $\hat{z}$ direction), respectively. Here we have assumed that $\kappa_{m||n}$ is pure imaginary; if it is real, then the corresponding order n carries no energy due to evanescent character of the corresponding wave. The negative sign of the reflected power corresponds to the

wave propagation in the negative direction along the axis $\hat{z}$. Finally, the reflectance and transmittance efficiencies are

$$\mathcal{R}_n = -\frac{S_{2,z||n}}{S_z^{(i)}} = \frac{k_z}{|\kappa_{2||n}|} \left| r_{x||n} \right|^2 , \tag{251}$$

$$\mathcal{T}_n = \frac{S_{1,z||n}}{S_z^{(i)}} = \frac{\epsilon_1 k_z}{\epsilon_2 |\kappa_{1||n}|} \left| t_{x||n} \right|^2 , \tag{252}$$

respectively. The diffuse reflectance and diffuse transmittance amplitudes of the order n entering these relations are defined as

$$r_{x||n} = \frac{\mathcal{E}_{2,x||n}}{E_x^{(i)}} , \tag{253}$$

$$t_{x||n} = \frac{\mathcal{E}_{1,x||n}}{E_x^{(i)}} . \tag{254}$$

The specular reflectance and transmittance ($n = 0$ mode) are given by

$$\mathcal{R}_0 = \left| r_{x||0} \right|^2 , \tag{255}$$

and

$$\mathcal{T}_0 = \left| t_{x||0} \right|^2 \frac{\epsilon_1}{\epsilon_2} \frac{\cos\theta}{\sqrt{\epsilon_1/\epsilon_2 - \sin^2\theta}} . \tag{256}$$

The last expression is valid for $\epsilon_1 > \epsilon_2$ or for $\theta < \theta_c = \arcsin(\sqrt{\epsilon_1/\epsilon_2})$, with θ_c denoting the critical angle for total reflection at the interface.

In general, for $n \neq 0$, using the scattering angles for diffuse reflection and transmision modes, Eqs. (236), (238), the diffuse reflectance efficiency is

$$\mathcal{R}_n = \frac{\cos\theta}{\cos\theta_{2||n}} \left| r_{x||n} \right|^2 , \tag{257}$$

and the diffuse transmittance efficiency is given by

$$\mathcal{T}_n = \sqrt{\frac{\epsilon_1}{\epsilon_2}} \frac{\cos\theta}{\cos\theta_{1||n}} \left| t_{x||n} \right|^2 . \tag{258}$$

It should be noticed that Eqs. (257) and (258) are valid for positive arguments of the square root only (i.e. for propagating waves) and for real dielectric permitivitties ϵ_1 and ϵ_2. The absorbance is defined as $\mathcal{A} = 1 - \sum_n (\mathcal{R}_n + \mathcal{T}_n)$, where the sum over n is restricted to the diffraction orders corresponding to propagating waves only.

8.3.3. *Two special cases*

Let us consider a special case of vanishing conductivity ("graphene is absent"). Then Eqs. (243) and (244) give $\mathcal{E}_{1,x||n} = 0$ ($n \neq 0$) (no diffuse reflectance and transmittance in this case) and

$$\frac{\mathcal{E}_{1,x||0}}{E_x^{(i)}} = 2 \left(1 + \sqrt{\frac{\epsilon_1}{\epsilon_2}} \frac{\cos\theta}{\sqrt{1 - \epsilon_2 \sin^2\theta/\epsilon_1}} \right)^{-1} . \tag{259}$$

The reflection coefficient is given by

$$r_{x||0} = \frac{\mathcal{E}_{1,x||0}}{E_x^{(i)}} - 1 = \frac{\sqrt{1-\epsilon_2 \sin^2\theta/\epsilon_1} - \sqrt{\epsilon_1/\epsilon_2}\cos\theta}{\sqrt{1-\epsilon_2 \sin^2\theta/\epsilon_1} + \sqrt{\epsilon_1/\epsilon_2}\cos\theta}\,, \tag{260}$$

which reproduces the well known result from elementary optics.

Another particular case is obtained when $d_g = D$. In this case, only the $m = 0$ Fourier component of $\sigma(x)$ survives. Thus, we obtain:

$$\frac{\mathcal{E}_{1,x||0}}{E_x^{(i)}}\left(\frac{1}{\cos\theta} + \frac{\epsilon_1/\epsilon_2}{\sqrt{\epsilon_1/\epsilon_2 - \sin^2\theta}} + \frac{\sigma_D}{\sqrt{\epsilon_2}\epsilon_0 c}\right) = \frac{2}{\cos\theta}\,. \tag{261}$$

Again, using Eq. (256) and putting $\epsilon_1 = \epsilon_2 = 1$ we obtain the well known result for the transmittance of free-standing graphene (for a TM wave),

$$\mathcal{T}_0 = \left|\frac{2}{2 + \sigma_D \cos\theta/\epsilon_0 c}\right|^2 . \tag{262}$$

8.3.4. *Scattering by a grid of graphene micro-ribbons*

After checking two special cases of the general expressions, we now want to address an example where the full set of Eqs. (255) - (258) has to be used. This particular problem was considered in Ref. [44]. For an array of graphene ribbons, the Fourier coefficients in Eq. (221) are given by $\mathcal{S}_0 = d_g/D$ and

$$\mathcal{S}_l = \frac{1}{l\pi}\sin\frac{l\pi d_g}{D} e^{-il\pi d_g/D}\,; \qquad l \neq 0\,. \tag{263}$$

In Fig. 26 we represent the absorbance and the transmittance of a grid of graphene ribbons for different values of the broadening Γ. This calculation required 600 reciprocal lattice vectors. The same quantities for uniform (pristine) graphene are represented by dashed curves. For small values of Γ, both the absorbance and the transmittance spectra present a set of resonances, with the most prominent one at low energies. On the other hand, for large Γ, the weaker resonances are washed away and the most prominent one becomes less pronounced. Compared to the case of pristine graphene, the absorption is suppressed at low energies whereas the transmittance is increased. The energy of the largest resonance is approximately given by $\hbar\Omega_p$ [see Eq.(64)] with $q = \pi/(2d_g)$, suggesting a coupling of the impinging ER to the SPPs modes of graphene. Unfortunately, the analysis is not so simple, because each ribbon has a finite size and the electron confinement has to be taken into account. The behaviour of the transmittance at low energies should also be noted. In the case of grid it tends to unity whereas in the pristine graphene case it attains its lowest values. The grid transmits more at low energies although the size of the gaps between the ribbons is much smaller than the wavelength of the incoming radiation.

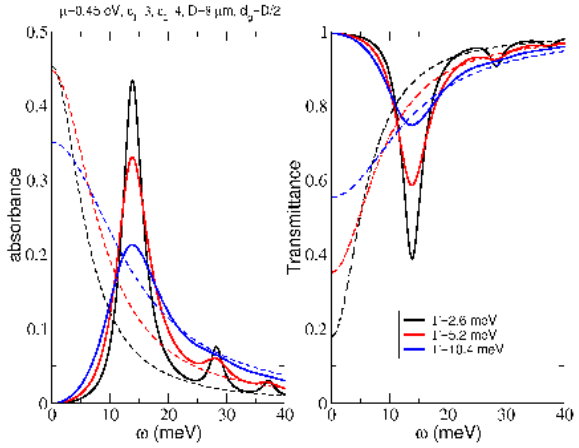

Fig. 26. Absorbance (left) and transmittance (right) of a grid of graphene ribbons for different values of the broadening Γ. The dashed lines are the absorbance/transmittance curves for pristine graphene for the same Γ values and chemical potential E_F. The parameters are: $E_F = 0.45$ eV, $D = 8$ μm, $d_g = D/2$, $\epsilon_1 = 4$, and $\epsilon_2 = 3$.

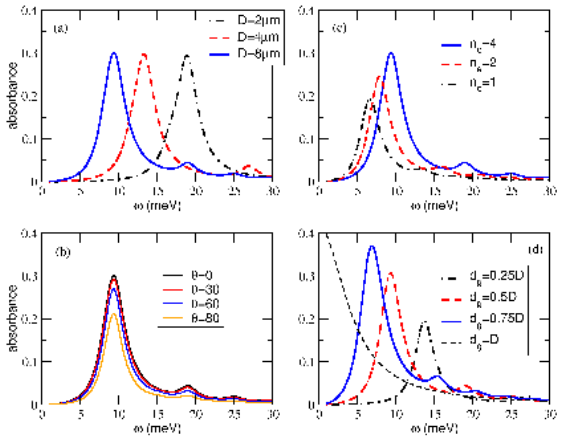

Fig. 27. Absorbance of a grid of graphene ribbons: (a) dependence on the lattice parameter D; (b) dependence on the angle of incidence; (c) dependence on the electronic density; (d) dependence on the width of the graphene ribbon (keeping the width of the unit cell constant). The parameters for the reference curve (solid blue) are: $E_F = 0.23$ eV, $D = 8$ μm, $\epsilon_1 = 5$, $\epsilon_2 = 3$, and $\Gamma = 2.6$ meV. In panel (c) n_e is given in units of 10^{12} cm^{-2}.

In Fig. 27 we study the effect of different parameters of the problem on the absorbance curve. In panel (a) we find the variation of absorbance with the parameter D, keeping $d_g = D/2$. The shift of the absorbance maximum scales as

$$\omega_{\max} \propto \sqrt{\frac{1}{D}}\,. \tag{264}$$

In panel (b), the dependence of the absorbance on the angle of incidence, θ, is given. No appreciable effect is seen here, except close to grazing incidence. We will see below that in the case of a continuous sheet with a modulated conductivity the situation is quite different. In panel (c), the dependence on the electronic density is shown (the values on the plot are given in units of 10^{12} cm^{-2}). The red shift scales with n_e as

$$\omega_{\max} \propto (n_e)^{1/4} \,. \tag{265}$$

Finally, in panel (d) we present the dependence of the absorbance on d_g, keeping D constant and equal to 8 μm. The blue shift follows the scaling relation

$$\omega_{\max} \propto \sqrt{\frac{1}{d_g}} \,. \tag{266}$$

In this latter panel the absorbance of an infinite graphene sheet is also plotted. Clearly, there is an enhancement of absorption due to SPP around certain specific frequencies, where the absorbance is higher for the grid of ribbons than for an infinite graphene sheet. Relations (264), (265), and (266) have the same functional form of dependence on d_g and n_e as the SPP frequency in the continuous system for the wavenumber $q = \pi/2d_g$. Considering the case of Fig. 28, we predict a maximum at the frequency

$$\hbar\Omega_p \approx \sqrt{\frac{4\alpha}{\epsilon_1+\epsilon_2} E_F \hbar c q} = \sqrt{\frac{4}{137\times 8} 0.23 \times 0.2 \frac{\pi}{8}} \simeq 8.1 \text{ meV} \,, \tag{267}$$

a value close to the position of the first maximum in the absorbance spectrum.

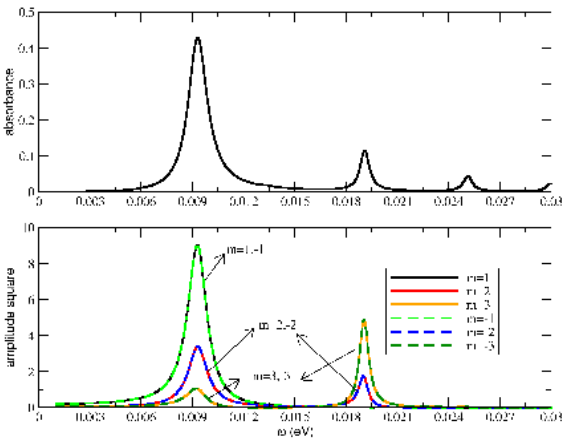

Fig. 28. Contribution of the first three harmonics to the absorbance curve. The reference curve (top panel) has $\Gamma = 0.6$ meV. Other parameters as in Fig. 27. In the bottom panel, the quantity $|\mathcal{E}_{1,x||n}/E_x^{(i)}|^2$ is depicted.

In order to understand the origin of the second maximum (and the third, as well) seen in the absorbance spectrum, we plotted in Fig. 28 the squared absolute value of the amplitude $\mathcal{E}_{1,x||n}/E_x^{(i)}$ for $n = \pm 1, \pm 2$ and ± 3. Clearly, the spectral weight associated with different harmonics is centered at the maxima observed in the absorbance spectrum. This representation gives a qualitative understanding of how the spectral weight associated with the different SPP modes in the infinite sheet is redistributed to form the absorbance spectrum in the periodic system. Different harmonics contribute differently to these maxima, for example, none of the depicted harmonics contribute to the maximum observed above 24 meV, only those with $|n| \geq 4$ contribute to it.

8.3.5. *Scattering from graphene sheet with cosine-modulated conductivity*

We next consider an example where the graphene sheet is continuous (as opposed to the grid of ribbons) and possesses a periodically modulated optical conductivity. As in Sec. 8.2, we assume a conductivity profile of the form (227), with the Fourier harmonics given by Eqs. (228) and (229). We shall see that, for angles of incidence different from zero, the absorbance peak will split into two, associated with the lattice vectors $G = \pm 2\pi/D$. We give below a derivation for the energy of the peaks as function of the angle of incidence. In the non-retarded approximation, the energy of the plasmon-polaritons is given by Eq. (64), with $\bar{\epsilon} = (\epsilon_1 + \epsilon_2)/2$. For an ER wave incoming at an angle of incidence θ, the wavevector of the excited SPP is given by

$$q = |k \sin\theta + nG| = |\frac{\omega\sqrt{\epsilon_1}}{c} \sin\theta - mG| \,. \tag{268}$$

From Eq. (63) for the SPP dispersion relation it follows that

$$q_p = |\frac{\omega\sqrt{\epsilon_2}}{c} \sin\theta + nG| = \frac{(\hbar\omega)^2}{4\alpha} \frac{\epsilon_1 + \epsilon_2}{E_F \hbar c} \,. \tag{269}$$

We assume that $G > \frac{\omega\sqrt{\epsilon_2}}{c}$. There are two possibilities:

(1) $n = -1$

$$\frac{(\hbar\omega)^2}{4\alpha} \frac{\epsilon_1 + \epsilon_2}{E_F\sqrt{\epsilon_2}} + \hbar\omega \sin\theta - G\hbar c/\sqrt{\epsilon_2} = 0 \,; \tag{270}$$

(2) $n = 1$

$$\frac{(\hbar\omega)^2}{4\alpha} \frac{\epsilon_1 + \epsilon_2}{E_F\sqrt{\epsilon_2}} - \hbar\omega \sin\theta - G\hbar c/\sqrt{\epsilon_2} = 0 \,. \tag{271}$$

Introducing the parameters

$$a = \frac{1}{4\alpha E_F} \frac{\epsilon_1 + \epsilon_2}{\sqrt{\epsilon_2}} \,, \tag{272}$$

and

$$b = G\frac{c\hbar}{\sqrt{\epsilon_2}}\,, \tag{273}$$

the solution of the two equations for $\omega(\theta)$ reads as

$$\hbar\omega = \pm\frac{\sin\theta}{2a} + \frac{1}{2a}\sqrt{\sin^2\theta + 4ab}\,, \tag{274}$$

for $n = 1$ and $n = -1$, respectively. Thus, we expect to observe a peak splitting for $\theta > 0$ at the left ($n = -1$) and at the right ($n = 1$) of the single peak at $\theta = 0$. We shall see that this is indeed the case.

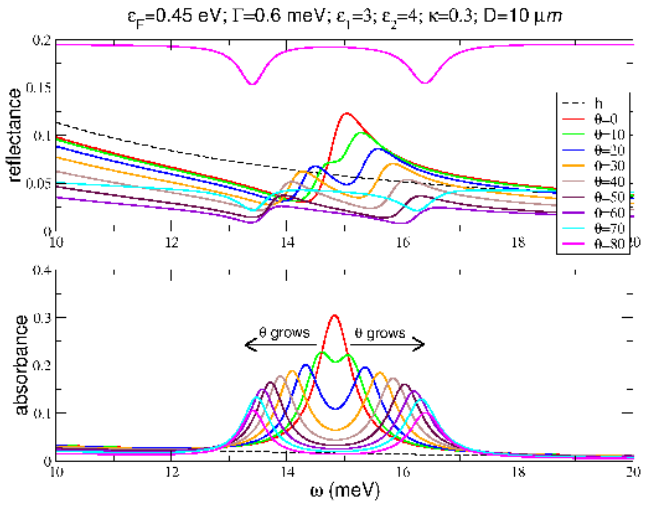

Fig. 29. Spectra of a graphene sheet with a cosine-modulated conductivity. Reflectance (top) and absorbance (bottom) *versus* frequency for different angles of incidence. The parameters are: $E_F = 0.452$ eV, $D = 10$ μm, $\epsilon_1 = 4$, $\epsilon_2 = 3$, $\Gamma = 0.6$ meV, and $h = 0.3$. The Brewster angle for these dielectrics is 49.1^o.

The linear system defined by Eqs. (243) and (244) is solved numerically and the sums over n are cut off at $n = -N, \ldots, 0, \ldots, N$. The numerical solution rapidly converges with N. Results for the specular reflectance, $\mathcal{R}_0$, and for the absorbance, $\mathcal{A} = 1 - \mathcal{R}_0 - \mathcal{T}_0$, are given in Fig. 29. For a modulated conductivity the momentum of the SPPs is conserved up to a reciprocal lattice vector nG, with $n = \pm 1, \pm 2, \ldots$, that is,

$$q_p = |k\sin\theta + nG|\,. \tag{275}$$

In this case, even for normal incidence, it is possible to excite SPPs. We stress that in the present case the Bragg scattering mechanism expressed in Eq. (275), allowing

to overcome the momentum mismatch between the propagating wave and SPPs, is induced entirely by the conductivity modulation and it is not a consequence of a external grating. The excitation of SPPs at normal incidence is illustrated in Fig. 29. The dashed black curve represents the behaviour of the system for a homogeneous conductivity and impinging ER at normal incidence; clearly the curve is featureless. For the inhomogeneous case, a large enhancement of the absorbance is seen around the energy given by Eq. (64) with $q_p = 2\pi/D$ (note that using this equation implies the extended band scheme). The position of the peak does not coincide exactly with the number given by Eq. (64) because this equation is not sensitive to the details of the band structure. From Fig. 25 we can observe that the bands for $n = \pm 1$ at the zone center have an energy of about 15 meV (the energy for which the reflectance curve has a maximum for $\theta = 0$). As the angle of incidence approaches the Brewster angle, Θ_B, for the two dielectrics, the reflectance decreases substantially. Note that the Brewster angle of the system is not given exactly by the usual formula, $\Theta_B = \arctan\sqrt{\epsilon_1/\epsilon_2}$, because of the presence of graphene. For incidence angles above Θ_B the reflectance develops two dips and can be larger than it would be for $\theta = 0$ (see curve for $\theta = 80^o$ in Fig. 29).

When the incoming beam deviates from normal incidence (i. e. $\theta \neq 0$), there is a peak splitting both in the reflectance and in the absorbance curves, as predicted above. We would like to understand in qualitative terms the behaviour of the splitting as function of θ. Using Eq. (275) in Eq. (64) yields

$$\hbar\Omega_p = \sqrt{\frac{2\alpha}{\bar{\epsilon}} E_F \hbar c |k \sin\theta + nG|}\,. \tag{276}$$

Clearly, when $n > 0$ and θ increases, the frequency shifts toward higher energies. On the other hand, when $n < 0$, the energy decreases as θ increases. This behavior can be understood from the analysis of Fig. 25. For $\theta = 0$ the light line, Eq. (113), is vertical and touches the second band at the center of the Brillouin zone ($q = 0$) where the branches associated with $n = 1$ and $n = -1$ almost touch each other (they do touch within the non-retarded approximation, see Fig. 25). As θ grows, the slope of light line decreases and the branches with both $n = 1$ and $n = -1$ split away.

In Fig. 30 we plot the two branches of Eq. (274) and compare them with the positions of the absorbance peaks obtained from Fig. 29. The agreement is only qualitative because, first, Eq. (274) is derived from a kinematic argument and, therefore, misses the dependence on h (and, eventually, some symmetries a particular problem may have) and, secondly, we used the non-retarded approximation. However, for small h the agreement is quite good. Indeed, if we shift the solid curves in Fig. 30 by adding a constant, they would fit the points (solid squares) obtained from Fig. 29. In the bottom panel of Fig. 30 we plot $|r_{x||\pm1}|^2$ for different θ as a function of the energy. The energies of the peaks of $|r_{x||\pm1}|^2$ are the same as those of the transmittance minima (absorbance maxima). This shows that the polaritons of the $n = \pm 1$ branches with the wavevector $q_p \approx 0$ are responsible for the features

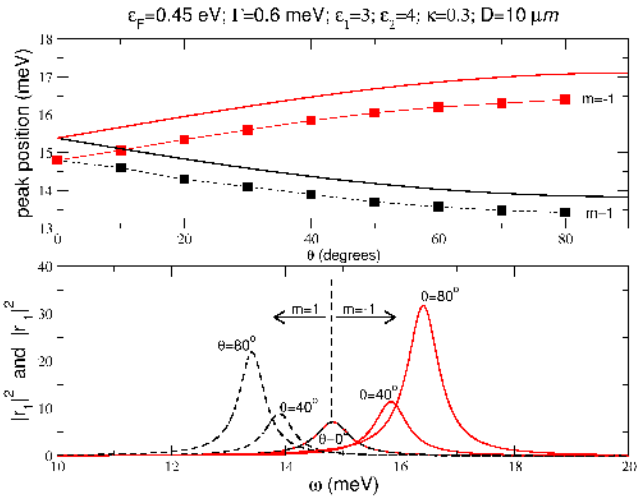

Fig. 30. Position of the absorbance peak as function of the angle of incidence. Top: dependence of the absorbance peak energy upon the angle. The lines with squares are obtained from the bottom panel of Fig. 29; the solid lines are the two branches of Eq. (274). The bottom panel shows the squared absolute values of the amplitudes of the modes associated with the SPPs of momentum $\pm G$. The parameters are the same of Fig. 29.

in the reflectance, transmittance and absorbance spectra.

9. Scattering of ER from corrugated graphene

9.1. *Setting the problem and definitions*

In Secs. 6, 7 and 8 we have seen that resonant coupling between ER and SPPs can be achieved either using the ATR scheme (Otto configuration), or due to a topological defect on graphene or its modulated conductivity. Another possibility is the use of a dielectric grating [103]. In what follows we discuss the coupling of ER to SPPs in graphene-based gratings.

We want to solve the scattering problem of light impinging on a diffraction grating, as schematically represented in Fig. 31. The region 1 is such that $z > \max[a(x)]$, whereas the region 1^- is such that $a(x) < z < \max[a(x)]$. A similar definition applies to the regions 2 and 2^+ when $z < \min[a(x)]$ and $\min[a(x)] < z < a(x)$, respectively. In general, the calculation of the fields in the regions 2^+ and 1^-, i.e. $\min[a(x)] < z < \max[a(x)]$ is a challenging problem.

It will be assumed that in both regions 1 and 2 the dielectric functions, ϵ_1 and ϵ_2, are constant. For a TM wave we have Maxwell's equations (11), (13) and (15), while the electromagnetic fields in regions 1 and 2 are the same as represented by Eqs. (230), (231) and (232). The Rayleigh-Fano approximation (also called Rayleigh hypothesis) assumes that Rayleigh expansions (see below) are valid in the regions 1^- and 2^+, which is not true in general [8] (for example, the method fails for rectangular

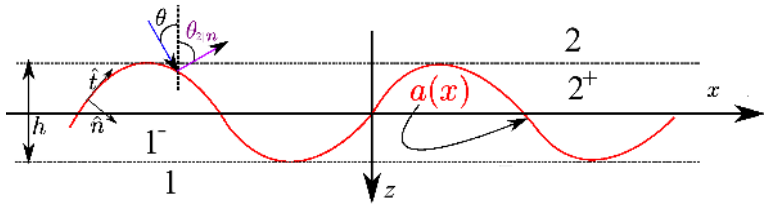

Fig. 31. Grating geometry and different regions referred in the text. Graphene follows the profile $a(x)$.

gratings). However, in the case of smooth grating profiles it can be proved that the solution of Maxwell's equations exists and is unique [104,105], and can be approximated by linear combinations of reflected and transmitted waves in the regions 1^- and 2^+ (see Ref. [105] for details).

Since we are dealing with a corrugated surface, we need to defined tangent and normal vectors to the curve $z = a(x)$ (see Fig. 31). The unit vector tangent to the curve $z = a(x)$ at point x is given by

$$\hat{t} = \frac{1}{\sqrt{1 + \left(\frac{da}{dx}\right)^2}} \left(\hat{x} + \frac{da}{dx}\hat{z}\right) , \quad |\hat{t}| = 1. \tag{277}$$

The normal unit vector to the curve is

$$\hat{n} = \frac{1}{\sqrt{1 + \left(\frac{da}{dx}\right)^2}} \left(-\frac{da}{dx}\hat{x} + \hat{z}\right) , \quad |\hat{n}| = 1; \tag{278}$$

and clearly $\hat{n} \cdot \hat{t} = 0$. Since the current density vector is tangent to the graphene sheet, we must have $\vec{J}_s = \sigma \vec{E}_t = \sigma E_t \hat{t}$, where E_t is given by

$$E_t = \vec{E} \cdot \hat{t} = \frac{1}{\sqrt{1 + \left(\frac{da}{dx}\right)^2}} \left(E_x + \frac{da}{dx}E_z\right) . \tag{279}$$

One of the boundary conditions (7) requires the determination of the vector product $\vec{J}_s \times \hat{n}$:

$$\vec{J}_s \times \hat{n} = -\frac{\sigma}{\sqrt{1 + \left(\frac{da}{dx}\right)^2}} \left(E_x + \frac{da}{dx}E_z\right) \hat{z} , \tag{280}$$

and the respective boundary condition $B_{1,y}(x,z)\hat{y} - B_{2,y}(x,z)\hat{y} = \mu_0 \sigma \vec{J} \times \hat{n}$ reads

$$B_{1,y}(x,z) - B_{2,y}(x,z) = -\frac{\mu_0 \sigma}{\sqrt{1 + \left(\frac{da}{dx}\right)^2}} \left(E_x + \frac{da}{dx}E_z\right) . \tag{281}$$

The second boundary condition is $\vec{E}_{1,t} = \vec{E}_{2,t}$, which can be written as

$$E_{1,x}(x,z) + \frac{da}{dx}E_{1,z}(x,z) = E_{2,x}(x,z) + \frac{da}{dx}E_{2,z}(x,z) . \tag{282}$$

These boundary conditions are to be applied to a general profile $a(x)$.

9.2. *Rayleigh method by Toigo et al.*

We give a representation of Rayleigh equations based on Ref. [8]. Using Eqs. (230)-(232), the boundary conditions, Eqs. (281)-(282), can be written in terms of the x-component of the electric field as

$$\epsilon_1 \sum_n \frac{\mathcal{E}_{1,x||n}}{\kappa_{1||n}} e^{i[(q+nG)x-\kappa_{1||n}a(x)]} + \epsilon_2 \sum_n \frac{\mathcal{E}_{2,x||n}}{\kappa_{2||n}} e^{i[(q+nG)x+\kappa_{2||n}a(x)]} - i\frac{\epsilon_2}{k_z} E_x^{(i)} e^{i[qx+k_z a(x)]} = -i\frac{\sigma}{\epsilon_0\omega\sqrt{1+\left(\frac{da}{dx}\right)^2}} \sum_n \left[1 + i\frac{da}{dx}\frac{q+nG}{\kappa_{1||n}}\right] \times \mathcal{E}_{1,x||n} e^{i[(q+nG)x-\kappa_{1||n}a(x)]}\,; \quad (283)$$

$$\sum_n \mathcal{E}_{1,x||n} e^{i[(q+nG)x-\kappa_{1||n}a(x)]} \left[1 + i\frac{da}{dx}\frac{q+nG}{\kappa_{1||n}}\right] = \sum_n \mathcal{E}_{2,x||n} e^{i[(q+nG)x+\kappa_{2||n}a(x)]} \left[1 - i\frac{da}{dx}\frac{q+nG}{\kappa_{2||n}}\right] + \left[1 - \frac{da}{dx}\frac{q}{k_z}\right] E_x^{(i)} e^{i[qx+k_z a(x)]}\,. \quad (284)$$

Eqs. (283),(284) were obtained using Eqs. (83)-(84) (replacing ϵ_3 by ϵ_2) and (208)-(209). The boundary conditions are applied at $z = a(x)$. Multiplying Eq. (283) by $e^{-i(q+pG)x}$ and integrating over $\int_0^D dx/D$, we obtain

$$\epsilon_1 \sum_n \frac{\mathcal{E}_{1,x||n}}{\kappa_{1||n}} M_{1||p-n} + \epsilon_2 \sum_n \frac{\mathcal{E}_{2,x||n}}{\kappa_{2||n}} M_{2||p-n} - i\frac{\epsilon_2}{k_z} E_x^{(i)} M_p^{(i)} = -i\frac{\sigma}{\epsilon_0\omega} \sum_n \left(L_{p-n} + i\frac{q+nG}{\kappa_{1||n}} N_{p-n}\right) \mathcal{E}_{1,x||n}\,, \quad (285)$$

where

$$M_p^{(i)} = \frac{1}{D}\int_0^D dx e^{-ipGx} e^{ik_z a(x)}\,, \quad (286)$$

$$M_{m||p-n} = \frac{1}{D}\int_0^D dx e^{-i(p-n)Gx} e^{(-1)^m \kappa_{m||n} a(x)}\,, \quad (287)$$

$$L_{p-n} = \frac{1}{D}\int_0^D dx \frac{e^{-i(p-n)Gx}}{\sqrt{1+\left(\frac{da}{dx}\right)^2}} e^{-\kappa_{1||n}a(x)} \approx M_{1||p-n}\,, \quad (288)$$

$$N_{p-n} = \frac{1}{D}\int_0^D dx \frac{da}{dx}\frac{e^{-i(p-n)Gx}}{\sqrt{1+\left(\frac{da}{dx}\right)^2}} e^{-\kappa_{1||n}a(x)} \approx -i\frac{(p-n)G}{\kappa_{1||n}} M_{1||p-n}\,. \quad (289)$$

After some manipulations we arrive at the following equation:

$$\sum_n \left(\frac{\epsilon_1}{\kappa_{1||n}} + i\frac{\sigma}{\epsilon_0\omega} \frac{(q+nG)(q+pG) - \omega^2\epsilon_1/c^2}{\kappa_{1||n}^2} \right) \mathcal{E}_{1,x||n} M_{1||p-n} = -\epsilon_2 \sum_n \frac{\mathcal{E}_{2,x||n}}{\kappa_{2||n}} M_{2||p-n} + i\frac{\epsilon_2}{k_z} E_x^{(i)} M_p^{(i)} \,, \tag{290}$$

In a similar manner, multiplying Eq. (284) by $e^{-i(q+pG)x}$ and integrating over $\int_0^D dx/D$, we obtain:

$$\sum_n \frac{(q+nG)(q+pG) - \omega^2\epsilon_1/c^2}{\kappa_{1||n}^2} \mathcal{E}_{1,x||n} M_{1||p-n} = \sum_n \frac{(q+nG)(q+pG) - \omega^2\epsilon_2/c^2}{\kappa_{2||n}^2} \mathcal{E}_{2,x||n} M_{2||p-n} + \sum_n \frac{\omega^2\epsilon_1/c^2 - q(q+pG)}{k_z^2} E_x^{(i)} M_p^{(i)} \,. \tag{291}$$

Solution of the boundary problem (290) and (291) will allow for the calculation of the reflectance, transmittance, and absorbance spectra.

9.3. *Three limiting cases*

First, we will show that, if $a(x) = 0$ and $E_x^{(i)} = 0$, one obtains from Eqs. (290) and (291) the usual SPP spectrum folded into the first Brillouin zone. When $a(x) = 0$, we have $M_{m||p-n} = \delta_{p,n}$ and Eqs. (290) and (291) reduce to

$$\left(\frac{\epsilon_1}{\kappa_{1||p}} + i\frac{\sigma}{\epsilon_0\omega} \right) \mathcal{E}_{1,x||p} = -\epsilon_2 \frac{\mathcal{E}_{2,x||p}}{\kappa_{2||p}} \,; \qquad \mathcal{E}_{1,x||p} = \mathcal{E}_{2,x||p} \,. \tag{292}$$

Solving for $\mathcal{E}_{2,x||p}$, we obtain

$$\frac{\epsilon_1}{\kappa_{1||p}} + \frac{\epsilon_2}{\kappa_{2||p}} + i\frac{\sigma}{\epsilon_0\omega} = 0 \,. \tag{293}$$

Since the SPP amplitude decays away from the graphene sheet, we consider $\kappa_{m||n}$ in the form (207) with $q \in [-\pi/D, \pi/D]$. With this choice we recover Eq. (47) folded into the first Brillouin zone.

When $E_x^{(i)}$ is finite, we have a scattering problem. In this case $M_p^{(i)} = \delta_{p,0}$ and Eqs. (290) and (284) reduce to

$$\left(\frac{\epsilon_1}{\kappa_{1||0}} + i\frac{\sigma}{\epsilon_0\omega} \right) \mathcal{E}_{1,x||0} = -\epsilon_2 \frac{\mathcal{E}_{2,x||0}}{\kappa_{2||0}} + i\frac{\epsilon_2}{k_z} E_x^{(i)} \,, \tag{294}$$

$$\mathcal{E}_{1,x||0} = \mathcal{E}_{2,x||0} + E_x^{(i)} \,.$$

In the limit $\sigma = 0$ we obtain Eq. (260), the well-known reflectance amplitude from elementary optics. In the case $\sigma \neq 0$ and $\epsilon_1 = \epsilon_2$ we obtain Eq. (262), which gives the transmittance amplitude for graphene.

9.4. *A non-trivial example I: sine profile*

The last two examples are trivial for they refer to the limit of zero curvature. We now consider a non-trivial case where graphene has a well defined periodic corrugation. We assume a profile of the form

$$a(x) = h\sin(2\pi x/D)\,, \tag{295}$$

from which follows $da/dx = (2\pi h/D)\cos(2\pi x/D)$. For this choice of profile the Rayleigh hypothesis is exact. We have:

$$M_p^{(i)} = J_p(k_z h)\,, \tag{296}$$

$$M_{m||p-n} = J_{p-n}[i(-1)^{m+1}\kappa_{m||n}h] = i^{p-n}I_{p-n}[(-1)^{m+1}\kappa_{m||n}h]\,, \tag{297}$$

where $J_p(z)$ and $I_p(z)$ are the usual and modified Bessel functions of order p, respectively.

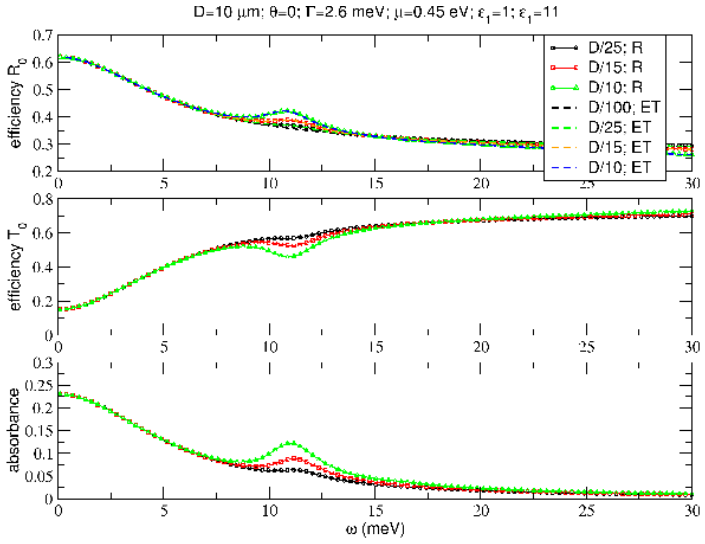

Fig. 32. Dependence of the reflectance, transmittance and absorbance on frequency for different depth of the grooves for sine profile gratings. We compare the Rayleigh method with the results from the extinction theorem. In the legend, the label R stands for the Rayleigh approximation whereas the label ET stands for the extinction theorem result. The parameters are $E_F = 0.45$ eV, $D = 10$ μm, $\epsilon_1 = 1$, $\epsilon_2 = 11$ (silicon), $\Gamma = 2.6$ meV, and $\theta = 0$.

In Fig. 32 we represent the efficiencies $\mathcal{R}_0$ and $\mathcal{T}_0$ (top and central panels, respectively), and the absorbance, $\mathcal{A} = 1 - \mathcal{R}_0 - \mathcal{T}_0$, as functions of the incoming photon energy, for different values of the ratio h/D. When $h/D \ll 1$, we recover the properties of a flat graphene sheet. We compare results from the Rayleigh approximation described above with those produced by the extinction theorem method (dashed

curves), an exact integral-equation approach to the scattering problem [8,77]. We see that the agreement is excellent. In Fig. 33 the quality of the agreement between the two methods is more evident. In this figure we compare the dependence of the specular reflectance $\mathcal{R}_0$ on frequency, for several angles of incidence θ and $h/D = 0.1$. The resonance seen in Figs. 32 and 33 above 10 meV is due to the excitation of a surface-plasmon-polariton of energy

$$\hbar\Omega_p = \sqrt{\frac{4\alpha}{\epsilon_1+\epsilon_2} E_F c\hbar \frac{2\pi}{D}} \approx 11 \text{ meV}\,. \tag{298}$$

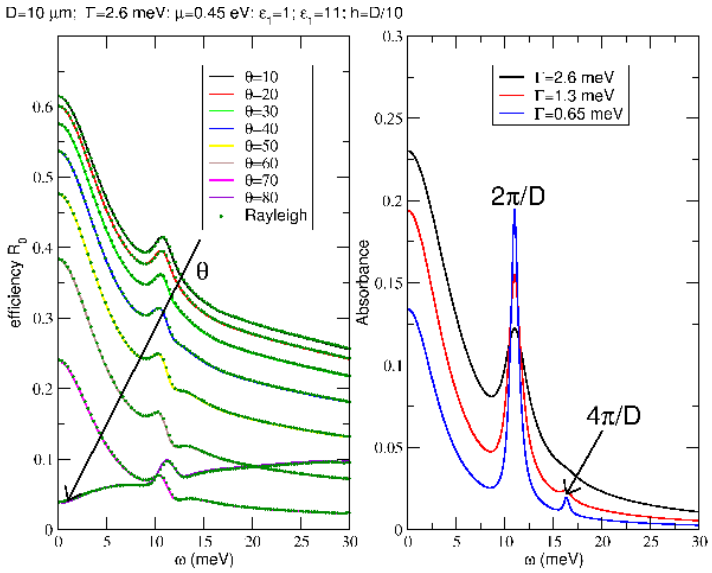

Fig. 33. Left: Dependence of the reflectance on the angle of incidence for a sine profile grating. We compare the Rayleigh method (solid circles) with the results from the extinction theorem approach (solid lines). The arrow indicates the direction of growth of the angle θ. Right: absorbance for different values of the broadening Γ, at normal incidence. Other parameters are as in Fig. 32.

In the right panel of Fig. 33 we present the absorbance, $\mathcal{A}$, for different values of Γ. As Γ decreases, the resonance in the absorbance becomes more prominent. Also, the coupling of the ER to the SPP of wave number $4\pi/D$ (extended band scheme) becomes evident as a smaller resonance.

9.5. *A non-trivial example II: sawtooth profile*

In the case of a sawtooth profile the function $a(x)$ reads (see Fig. 34):

$$a(x) = \begin{cases} \frac{2h}{D}x + \frac{h}{2}, & -D/2 < x < 0\,, \\ -\frac{2h}{D}x + \frac{h}{2}, & 0 < x < D/2\,. \end{cases} \tag{299}$$

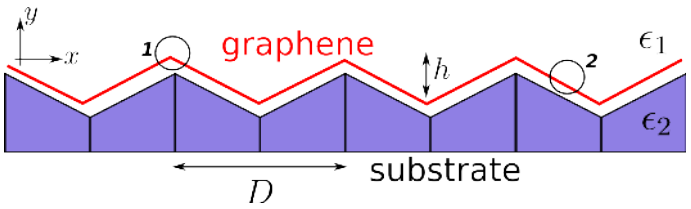

Fig. 34. Periodic patterned substrate with a sawtooth profile. In regions with the label 1 the strain is expected to be higher than in those with label 2. Then, the problem of scattering by such grating also includes the previously considered case of a periodically modulated conductivity.

In this case the functions $M_p^{(i)}$ and $M_{m||p-n}$ can be written as

$$M_p^{(i)} = \frac{ik_z h}{\pi^2 p^2 - k_z^2 h^2}\left[e^{ik_z h/2} - (-1)^p e^{-ik_z h/2}\right], \tag{300}$$

$$M_{m||p-n} = \frac{(-1)^m \kappa_{m||n} h}{\pi^2 (p-n)^2 + \kappa_{m||n}^2 h^2} \times \left[e^{(-1)^m \kappa_{m||n} h/2} - (-1)^{p-n} e^{(-1)^{m+1} \kappa_{m||n} h/2}\right]. \tag{301}$$

Contrary to the case of the sine profile, the Rayleigh method for the sawtooth profile is neither convergent for some values of h, for a given ω, nor for a given h for all values of ω. We have checked that partial convergence requires $h \lesssim D/10$. The convergence over an energy range has to be checked case by case.

In Fig. 35 we plot the absorvance, reflectance, and transmittance for a grating with a sawtooth profile where the convergence could be achieved. As in the case of the sinusoidal profile discussed in Sec. 9.4, we see the presence of resonances associated with the coupling of the impinging ER with the graphene SPPs. For $\theta = 0$ the resonance is located at $\hbar\omega \approx 11.6$ meV. As before, the value can be predicted from:

$$\hbar\Omega_p = \sqrt{\frac{4\alpha}{\epsilon_1 + \epsilon_2} E_F \hbar c q_p} \tag{302}$$

$$= \sqrt{\frac{4}{137 \times 12} 0.452 \times 0.2 \frac{2\pi}{10}} \approx 11.8 \text{ meV}. \tag{303}$$

At finite angles of incidence, the single peak seen at $\theta = 0$ splits into two peaks because the ATR scan line intercepts the $n = -1, 1$ bands at different energies. The prediction for the positions of the two peaks follows from the calculation of the band structure of the SPPs for the sawtooth profile. It is interesting to note that the peak splitting does not occur in the case of the sine profile.

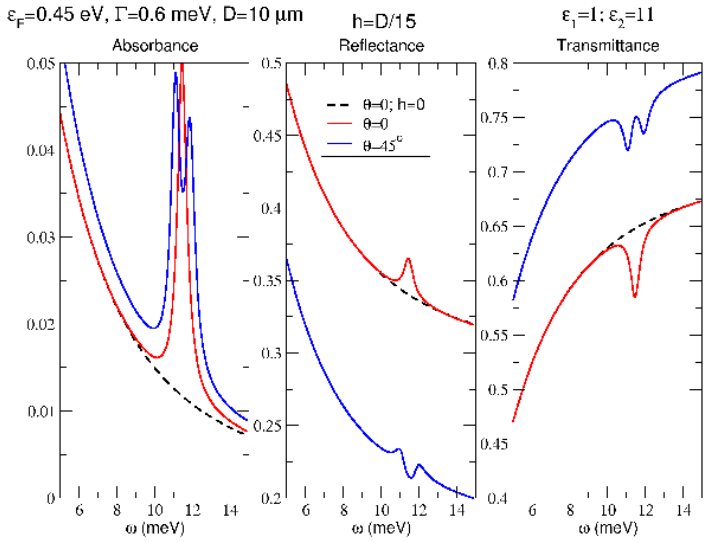

Fig. 35. Absorbance, reflectance and transmittance for the sawtooth profile at two angles of incidence, $\theta = 0$ and $\theta = 45^o$. The dashed lines refer to the non-corrugated limit for $\theta = 0$. Here $h/D = 1/15$ and $\Gamma = 0.6$ meV; other parameters as in Fig. 32.

10. Graphene on a metallic grating

10.1. *Relation between the conductivity and the dielectric function of a 3D metal*

So far we have discussed the resonant coupling of ER to SPPs in graphene lying on a dielectric grating. In this section we shall consider the case where the underlying grating is made of a conductor, be it a metal, a doped semiconductor, or a mesostructure [106].

Let us first derive a simple relation between the conductivity and the dielectric function of a 3D metal, based on Drude's model [107]. The equation of motion of an electron in a metal subject to an oscillating electric field is

$$m_e \frac{d^2x}{dt^2} + m_e\gamma\frac{dx}{dt} = -eE(\omega)^{-i\omega t}\,, \tag{304}$$

where m_e denotes the electron mass and $-e$ is the electron charge. Substituting $x = x_0 e^{-i\omega t}$, into Eq. (304) we obtain

$$x_0 = \frac{eE(\omega)}{m_e\omega(\omega + i\gamma)}\,. \tag{305}$$

The polarization is defined as $P(\omega) = -en_e x_0$ (units of C/m^2), where n_e is the electronic density (per unit volume) of the gas. The electric displacement field is

defined as

$$D(\omega) = \varepsilon_0 \epsilon(\omega) E(\omega) = \varepsilon_0 E(\omega) + P(\omega)$$
$$= \varepsilon_0 E(\omega) - \frac{e^2 n_e E(\omega)}{m_e \omega(\omega + i\gamma)} \,. \tag{306}$$

Therefore, we have

$$\epsilon(\omega) = 1 - \frac{e^2 n_e/\varepsilon_0}{m_e \omega(\omega + i\gamma)} \,. \tag{307}$$

On the other hand, Drude's model for the conductivity reads [107]

$$\sigma_{3\mathrm{D}} = \frac{e^2 n_e}{m_e(\gamma - i\omega)} \,. \tag{308}$$

Comparing Eqs. (307) and (308) we obtain

$$\epsilon(\omega) = 1 + i\frac{\sigma_{3\mathrm{D}}}{\varepsilon_0 \omega} \,. \tag{309}$$

If the dielectric screening by core electrons of the metal atoms is taken into account, the unity in Eq. (309) must be replaced by a background dielectric constant $\epsilon_\infty > 1$ [95]. For instance, for gold $\epsilon_\infty = 1.53$ [108], while for most semiconductors it is of the order of 10.

Thus, when dealing with a 3D metal the conductivity enters the problem through the dielectric function. Often it can be assumed that $\gamma \ll \omega$, leading to a purely real dielectric function, that is, the metal acts as a dispersive dielectric with a dielectric constant that can negative. In this limit, the dielectric function has the simple form

$$\epsilon(\omega) = \epsilon_\infty - \frac{\omega_p^2}{\omega^2} \,, \tag{310}$$

where $\omega_p^2 = n_e e^2/(m_e \epsilon_0)$ denotes the plasma frequency of the bulk conductor. Although it is, of course, measured in s^{-1}, for convenience we shall use values in meV, which correspond to plasma energy $\hbar\omega_p$.

10.2. *Surface plasmon–polaritons at a dielectric-metal interface*

Before discussing the form of the spectrum of SPPs when graphene is placed on a bulk conductor, we analyze the simpler case of a dielectric-metal interface. We assume a system where a dielectric of constant permittivity ϵ_2 is in contact with a bulk metal of dielectric function $\epsilon(\omega)$. The dispersion relation can be obtained from Eq. (47) by putting $\sigma \equiv 0$ and substituting ϵ_1 by $\epsilon(\omega)$, namely

$$\frac{\epsilon(\omega)}{\kappa_1} + \frac{\epsilon_2}{\kappa_2} = 0 \,, \tag{311}$$

where $\kappa_1^2 = q^2 - \epsilon(\omega)\omega^2/c^2$ and $\kappa_2^2 = q^2 - \epsilon_2\omega^2/c^2$. As a result, for real values of κ_1 and κ_2, $\epsilon(\omega)$ has to be real and negative, implying $\omega < \omega_p$. Sometimes in the

literature the eigenvalue equation (311) appears in the form

$$q = \frac{\omega}{c}\sqrt{\frac{\epsilon_2\epsilon(\omega)}{\epsilon_2+\epsilon(\omega)}}\,, \tag{312}$$

which can be easily obtained from Eq. (311). Note that, since the argument in the square root above must be positive, it is necessary that $\epsilon(\omega) < -\epsilon_2$ and $\omega < \omega_p/\sqrt{\epsilon_\infty+\epsilon_2}$, which gives an upper bound for the SPP frequencies.

We can solve Eq. (311) for ω:

$$\omega^2 = \frac{\omega_p^2}{2\epsilon_\infty} + \frac{c^2q^2}{2}\frac{\epsilon_\infty+\epsilon_2}{\epsilon_2\epsilon_\infty} - \frac{1}{2\epsilon_2\epsilon_\infty}\sqrt{[\omega_p^2\epsilon_2 + c^2q^2(\epsilon_\infty+\epsilon_2)]^2 - 4\epsilon_2\epsilon_\infty c^2q^2\omega_p^2}\,. \tag{313}$$

The minus sign in front of the square root is necessary to guarantee that $\omega < \omega_p/\sqrt{\epsilon_\infty+\epsilon_2}$. This relation takes simple forms in two limiting cases. When $q \to 0$, we have

$$\omega^2 = \frac{c^2q^2}{\epsilon_2} - \frac{c^4q^4(\epsilon_2+\epsilon_\infty)^2}{4\epsilon_2^2\epsilon_\infty\omega_p^2}\,. \tag{314}$$

In this case, the dispersion relation of SPPs is always below the spectrum of the ER in the dielectric, a situation that does not occur for SPPs on graphene (recall Sec. 4).

For $q \to \infty$ we obtain

$$\omega^2 = \frac{\omega_p^2}{\epsilon_\infty+\epsilon_2} - \frac{\epsilon_2\omega_p^4}{4\epsilon_\infty(\epsilon_\infty+\epsilon_2)c^2q^2}\,, \tag{315}$$

that is, the dispersion relation is always below $\omega_p/\sqrt{\epsilon_\infty+\epsilon_2}$. Clearly, the dispersion curve of the surface plasmon–polaritons at the surface of a 3D metal is quite different from that for a 2D conductor (see Sec. 4).

10.3. *Graphene on a metallic grating*

As known, for frequencies below the plasma frequency a bulk metal reflects all light impinging on it, a consequence of the negative value of its dielectric permittivity.[a] If the surface of the metal has a periodic corrugation, the energy of the reflected wave is distributed among the specular and the diffracted orders, as seen in Fig. 36. In this figure we depict three reflectance efficiencies, $\mathcal{R}_0$, $\mathcal{R}_1$, and $\mathcal{R}_{-1}$, for normal incidence of the impinging radiation. As expected for normal incidence, we have $\mathcal{R}_1 = \mathcal{R}_{-1}$. Since we are considering the limit of a dispersive metal with no absorption, there is no dissipation due to SPPs. The rich structure seen in $\mathcal{R}_0$, $\mathcal{R}_1$, and $\mathcal{R}_{-1}$ spectra is due to the distribution of the energy through the different diffraction orders. The

[a]Strictly speaking, this is true for $\epsilon_\infty = 1$, zero damping and neglecting interband or impurity-related optical transitions that may take place in the same spectral region.

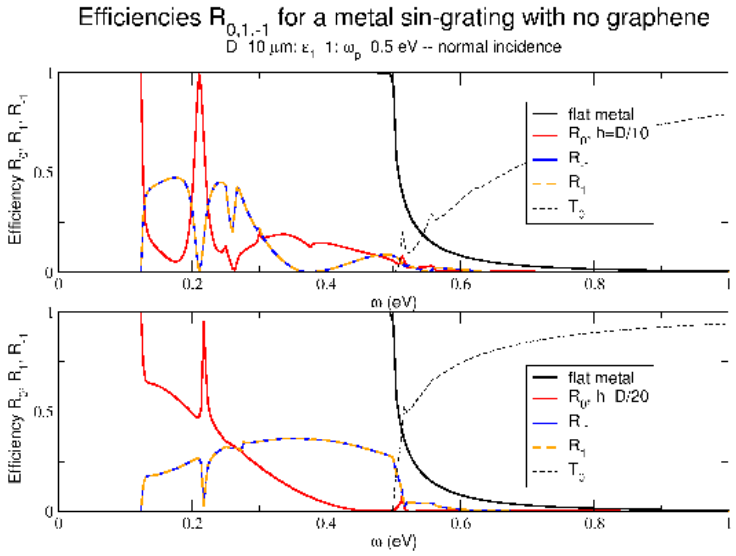

Fig. 36. Reflectance and transmittance of a sinusoidal metallic grating (without graphene). We depict three reflectance efficiencies, $\mathcal{R}_0$, $\mathcal{R}_1$, and $\mathcal{R}_{-1}$. The specular transmittance $\mathcal{T}_0$ is also depicted as a dashed line; $\mathcal{T}_0 \neq 0$ only for $\omega > \omega_p$. The parameters are: $\epsilon_1 = \epsilon_\infty = 1$, $\hbar\omega_p = 0.5$ eV, $D = 10$ μm, $h = D/10$ (top), and $h = D/20$ (bottom).

interpretation of the figure is rather difficult because the problem is non-linear in the frequency ω. For energies below 0.12 eV (smaller than the plasma frequency taken equal to 0.5 meV) only the specular ($\mathcal{R}_0$) order is propagating. Since the absorption of the metal was neglected the reflectance is equal to unity; this corresponds to frequencies $\omega/c < G$. Above 0.12 eV the orders $n = \pm 1$ ($\mathcal{R}_{\pm 1}$) also become propagating and we have Bragg diffraction (orders with $|n| > 1$ are evanescent; this corresponds to frequencies $G < \omega/c < 2G$). In this case SPPs with the wavevectors $\pm G$, excited by the incoming light thanks to the presence of the grating, become radiative (non-evanescent) and the diffracted energy is distributed among the three orders $n = 0, \pm 1$ in a non-trivial way. In this case we have $\mathcal{R}_0 + \mathcal{R}_1 + \mathcal{R}_{-1} = 1$, since there is no dissipation in the metal. Above the plasma frequency the grating becomes partially transparent. As the frequency of the incoming ER increases the dielectric function of the metal tends to ϵ_∞ and $\mathcal{T}_0 \to 1$, as seen in Fig. 36.

If we deposit graphene on top of a corrugated metal surface, the system has two different regimes. For frequencies smaller than $\omega_p/\sqrt{\epsilon_\infty + \epsilon_2}$ the system behaves essentially as the surface of a bulk conductive system. When $\omega > \omega_p/\sqrt{\epsilon_\infty + \epsilon_2}$ the system behaves as a graphene sheet on a dispersive dielectric. The problem of the plasmon spectrum of a graphene sheet in the vicinity of a thick plasma-containing substrate was considered by Horing [109], who derived the dispersion relation of the surface plasmons of the system.

In what follows, we assume that graphene is deposited on a metallic grating, as

illustrated in Fig. 37.

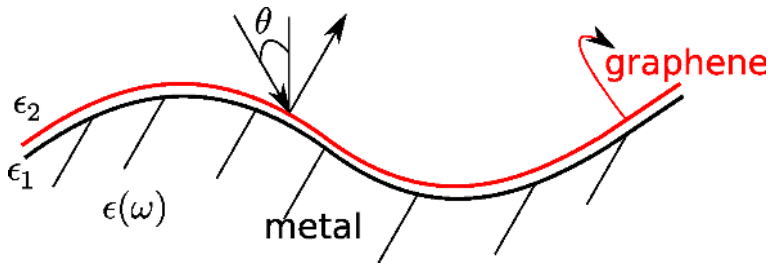

Fig. 37. Graphene on a metal. The upper and lower media have dielectric permittivities ϵ_2 and $\epsilon_1 \equiv \epsilon(\omega)$, respectively.

For the metal we take a dielectric function corresponding to the limit of a dispersive conductor, that is, given by Eq. (310). For simplicity, we shall assume $\epsilon_\infty = 1$. We want to study the form of the dispersion relation of the surface plasmon–polaritons. In this case, the eigenvalue equation has the same form as Eq. (47),

$$1 + \frac{\kappa_2 \epsilon(\omega)}{\kappa_1 \epsilon_2} + i\sigma_g \frac{\kappa_2}{\omega \epsilon_0 \epsilon_2} = 0\,. \tag{316}$$

Let us approximate the conductivity of graphene by its imaginary part only (the dispersive conductor limit). It allows for writing the eigenvalue equation as

$$1 + \frac{\kappa_2 \epsilon(\omega)}{\kappa_1 \epsilon_2} - \frac{\alpha}{\epsilon_2} \frac{4E_F}{\hbar\omega} \frac{\hbar c \kappa_2}{\hbar\omega} = 0\,. \tag{317}$$

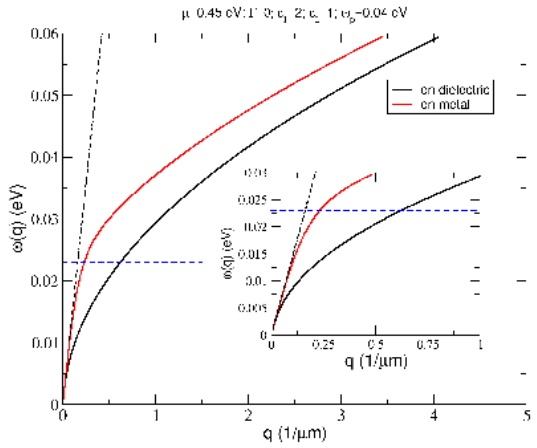

Fig. 38. SPP dispersion curves for graphene on a conductor with $\omega_p = 40$ meV and $\epsilon_\infty = 1$. The dashed black line is the light cone, $q/\sqrt{\epsilon_2}$, and the horizontal line marks the value $\omega = \omega_p/\sqrt{1+\epsilon_2}$.

Equation (317) gives the SPP dispersion relation for graphene placed on a metal. When the conductivity of graphene vanishes, we recover Eq. (311). In Fig. 38 we plot the solution of Eq. (317) for $\omega_p = 0.04$ eV. The general trend of the solution is the following: when $\omega < \omega_p/\sqrt{1+\epsilon_2}$, the SPP dispersion relation is that of the conductor underneath graphene; when $\omega > \omega_p/\sqrt{1+\epsilon_2}$ there is a change of the regime and the dispersion curve follows that of SPPs in graphene cladded by two dielectrics. It should be noted that, for a bulk conductor alone, the SPP dispersion relation lies below the value $\omega_p/\sqrt{1+\epsilon_2}$ for all q (see previous section). We also note that the spectrum for the combined system { graphene+conductor } lies above that for the graphene alone (with $\epsilon_1 = 1$) because for $\omega > \omega_p$ we have $0 < \epsilon(\omega) < 1$. Indeed, when $\omega > \omega_p$ and $q \gg \omega/c$, we can find an analytical expression for $\omega(q)$. In this regime, Eq. (317) reads:

$$1 + \frac{1 - \omega_p^2/\omega^2}{\epsilon_2} + i\frac{\sigma_g q}{\epsilon_0 \omega \epsilon_2} = 0\,. \tag{318}$$

Solving it in order of ω gives

$$\omega = \sqrt{\frac{\omega_p^2}{1+\epsilon_2} + 4\frac{\alpha E_F}{1+\epsilon_2}\frac{qc}{\hbar}}\,. \tag{319}$$

If $\omega_p \to 0$, we recover the dispersion relation of SPPs on a graphene sheet cladded between two media of relative permittivities $\epsilon_1 = 1$ and ϵ_2.

In Fig. 39 we plot the reflectance, transmittance, and absorbance of graphene on a conductive sinusoidal grating. For the plasma frequency we assume a value of 20 meV, corresponding to a doped semiconductor (for example $n-$GaAs, with 10^{18} electrons per cm^3); some types of mesostructures can also have very low plasma frequencies [106]. The choice of such a low plasma frequency simplifies the analysis, since, in this case, the only propagating order is the specular one. If there is no graphene on the grating (central panel of Fig. 39), we have total reflection for $\omega < \omega_p' = \omega_p/\sqrt{\epsilon_\infty}$, as it should be. When the graphene is present, the reflectance is smaller than 1 for $\omega < \omega_p'$ because of the absorption in graphene. Note, however, that if graphene were supported by a dielectric instead of the conductor, the reflectance would be much lower (top panel of Fig. 39). Above ω_p', for this choice of parameters, the reflectance and the transmittance show coupling of ER to the SPPs in graphene. The presence of the conductor beneath the graphene sheet shifts the position of the peak of the resonance toward higher energies because the its dielectric permittivity, although positive, is smaller than 1 (note that $\epsilon_\infty = 1$ in this example).

As it can be seen in Fig. 39, the presence of graphene introduces a dip in the transmittance, at $\omega > \omega_p$. At the same time, an enhancement of the absorption of graphene is observed. It is also clear (bottom panel) that the reflectance drops to zero at a given frequency above 0.03 eV, which does not occur when graphene stands alone on a dielectric grating (top panel). Note that the metal does not absorb electromagnetic radiation, since in this model its dielectric constant is purely

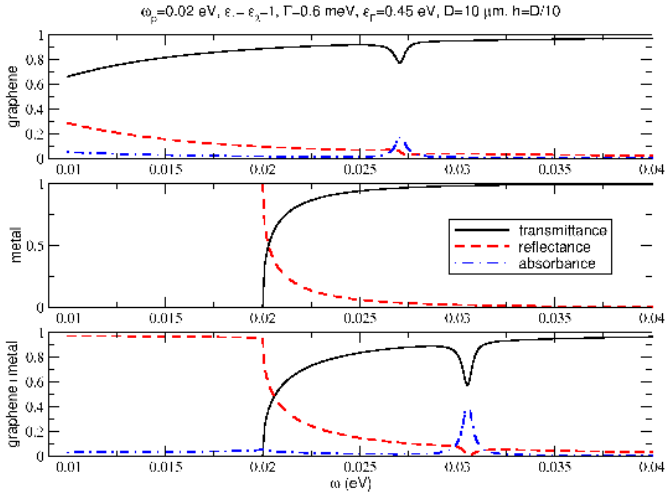

Fig. 39. Reflectance, transmittance, and absorbance of graphene on a conductive sinusoidal grating. Top panel: free standing graphene with a sinusoidal profile. Central panel: sinusoidal metallic grating without graphene. Bottom panel: graphene on a sinusoidal metallic grating. The parameters are: $\epsilon_2 = \epsilon_\infty = 1$, $\Gamma = 0.6$ meV, $\omega_p = 0.02$ eV, $E_F = 0.45$ eV, $D = 10$ μm, and $h = D/10$.

real. The absorption occurs entirely within the graphene sheet. If the conductive substrate also absorbes ER, the analysis becomes more complex [77].

11. Summary

At present, graphene plasmonics is an active field of research, both theoretical and experimental. The community has been addressing a broad range of topics in this field, some of which are: (i) coupling of ER to SPPs in graphene; (ii) use of nanoemitters for excitation of SPPs; (iii) enhancement of light absorption in graphene owing to SPPs; (iv) filters and polarizers exploring the propagation of SPPs along a graphene-covered surface; (v) launching and detection of SPPs in graphene, aiming at nanoplasmonic-based circuitry; (vi) exploring graphene double-layers (or multilayers) where two (or more) different SPP branches emerge; (vii) ER switches and polarizers based on the ATR configuration; and (viii) formation of polaritonic crystals with band gaps controlled by gate voltage.

In this work we focused on the SPP spectra of single and double layer graphene systems. We showed that the ATR configuration can work as an optical switch and that the double-layer system allows for moving the resonant energy towards higher energies. We showed further that, exploring the different response of graphene to TM and TE waves, one can control the state of polarization of the outgoing wave by changing the electron Fermi energy in graphene. It was demonstrated that SPP excitation can be achieved directly by illuminating a thin metallic stripe deposited on top of graphene, which can be viewed as a topological defect in the otherwise uniform

system, which enables to overcome the restriction imposed by the in-plane momentum conservation. We discussed the physics of graphene-based gratings where the underlying material is either a dielectric or a conductor. We also showed that, even in the absence of a grating, an efficient ER-SPP coupling exists in graphene systems with periodically modulated conductivity, which can be induced by different mechanisms (e.g., strain, doping, and gating). In particular, it was shown for an array of microribbons and for a continuous graphene sheet with a cosine-modulated conductivity. Both systems have the properties of a polaritonic crystal, although there is some difference in details between them. Another system from which one should expect qualitatively similar properties is graphene deposited on a periodically corrugated surface (a grating). The presented computational description of structures of this type in terms of Rayleigh-Fano expansions is demanding because the problem is poorly convergent. Even though, the cases of a sinusoidal and a sawtooth grating were considered and we showed that the ER-SPP coupling manifests itself by resonances in the reflectance, transmittance, and absorbance spectra. When graphene is placed on a metallic surface with smooth periodic profile, the SPP dispersion is hybrid, showing the properties of a bulk metal at low wavenumbers and those of an isolated graphene sheet as large wavenumbers. Not surprisingly, the change of the regime takes place close to the plasma frequency of the metal underlying the graphene sheet.

Acknowledgements

This work was partially supported by FEDER through the COMPTETE Program and by the Portuguese Foundation for Science and Technology (FCT) through Strategic Project PEst-C/FIS/UI0607/2011. A.F. greatly acknowledges support from National Research Foundation-Competitive Research Programme through award "Novel 2D materials with tailored properties: beyond graphene" (Grant No. R-144-000-295-281).

References

1. Wood R W 1902 *Phil. Mag.* **4** 396
2. Rayleigh L 1907 *Phil. Mag.* **14** 60
3. Fano U 1936 *Phys. Rev* **50** 573
4. Fano U 1937 *Phys. Rev* **51** 288
5. Kretschmann E and Reather H 1968 *Z. Naturf.* **23A** 2135
6. Otto A 1968 *Z. Phys.* **216** 398
7. Sambles J R, Bradbary G W and Yang F 1991 *Contemporary Phys.* **32** 173
8. Toigo F, Marvin A, Celli V and Hill N R 1977 *Phys. Rev. B* **15** 5618
9. Chandezon J, Dupuis M T and Cornet G 1982 *J. Opt. Soc. Am.* **72** 839
10. Li L, Chandezon J, Granet G and Plumey J 1999 *Appl. Opt.* **38** 304
11. Ebbesen T W, Lezec H J, Ghaemi H F, Thio T and Wolf P A 1998 *Nature* **391** 667
12. Barnes W L, Dereux A and Ebbesen T W 2003 *Nature* **424** 824
13. Ebbesen T W, Genet C and Bozhevolnyi S I 2008 *Phys. Today* **May** 44

14. Mary A, Rodrigo S G, Martn-Moreno L and Garca-Vidal F J 2007 *Phys. Rev. B* **76** 195414
15. Sturman B, Podivilov E and Gorkunov M 2008 *Phys. Rev. B* **77** 075106
16. Stockman M I 2011 *Phys. Today* **February** 39
17. Maier S A 2007 *Plasmonics: Fundamentals and Applications* (Springer)
18. Kneipp K 2007 *Phys. Today* **Movember** 40
19. Lee J, Shim S, Kim B and Shin H S 2011 *Chem. Eur. J.* **17** 2381
20. Zhang J, Zhang L and Xu W 2012 *J. Phys. D: Appl. Phys.* **45** 113001
21. Jung L S, Campbell C T, Chinowsky T M, Mar M N and Yee S S 1998 *Langmuir* **14** 5636
22. Haes A J, Haynes C L, DMcFarland A, Schatz G C, Van Duyne R P and Zou S 2005 *MRS Bulletin* **30** 368
23. Willets K A and Van Duyne R P 2007 *Annu. Rev. Phys. Chem.* **58** 267
24. Shalabney A and Abdulhalim I 2011 *Laser Photon. Rev.* **5** 571
25. Green M A and Pillai S 2012 *Nature Photonics* **6** 130
26. Reece P J 2008 *Nature Photonics* **2** 333
27. Juan M L, Righini M and Quidant R 2011 *Nature Photonics* **5** 349
28. Ozbay E 2006 *Science* **311** 189
29. Han Z and Bozhevolny S I 2013 *Rep. Prog. Phys.* **76** 016402
30. Vakil A and Engheta N 2011 *Science* **332** 1291
31. Vakil A and Engheta N 2012 *Phys. Rev. B* **85** 075434
32. Xu H J, Lu W B, Zhu W, Dong Z G and Cui T J 2012 *Appl. Phys. Lett.* **100** 243110
33. Shung K W K 1986 *Phys. Rev. B* **34** 979
34. Hwang E H and Das Sarma S 2007 *Phys. Rev. B* **75** 205418
35. Wunsch B, Stauber T, Sols F and Guinea F 2006 *New J. Phys.* **8** 318
36. Stauber T, Schliemann J and Peres N M R 2010 *Phys. Rev. B* **81** 085409
37. Jablan M, Buljan H and Soljačić M 2009 *Phys. Rev. B* **80** 245435
38. Stauber T, Peres N M R and Guinea F 2007 *Phys. Rev. B* **76** 205423
39. Mishchenko E G, Shytov A V and Silvestrov P G 2010 *Phys. Rev. Lett.* **104** 156806
40. Popov V V, Bagaeva T Y, Otsuji T and Ryzhii V 2010 *Phys. Rev. B* **81** 073404
41. Wang W, Apell P and Kinaret J 2011 *Phys. Rev. B* **84** 085423
42. Schultz M H, Jauho A P and Pedersen T G 2011 *Phys. Rev. B* **84** 045428
43. Thongrattanasiri S, Manjavacas A and de Abajo F J G 2012 *ACS Nano* **6** 1766
44. Nikitin A Y, Guinea F, Garcia-Vidal F J and Martin-Moreno L 2011 *Phys. Rev. B* **85** 081405
45. Nikitin A Y, Guinea F, Garcia-Vidal F J and Martin-Moreno L 2011 *Phys. Rev. B* **84** 161407
46. Thongrattanasiri S, Silveiro I and de Abajo F J G 2012 *Appl. Phys. Lett.* **100** 201105
47. Andersen D R and Raza H 2012 *Phys. Rev. B* **85** 075425
48. Christensen J, Manjavacas A, Thongrattanasiri S, Koppens F H L and de Abajo F J G 2012 *ACS Nano* **6** 431
49. Pellegrino F M D, Angilella G G N and Pucci R 2010 *Phys. Rev. B* **82** 115434
50. Pellegrino F M D, Angilella G G N and Pucci R 2011 *Phys. Rev. B* **84** 195407
51. Koppens F H L, Chang D E and de Abajo F J G 2011 *Nano Lett.* **11** 3370
52. Nikitin A Y, Guinea F, Garcia-Vidal F J and Martin-Moreno L 2011 *Phys. Rev. B* **84** 195446
53. Gómez-Santos G and Stauber T 2011 *Phys. Rev. B* **84** 165438
54. Huidobro P A, Nikitin A Y, Gonzlez-Ballestero C, Martn-Moreno L and Garca-Vidal F J 2012 *Phys. Rev. B* **85** 155438
55. Manjavacas A, Nordlander P and de Abajo F J G 2012 *ACS Nano* **6** 1724

56. Hwang E H, Sensarma R and Das Sarma S 2010 *Phys. Rev. B* **82** 195406
57. Jablan M, Buljan H, and Soljačić M 2011 *OPTICS EXPRESS* **19** 11236
58. Stauber T and Gómez-Santos G 2012 *Phys. Rev. B* **85** 075410
59. Profumo R E V, Asgari R, Polini M and MacDonald A H 2012 *Phys. Rev. B* **85** 085443
60. Gan C H, Chu H S and Li E P 2012 *Phys. Rev. B* **85** 125431
61. Ilic O, Jablan M, Joannopoulos J D, Celanovic I, Buljan H and Soljačić M 2012 *Phys. Rev. B* **85** 155422
62. Wang B, Zhang X, Yuan X and Teng J 2012 *Appl. Phys. Lett.* **100** 131111
63. Schedin F, Lidorikis E, Lombardo A, Kravets V G, Geim A K, Grigorenko A N, Novoselov K S and Ferrari A C 2010 *ACSNano* **4** 5617
64. Ju L, Geng B, Horng J, Girit C, Martin M C, Hao Z, Bechtel H A, Liang X, Zettl A, Shen Y R and Wang F 2011 *Nature Nanotechnology* **6** 630
65. Echtermeyer T J, Britnell L, Jasnos P K, Lombardo A, Gorbachev R V, Grigorenko A N, Geim A K, Ferrari A and Novoselov K S 2011 *Nature Communications* **2** 458
66. Fei Z, Andreev G O, Bao W, Zhang L M, McLeod A S, Wang C, Stewart M K, Zhao Z, Dominguez G, Thiemens M, Fogler M M, Tauber M J, Castro-Neto A H, Lau C N, Keilmann F and Basov D N 2011 *Nano Lett.* **11** 4701
67. Castro Neto A H, Guinea F, Peres N M R, Novoselov K S and Geim A K 2009 *Rev. Mod. Phys.* **81** 109
68. Peres N M R 2010 *Rev. Mod. Phys.* **82** 2673
69. Zhang X C and Xu J 2010 *Introduction to THz Wave Photonics* (Springer)
70. Fei Z, Rodin A S, Andreev G O, Bao W, McLeod A S, Wagner M, Zhang L M, Zhao Z, Dominguez G, Thiemens M, Fogler M M, Castro-Neto A H, Lau C N, Keilmann F and Basov D N 2012 *arXiv* 1202.4993
71. Chen J, Badioli M, Alonso-Gonzlez P, Thongrattanasiri S, Huth F, Osmond J, Spasenovic M, Centeno A, Pesquera A, Godignon P, Zurutuza A, Camara N, de Abajo J G, Hillenbrand R and Koppens F 2012 *arXiv* 1202.4996
72. Yan H, Li X, Chandra B, Tulevski G, Wu Y, Freitag M, Zhu W, Avouris P and Xia F 2012 *Nature Nano.* **7** 330
73. Chen P Y and Alù A 2011 *ACS Nano* **5** 5855
74. Bludov Y V, Vasilevskiy M I and Peres N M R 2010 *EPL* **92** 68001
75. Crassee, Orlita M, Potemski M, Walter A L, Ostler M, Seyller T, Gaponenko I, Chen J and Kuzmenko A B 2012 *Nano Lett.* **12** 2470
76. Sreekanth K V, Zen S, Shang J, Yong K-T, and Ting Yu 2012 *Sci. Rep.* **2** 737
77. Ferreira A and Peres N M R 2012 *Phys. Rev. B* **86** 205401
78. Peres N M R, Ferreira A, Bludov Y V and Vasilevskiy M I 2012 *J. Phys.: Condens. Matter* **24** 245303
79. Davoyan A R, Popov V V and Nikitov S A 2012 *Phys. Rev. Lett.* **108** 127401
80. Bludov Y V, Peres N M R and Vasilevskiy M I 2012 *Phys. Rev. B* **85** 245409
81. De Martini F and Shen Y R 1976 *Phys. Rev. Lett.* **36** 216
82. Georges A T and Karatzas N E 2012 *Phys. Rev.* **85** 155442
83. Renger J, Quidant R, van Hulst N, Palomba S and Novotny L 2009 *Phys. Rev. Lett.* **103** 266802
84. Aharonian K H and Tilley D R 1989 *J. Phys.: Condens. Matter* **1** 5391
85. Fowles G R 1989 *Introduction to Modern Optics* (Dover, New York)
86. Peres N M R, Guinea F and Castro Neto A H 2006 *Phys. Rev. B* **73** 125411
87. Falkovsky L A and Pershoguba S S 2007 *Phys. Rev. B* **76** 153410
88. Stauber T, Peres N M R and Geim A K 2008 *Phys. Rev. B* **78** 085432
89. Abedinpour S H, Vignale G, Principi A, Polini M, Tse W K and MacDonald A H

2011 *Phys. Rev. B* **84** 045429
90. Ferreira A, Viana-Gomes J, Bludov Y V, Pereira V, Peres N M R and Castro Neto A H 2011 *Phys. Rev. B* **84** 235410
91. Ziman J M 2001 *Electrons and Phonons* (Oxford University Press)
92. Dubinov A A, Aleshkin V Y, Mitin V, Otsuji T and Ryzhii V 2011 *J. Phys.: Condens. Matter* **23** 145302
93. Bao Q, Zhang H, Wang B, Ni Z, Lim C H Y X, Wang Y, Tang D Y and Loh K P 2011 *Nature Photonics* **5** 411
94. Falko V I and Khmelnitskii D E 1989 *Sov. Phys. JETP* **68** 1150
95. Born M and Wolf E 1989 *Principles of Optics* (Pergamon)
96. Hecht E 2003 *Optics* 4th ed (Pearson)
97. Ferreira A, Peres N M R and Castro Neto A H 2012 *Phys. Rev. B* **85** 205426
98. Roldan R, Fuchs J N and Goerbig M O 2009 *Phys. Rev. B* **80** 085408
99. Chiu K W and Quinn J J 1974 *Phys. Rev. B* **9** 4724
100. Kukushkin I V, Muravev V M, Smet J H, Hauser M, Dietsche W and von Klitzing K 2006 *Phys. Rev. B* **73** 113310
101. Satou A and Mikhailov S A 2007 *Phys. Rev. B* **75** 045328
102. P. M. Morse and H. Feshbach 1953 *Methods of theoretical physics* (McGraw-Hill, New York)
103. Park S, Lee G, Song S H, Oh C H and Kim P S 2003 *Optics Lett.* **28** 41870
104. Chen X and Friedman A 1991 *Trans. Amer. Math. Soc.* **323** 465
105. Smirnov G 1997 *J. Math. Anal. Appl.* **214** 395
106. Pendry J B, Holden A J, Stewart W J and Youngs I 1996 *Phys. Rev. Lett.* **76** 4773
107. Fox M 2007 *Optical Properties of Solids* (Oxford)
108. Torrell M, Kabir R, Cunha L, Vasilevskiy M I, Vaz F, Cavaleiro A, Alves E and Barradas N P 2011 *J. Appl. Phys.* **109** 074310
109. Horing N J M 2009 *Phys. Rev. B* **80** 193401